

GLOBAL DYNAMICS OF THE EARTH'S PLASMASPHERE

A DISSERTATION
SUBMITTED TO THE DEPARTMENT OF ELECTRICAL ENGINEERING
AND THE COMMITTEE ON GRADUATE STUDIES
OF STANFORD UNIVERSITY
IN PARTIAL FULFILLMENT OF THE REQUIREMENTS
FOR THE DEGREE OF
DOCTOR OF PHILOSOPHY

Maria Spasojević
October 2003

© Copyright by Maria Spasojević 2004
All Rights Reserved

I certify that I have read this dissertation and that, in my opinion,
it is fully adequate in scope and quality as a dissertation for the
degree of Doctor of Philosophy.

Umran S. Inan
(Principal Adviser)

I certify that I have read this dissertation and that, in my opinion,
it is fully adequate in scope and quality as a dissertation for the
degree of Doctor of Philosophy.

Donald L. Carpenter

I certify that I have read this dissertation and that, in my opinion,
it is fully adequate in scope and quality as a dissertation for the
degree of Doctor of Philosophy.

Martin Walt

Approved for the University Committee on Graduate Studies.

Abstract

The structure and dynamics of the plasmasphere are highly sensitive to the geomagnetic disturbance activity that occurs regularly within the Earth's magnetosphere. The cycles of erosion and refilling of the plasma population in the plasmasphere have been studied extensively in the past but from the relatively limited perspective of individual (or occasionally multiple) ground stations and satellite crossings of the plasmopause and plasmasphere. Data available from the Extreme Ultraviolet Imager (EUV) on the IMAGE satellite allow us, for the first time, to study the plasmasphere system from a global perspective. The EUV instrument images the He^+ distribution in the plasmasphere by detecting resonantly scattered solar 30.4-nm radiation and produces images encompassing the entire plasmasphere with approximately 640 km spatial resolution once every 10 minutes. By tracking the location of the plasmopause in sequences of EUV images, we make quantitative measurements of radial and azimuthal motions of the boundary during the various phases of geomagnetic disturbances. We examine the rapid inward motion of the plasmopause boundary on the nightside as well as the sunward motion on the dayside which occurs at the onset of a disturbance. After several hours of continued enhanced activity, a plasmaspheric "plume" forms in the afternoon local time sector as a result of the interplay between forces driving the plasma sunward and those which tend to force the plasmasphere to rotate with the Earth. We also note the tendency for mesoscale azimuthal variations ($\leq 1 R_E$ in radial extent and $\leq 30^\circ$ in azimuthal extent) in the plasmopause radius to develop in a limited local time sector on the dayside during these active periods. In the aftermath of a disturbance, we follow the evolution of the plasmaspheric plumes and the degree to which they begin to corotate with the Earth. These disturbances

represent periods of significant redistribution of mass within the magnetosphere, and using the global images, we estimate that 50 to 100 metric tons of material, constituting between 25 % and 45 % of the initial plasmaspheric distribution, is removed from a volume extending from 1.5 to 5.5 R_E in a period of 15 hours or less. Finally, we identify an association between the plasmaspheric plume and energetic protons precipitating into the subauroral ionosphere. During a geomagnetic disturbance on June 18, 2001, a detached subauroral proton arc mapped along geomagnetic field lines to a broad region of enhanced cold plasma density associated with the plasmaspheric plume. The link between the proton arc and plasmaspheric plume suggests that the proton precipitation may be a result of wave-particle interactions which preferentially occur within the plume region.

Acknowledgments

I would like to thank my principal thesis adviser, Professor Umran Inan, for bring me into the VLF group, for his enthusiasm, leadership and perhaps most importantly for his confidence in my abilities throughout my six year tenure at Stanford. I would also like to express my gratitude to Professor Donald Carpenter. For the past several years, Don has been critical in guiding my research and in helping me to put my own results in the context of the extensive past work on the subject. I will always strive to be as careful and patient a researcher as Don.

I owe tremendous thanks to Dr. Bill Sandel and the entire EUV instrument team at the University of Arizona. They designed a fabulous instrument and continually provided updated tools for data analysis. Special recognition goes to Terry Forrester for his prompt replies to my numerous data requests. I would also like to thank Dr. James Burch of Southwest Research Institute for his leadership in the IMAGE satellite program.

I am grateful to Professor Martin Walt, for serving on my oral defense committee and for his timely yet thorough reading of this dissertation, and to Professor John Pauly, for serving as chairman of my defense committee.

I have benefited greatly from being a part of the VLF group and am grateful for the assistance and friendship of many present and former group members. I would especially like to acknowledge Jacob Bortnik, Elizabeth Gerken, Troy Wood, Michael Chevalier, Georgios Veronis, Timothy Chevalier, Robb Moore, Mehmet Demirkol, David Lauben, and Michael Johnson. Special thanks also goes to Shaolan Min, our administrative assistant.

I would like to thank to my parents, David and Victoria Salvati, and my sister, Andrea DeLuca, for a lifetime of encouragement and for all they have done for me.

Above all, I wish to thank my husband Mirko for his love, emotional support and constant reassurance throughout this long and at times difficult process.

MARIA SPASOJEVIĆ
Stanford, California
October 16, 2003

This research was supported by the National Aeronautics and Space Administration through the Graduate Student Researchers Program fellowship NGT5-92, through contract NAS5-96020 under subcontract 03-08482 from University of Massachusetts, and through contract NAG5-9974 under subcontract 4000061641 from the University of Iowa. We also acknowledge support from the National Science Foundation Office of Polar Programs through grant OPP-9818175 under subcontract Z365605 from University of Maryland.

Contents

Abstract	iv
Acknowledgments	vi
1 Introduction	1
1.1 The Earth's Magnetosphere	2
1.1.1 Coordinate Systems	4
1.1.2 Magnetospheric Plasma Regions	5
1.2 Geomagnetic Activity	8
1.3 Experimental Techniques	10
1.4 Geophysical Importance of the Plasmasphere	12
1.5 Contributions of this Research	12
2 Background and Past Research	14
2.1 Frozen-in Magnetic Flux	14
2.2 Bulk Plasma Motion	17
2.2.1 Corotation	17
2.2.2 Convection	17
2.2.3 Global Convection Models	20
2.3 Past Research on Plasmaspheric Dynamics	20
2.3.1 Early Discoveries	20
2.3.2 Basic Plasmaspheric Dynamics	21
2.3.3 Departures from Corotation	22
2.3.4 Reduction in the Plasmopause Radius	23

2.3.5	Duskside Bulge and Detached Plasma Regions	24
2.3.6	The Loss of Plasmaspheric Plasma	26
2.3.7	Irregular Density Structure	28
3	Observational Techniques	29
3.1	IMAGE Satellite Overview	29
3.2	Radio Plasma Imager	30
3.2.1	Deriving Electron Density from UHR Measurements	33
3.3	Extreme Ultraviolet Imager	36
3.3.1	Mapping EUV Images to the Equatorial Plane	37
3.4	The He ⁺ Edge and the Plasmopause	45
3.4.1	Methodology	45
3.4.2	Example Cases	47
3.4.3	Statistical Analysis	53
3.4.4	Conclusions	56
4	The Global Response of the Plasmasphere	58
4.1	Case I: June 26 – 27, 2001	59
4.1.1	Quiet Geomagnetic Conditions	59
4.1.2	Disturbance Onset	62
4.1.3	Disturbance Main Phase	64
4.1.4	Recovery Phase	70
4.2	Case II: June 9 – 10, 2001	74
4.2.1	Multi-staged Onset	76
4.2.2	Recurrent Substorm Activity	79
4.3	Conclusions	83
5	The Loss of Plasmaspheric Plasma	86
5.1	Estimating Plasma Loss	86
5.1.1	Calculating the Amount of He ⁺ Removed	92
5.1.2	Correlation of the Loss Percentage with IMF B_z	93
5.1.3	Comparing Losses Inside and Outside the New Plasmopause	95

5.1.4	Estimating the Total Mass of Material Lost	95
5.2	Conclusions	98
6	The Plume and Precipitating Protons	99
6.1	Previous Observations	99
6.2	Plasmaspheric Plume Formation	101
6.3	Detached Subauroral Proton Arc	105
6.4	Wave-Particle Interactions	109
6.5	Conclusions	111
7	Summary	112
7.1	Summary of Major Results	112
7.2	Suggestions for Future Research	114
	Bibliography	117

List of Figures

1.1	Schematic Diagram of the Earth's Magnetosphere	2
1.2	Solar Wind Distortion of the Earth's Magnetic Field	3
1.3	Coordinate Systems for the Inner Magnetosphere	4
1.4	Electron Density Distribution in the Plasmasphere	6
2.1	Magnetic Merging and Magnetospheric Convection	18
2.2	Equatorial Flow Patterns from the E5D Model	19
3.1	IMAGE Orbit from June 10, 2001	30
3.2	RPI Dynamic Spectrogram from June 10, 2001	32
3.3	Extracting Density from RPI Dynamic Spectrograms	35
3.4	EUV Image of the Plasmasphere from 06:12 UT on June 10, 2001 . .	36
3.5	He ⁺ Distribution Along Line of Sight Tangent to Plasmapause	40
3.6	Example of the Plasmapause Mapped to the Equatorial Plane	41
3.7	He ⁺ Distribution Along Line of Sight Interior to Plasmapause	43
3.8	Example of the Entire Plasmasphere Mapped to the Equatorial Plane	44
3.9	RPI and EUV Plasmapause Observation Locations on June 10, 2001 .	46
3.10	RPI Observation of the Plasmapause Gradient on June 10, 2001 . . .	47
3.11	He ⁺ Edges Bracketing the RPI Measurement on June 10, 2001	48
3.12	Comparison of RPI and EUV Plasmapause Locations on June 10, 2001	49
3.13	The <i>Kp</i> Index for June 10, 2001	50
3.14	Comparison of RPI and EUV Plasmapause Locations on June 2, 2001	51
3.15	The <i>Kp</i> Index for June 2, 2001	51
3.16	Comparison of RPI and EUV Plasmapause Locations on June 25, 2001	52

3.17	The Kp Index for June 25, 2001	52
3.18	Correlation Between $L_{\text{EUV,closest}}$ and L_{RPI}	53
3.19	Correlation Between $L_{\text{EUV,avg}}$ and L_{RPI}	54
3.20	Correlation Between $L_{\text{EUV,avg2}}$ and L_{RPI}	55
3.21	Comparison of Independent EUV Edge Extractions	56
4.1	Geomagnetic and Solar Wind Conditions for June 26 – 27, 2001	60
4.2	Pre-disturbance Plasmasphere on June 26, 2001	61
4.3	Tracking the Erosion Rate on June 26, 2001	63
4.4	Plume Formation on June 26 – 27, 2001	65
4.5	Tracking the Western Edge of the Plume on June 26 – 27, 2001	66
4.6	Density Measurements of the Plume at Geosynchronous Orbit.	68
4.7	Plume Evolution on June 27, 2001	71
4.8	Tracking the Plume Rotation on June 27, 2001	72
4.9	RPI Density Measurement on June 27, 2001	73
4.10	Geomagnetic and Solar Wind Conditions for June 9 – 10, 2001	75
4.11	Plasmapause Locations During Onset for June 9, 2001	76
4.12	Plume Wrapping and Channel Formation on June 10, 2001	78
4.13	Tracking the Western Edge of the Plume on June 10, 2001	79
4.14	Density Measurements of the Plume at Geosynchronous Orbit.	80
4.15	Tracking the Outward Motion of the Shoulder on June 10, 2001	81
4.16	Multiple Plume Formation on June 10, 2001	82
5.1	Loss of Plasmaspheric Material on June 18, 2001	87
5.2	Loss of Plasmaspheric Material on May 8 – 9, 2001	88
5.3	Loss of Plasmaspheric Material on May 28, 2001	89
5.4	Loss of Plasmaspheric Material on June 02, 2001	90
5.5	Loss of Plasmaspheric Material on June 26, 2001	91
5.6	Initial and Final He^+ Abundance for the 5 Disturbance Periods	92
5.7	Loss Percentage versus the Strength and Direction of IMF B_z	93
5.8	Loss Percentage Inside and Outside the New Plasmapause	94
5.9	Ratio of He^+ to H^+ Densities as a Function of Radial Distance	96

5.10	Total Mass Lost for Each Event Using Different He^+ / H^+ Ratios . . .	97
6.1	Geomagnetic and Solar Wind Conditions on June 18, 2001	102
6.2	EUV Plume Formation Sequence from June 18, 2001	103
6.3	LANL–01a MPA Measurements on June 18, 2001	104
6.4	FUV SI12 Image from 15:50 UT on June 18, 2001	106
6.5	FUV SI12 Keogram at 16 MLT on June 18, 2001	107
6.6	Tsyganenko Mapping of the Plasmapause and Proton Arc	108
7.1	Formation of a Notch on 28 May 2001	116

Chapter 1

Introduction

The plasmasphere is a vast toroidal region of ionized gas or plasma that encircles the Earth and extends from the top of the ionized upper atmosphere at altitudes of about 1000 km out to equatorial altitudes ranging from about 10,000 to 40,000 km. The structure and dynamics of the plasmasphere are highly sensitive to geomagnetic disturbance activity in the near-Earth space environment. The plasmasphere has been studied extensively for over forty years, and the historical development of plasmaspheric research is detailed in a monograph on the subject by *Lemaire and Gringauz* [1998]. This monograph reviews past experimental work, theoretical aspects, and modeling of the plasmasphere system, while also emphasizing the many outstanding scientific issues and gaps in our current knowledge which exist in part due to limitations of past experimental techniques.

Many ongoing and fundamental questions about the evolving structure of the plasmasphere can now be addressed with the data available from the Extreme Ultraviolet Imager (EUV), which was launched onboard the IMAGE satellite in March of 2000. The EUV instrument employs a novel technique to produce images encompassing the entire plasmasphere in a single snapshot, thus allowing for the first time the study of this region of space from a global vantage point. The plasmasphere is host to many of the complex interactions among charged particle populations and electromagnetic fields in near-Earth space, and knowledge of its dynamics on a global scale is therefore fundamental to our understanding of the flow of mass and energy within the

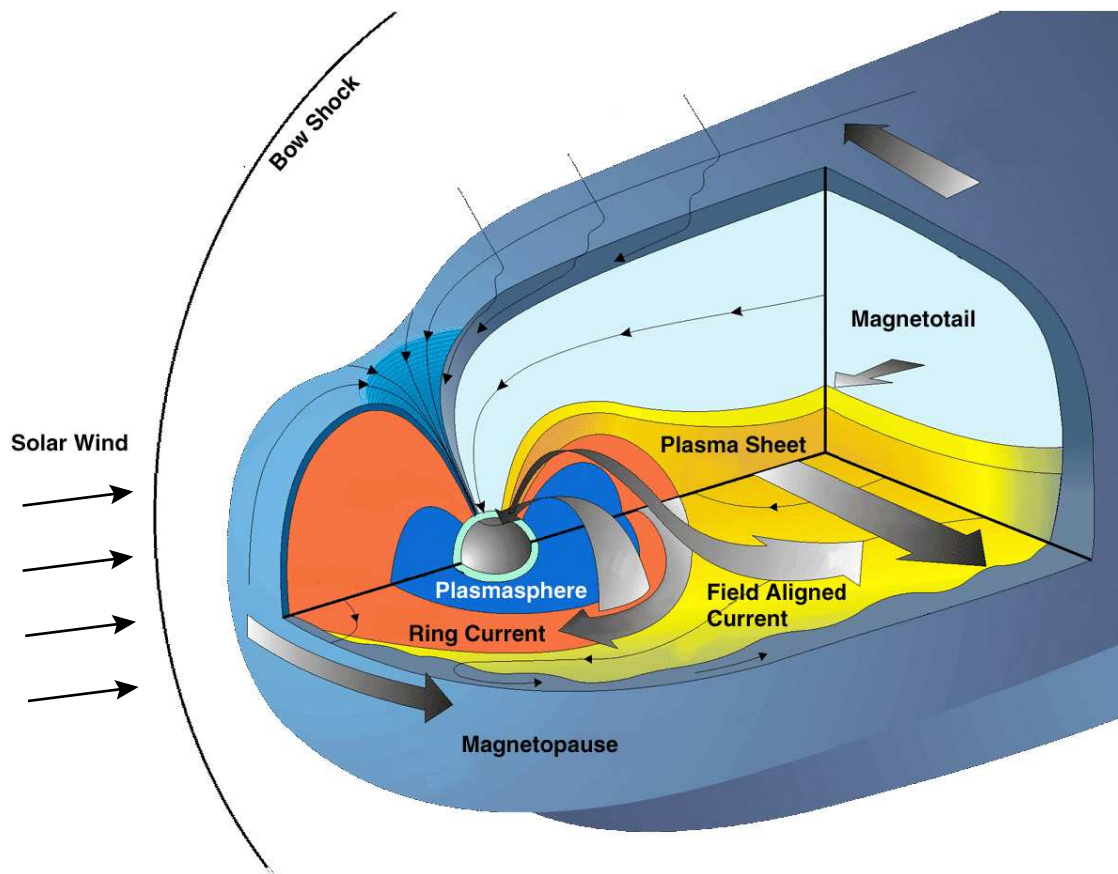


Figure 1.1. A schematic diagram of the Earth's magnetosphere with various plasma regions and current systems identified.

solar-terrestrial environment.

1.1 The Earth's Magnetosphere

The plasmasphere is but one part of a larger region of near-Earth space called the magnetosphere. The Earth's magnetosphere is a complex configuration of plasma regions with a wide range of densities and temperatures, contains several large scale current systems, and hosts a variety of electromagnetic and electrostatic wave phenomena. The magnetosphere, shown schematically in Figure 1.1, is formed as a result of the interaction between the intrinsic magnetic field of the Earth and the solar wind

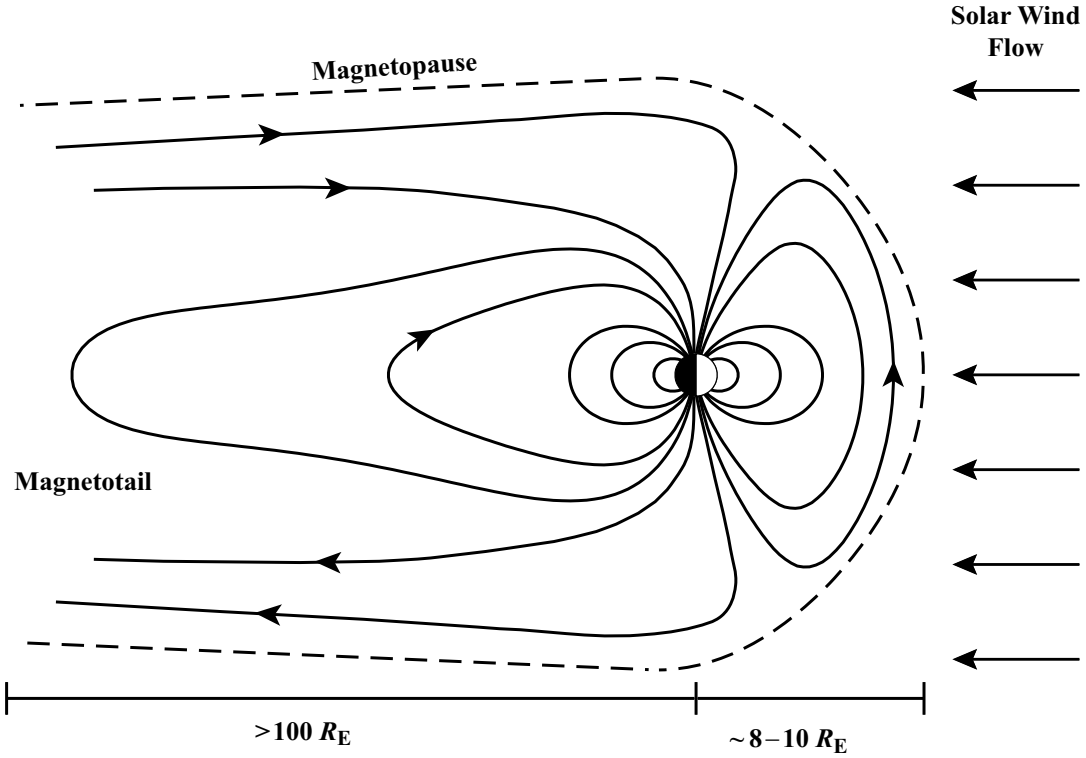


Figure 1.2. A schematic diagram in the noon-midnight meridional plane showing the distortion of the Earth's intrinsic magnetic field by the solar wind flow forming the magnetosphere.

blowing outward from the Sun [Cowley, 1996].

The magnetic field of the Earth [Chapman and Bartels, 1940] is believed to be created by currents in the molten, electrically conducting core of the Earth. It can be approximated, to first order, as a dipole whose axis is tilted $\sim 11^\circ$ from the Earth's spin axis. This magnetic field points down towards the surface of the Earth in the northern hemisphere and away from it in the southern hemisphere. The average magnetic field strength on the surface of the Earth is $\sim 50 \mu\text{T}$.

The solar wind [Neugebauer and Snyder, 1966] is a fully ionized plasma that streams continuously outward from the Sun at speeds of about 300 to 800 km/s. It is comprised primarily of protons and electrons with a small percentage (less than 5% by number) of alpha particles and heavier ions and has an average electron number density of $\sim 5 \text{ cm}^{-3}$. The average energy of solar wind particles is about 10 eV.

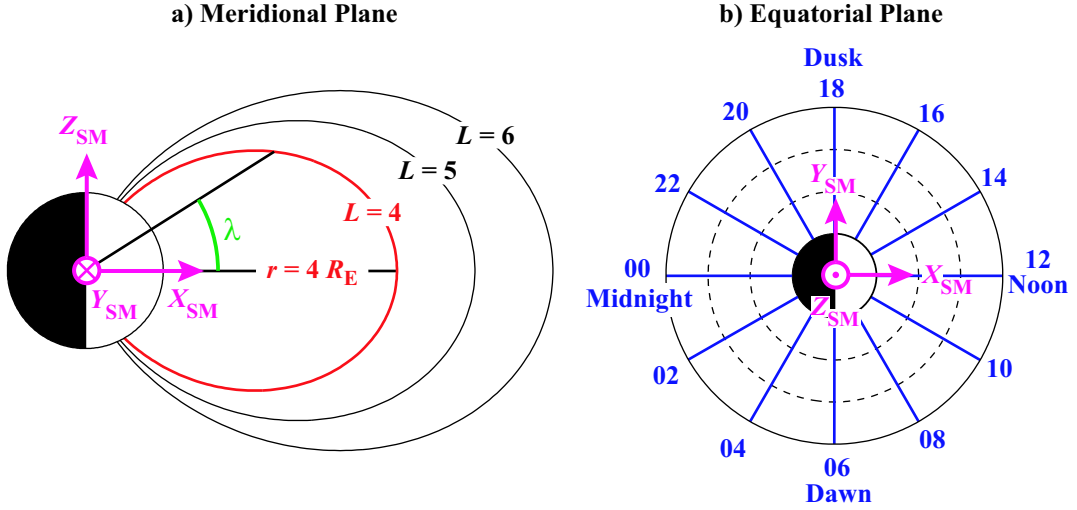


Figure 1.3. Cross-sections in the (a) meridional and (b) equatorial planes identifying the solar magnetic (SM) coordinate system as well as the parameters, L , λ (a) and magnetic local time (MLT) (b).

Embedded in the solar wind is a large scale interplanetary magnetic field (IMF) with an average strength of ~ 5 nT.

As the solar wind approaches the Earth, it cannot easily penetrate the dipolar magnetic field but is instead slowed down and deflected around it [Chapman and Ferraro, 1931]. The kinetic pressure of the solar wind distorts the outer part of the Earth's magnetic field, and the resulting field is shown schematically in Figure 1.2. On the dayside, the solar wind compresses the Earth's magnetic field so that the magnetopause boundary is typically located at a geocentric distance of $8 - 10$ Earth radii ($1 R_E = 6378$ km). A long magnetotail is formed extending for several hundred R_E on the nightside. However, near the Earth the dipole configuration of the geomagnetic field is relatively unaffected by the solar wind flow.

1.1.1 Coordinate Systems

This work focuses on studies of the inner magnetosphere which can be loosely defined as the region of space inside of the geosynchronous orbit lying at a geocentric equatorial distance of $6.6 R_E$. Throughout most of this dissertation, we assume that

the magnetic field of the Earth in this region can be approximated with reasonable accuracy by a centered, tilted dipole.

For studies of the inner magnetosphere, the solar magnetic (SM) coordinate system is often used [Kivelson and Russell, 1995, App. 3]. In the SM system, the Z_{SM} axis is coincident with the geomagnetic dipole axis, the Y_{SM} axis is perpendicular to the Earth-Sun line toward dusk, and the XZ_{SM} plane contains the Sun direction. The SM system rotates with both a yearly and daily period with respect to inertial coordinates.

However, since magnetospheric plasma is strongly ordered by the magnetic field, it is useful to define another coordinate system with the three coordinates being L , magnetic latitude (λ), and magnetic local time (MLT). In a dipole magnetic field, the equation of a field line can be expressed [Walt, 1994, Ch. 3] as

$$r = L \cos^2 \lambda \quad (1.1)$$

The L parameter essentially identifies a field line and is defined as the distance in Earth radii at which a field line crosses the magnetic equatorial plane, and λ is magnetic latitude as measured from the equator (Figure 1.3a). The third parameter, MLT, defines the azimuthal component and is measured counter-clockwise (when looking in $-Z_{\text{SM}}$ direction) in decimal hours from 00 MLT (magnetic midnight) in the $-X_{\text{SM}}$ direction as shown in Figure 1.3b.

1.1.2 Magnetospheric Plasma Regions

There are several magnetospheric plasma regions of interest in this work, including both cold plasma populations with energies less than several electron-volts as well as energetic particles with energies greater than a kilovolt.

Ionosphere

The ionosphere forms the base of the plasma environment of the Earth. At altitudes above about 90 km, the tenuous neutral atmosphere becomes partially ionized by solar ultraviolet radiation. In addition, solar and galactic cosmic rays and energetic particles from the magnetosphere precipitate into the neutral upper atmosphere to

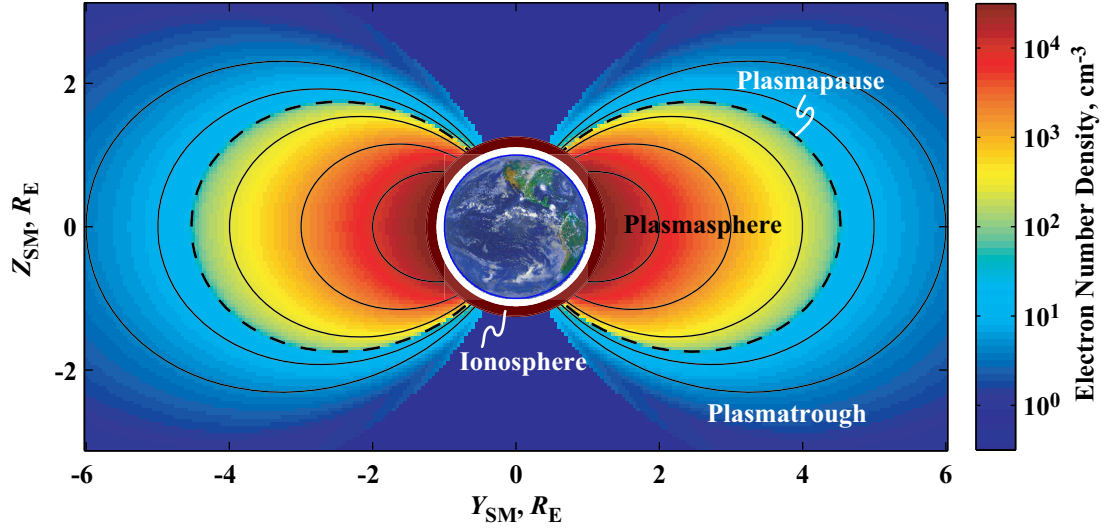


Figure 1.4. A model electron density distribution in the inner magnetosphere color coded on a log scale, with the plasmasphere, plasmopause and plasmatrough regions identified.

produce secondary ionization. This effect is particularly important at high latitudes and at night when photoionization ceases. The electron number density reaches a maximum of $\sim 10^6 \text{ cm}^{-3}$ at an altitude of $\sim 300 \text{ km}$ and decreases steadily above that into the magnetosphere. Ion and electron temperatures in the ionospheric are generally less than several tenths of an electron-volt.

The ionosphere is only partially ionized, and the density of neutral air molecules is relatively high so that collisions occur frequently between charged and neutral particles. On the other hand, above the ionosphere in most regions of the magnetosphere, collisions between particles occur infrequently, and thus the plasmas therein are generally treated as collisionless.

The ionosphere and the solar wind are the ultimate sources for the other magnetospheric plasma populations.

Plasmasphere

The plasmasphere is a toroidal region of cold plasma which encircles the Earth. Compared with other regions of the magnetosphere, the densities in the plasmasphere are

quite high, ranging from about 10 to 10^4 electrons cm^{-3} , as shown in Figure 1.4. The plasmasphere is populated by the outflow of ions and electrons from the underlying ionosphere along mid- and low-latitude geomagnetic field lines [e.g., *Lemaire*, 1989]. However, ion and electron temperatures in the plasmasphere are on average about three times higher than those in the ionosphere (on the order of 1 eV), possibly due to heating by plasma waves or Coulomb collisions with photoelectrons escaping from the ionosphere [*Comfort*, 1986; *Newberry et al.*, 1989]. Protons are the principal plasmaspheric ion species, followed by He^+ , O^+ and trace amounts of heavier ions with an equal number of electrons maintaining overall charge neutrality [*Comfort*, 1988]. Bulk plasma motion in the plasmasphere is primarily driven by the rotation of the Earth, and thus the plasmasphere is generally considered to corotate with the planet.

The plasmopause is an approximately field-aligned surface at the outer boundary of the plasmasphere at which there typically exists a sharp density gradient in the equatorial density profile on the order of a factor of five density decrease over less than $0.5 L$ [*Carpenter and Anderson*, 1992]. Outside the plasmopause in the plasmatrough, the cold plasma density drops to $\sim 1 - 10 \text{ cm}^{-3}$ (Figure 1.4).

In an average sense, the plasmasphere as viewed in the geomagnetic equatorial plane tends to be roughly circular with the plasmopause typically lying between $L \simeq 3$ and 5. However, since the time of the earliest studies of the plasmasphere, large scale ($1 R_E$ or greater) bulges in the equatorial plasmopause have been observed, especially in the dusk local time sector [*Carpenter*, 1966].

Radiation Belts and Ring Current

The radiation belts are energetic particles which occupy magnetic field lines in the range of $L=2$ to 7. They extend in energy from several keV up to as high as 10 MeV for electrons and 500 MeV for protons. These energetic particles are magnetically trapped in the mirror geometry of the Earth's field, executing helical gyro-motion around field lines and bouncing back and forth between conjugate hemispheres [*Walt*, 1994, Ch. 4]. They also undergo a slow azimuthal drift around the Earth as a result of the gradient and curvature magnetic drifts. A net westward current, known as the ring current, results from these drifts as the electrons drift eastward while the ions

drift westward. Although all trapped particles in the inner magnetosphere contribute to the ring current, only ions in the medium-energy range of ~ 10 keV to a few hundred of keV contribute substantially to the total current density. Electrons contribute little to the net current due to their negligible energy density [e.g. *Daglis et al.*, 1999].

Plasma Sheet

The plasma sheet [*Baumjohann et al.*, 1989] occupies the region of closed field lines in the equatorial magnetotail. It consists of ions and electrons with energies on the order of several keV and typical number densities of $\sim 0.1 - 1 \text{ cm}^{-3}$. The plasma sheet extends along geomagnetic field lines, reaching down to the nightside high-latitude ionosphere where precipitating plasma sheet particles collide with neutral atmospheric particles producing the visible aurora [*Chamberlain*, 1961].

1.2 Geomagnetic Activity

The solar wind carries a large amount of kinetic and electrical energy and momentum some of which can be transferred to the magnetosphere. Strong or sudden changes in the solar wind parameters, such as an increase in the velocity or density or a change in the interplanetary magnetic field (IMF) strength or direction, can cause a variety of geomagnetic disturbance activity within the magnetosphere. Energy can be transferred between the solar wind and the magnetosphere most efficiently when the IMF embedded in the solar wind and the Earth's magnetic field are oppositely directed [*Burton et al.*, 1975]. Thus, the vertical component of the IMF is of particular importance, and there is a well established correlation between southward IMF ($B_z < 0$) and the level of geomagnetic activity [*Murayama*, 1982]

Geomagnetic disturbances may last only several hours, such as in the case of an isolated substorm [*Akasofu*, 1964], or for several days, as in the case of a large magnetic storm [*Lui et al.*, 1987]. The most apparent manifestations of these disturbances are changes in the measured surface magnetic field strength of the Earth, resulting from enhancements in magnetospheric and ionospheric current systems as well as a brightening and expansion to lower latitudes of the visible aurora.

For example, the ring current can become quickly and substantially enhanced during geomagnetic storms as plasma sheet particles are transported Earthward and become trapped in the inner magnetosphere. A slow decay of the ring current occurs over several days as magnetospheric activity subsides. The global strength of the ring current can be monitored by ground-based magnetometers located at mid- and equatorial latitudes due to its diamagnetic effect on the surface field strength [Dessler and Parker, 1959]. The *Dst* magnetic index [Sugiura, 1964] calculated from these observations gives an estimate of the total energy content of the particles forming the ring current and can thus be used to monitor geomagnetic storms. Other frequently used magnetic indices include the *AE* index [Davis and Sugiura, 1966], an indicator of substorm activity which measures changes in the auroral electrojet current system in the ionosphere, and the *Kp* index [Bartels et al., 1939], a more general index which includes contributions from several current systems.

The size and shape of the plasmasphere is also strongly affected by the level of geomagnetic activity within the magnetosphere. Much of the dynamics of the plasmasphere are governed by the interplay between two plasma flow regimes in the inner magnetosphere, one driven by the rotation of the Earth and the other a global circulation pattern, referred to as global magnetospheric convection, driven by the solar wind during times of southward IMF (See Section 2.2). Empirical models of the plasmapause location [e.g., Carpenter and Anderson, 1992] show that the plasmasphere quickly shrinks during periods of enhanced geomagnetic activity and slowly grows or refills during recovery times. In the aftermath of strong magnetic activity, the plasmapause may be located at $L=2$, and plasmaspheric plasma may extend globally beyond $L=6$ after several days of low magnetic activity. Statistically, bulges in the dusk sector tends to be detected at earlier local times during periods of increased disturbance and at later local times (or not at all) during quiet periods [Carpenter, 1970].

1.3 Experimental Techniques

The plasmapause was initially discovered by two independent researchers using two quite different techniques, *in situ* observations of the electron number density [Gringauz, 1963] and ground-based “whistler” measurements [Carpenter, 1963]. These two techniques have continued to be used successfully for many decades to study the plasmasphere and plasmapause region.

Satellites can provide high time resolution measurements of the electron number density along the satellite orbit path. Density values can be extracted from data acquired with plasma wave receivers, as described in Section 3.2.1, or directly determined by particle detectors or Langmuir probes which may also be used to extract information on temperature and composition. *In situ* observations are well suited for the study of density structures of various scale sizes [*e.g.* Chappell, 1974; Moldwin *et al.*, 1995; Carpenter *et al.*, 2000]. However, in general it is difficult to obtain insight on the dynamic development of such density structures due to the typically long orbit periods (> 10 hours) of high altitude satellites. The large data sets produced by satellite missions have been used to develop empirical plasmasphere density and plasmapause location models such as the widely used Carpenter and Anderson [1992] model or newer models based on data from the CRRES satellite [Sheeley *et al.*, 2001; Moldwin *et al.*, 2002].

A whistler is a natural radio wave produced when impulsive very low frequency radiation from a lightning flash propagates through the dispersive plasma environment of the magnetosphere [Helliwell, 1965]. Analysis of the dispersion properties of whistler signals recorded at ground stations conjugate to regions of high lightning activity yields a variety of information on the electron density distribution in the magnetosphere [Carpenter and Smith, 1964; Park, 1972]. Whistlers received on the ground are guided along discrete magnetic field-aligned paths or ducts, which are believed to take the form of field-aligned density enhancements [Smith, 1961]. A typical lightning flash excites several of such ducts over a range of L values. The dispersion properties of most ground whistlers are such that a frequency of minimum time delay, or “nose” frequency, develops at a frequency proportional to the minimum magnetic

field value along the path. Measurement of the nose frequency indicates the approximate L value of the path, and travel time at that frequency provides a measure of the integrated electron density along the path [*Smith and Carpenter, 1961*]. The dispersion properties of whistlers are heavily weighted by the plasma environment along the higher-altitude (near equatorial) portion of the path where variations in the plasma parameters per unit distance along the field lines are minimal. As a result, whistlers provide a measure of the electron density near the magnetic equator that is relatively insensitive to the functional form of the distribution of plasma along the field lines used in the calculations [*Angerami and Carpenter, 1966*]. Therefore, instantaneous multi-point equatorial electron density profiles can be constructed from multi-component whistler measurements. Long observation periods allow for changes equatorial density and total flux tube content to be precisely tracked, and thus a particular strength of the whistler technique is the ability to determine cross- L bulk plasma motions in a frame of reference rotating with the Earth [*Carpenter and Smith, 2000*].

As detailed in Chapter 2, the plasmasphere has been studied extensively in the past using these and other experimental methods as well as theoretical techniques. Experimental research has revealed many complexities in both the structure and dynamics of the plasmasphere, but the ability to put observations into a global context has been limited [e.g., *Carpenter and Lemaire, 1997*]. On the other hand, numerical models have had some success in describing large scale plasmasphere features but generally tend to over-simplify many of the underlying physical processes.

The IMAGE satellite, with its unprecedented measurement capabilities, has brought about a resurgence of interest in the plasmasphere, its dynamics and interactions with energetic particle populations. In particular, the Extreme Ultraviolet Imager (EUV) (Chapter 3) is designed to study the plasmasphere by imaging the distribution of He^+ through its emission at 30.4 nm. EUV obtains an image encompassing the entire plasmasphere with a spatial resolution of about 650 km once every ten minutes and thus allows us for the first time to study the plasmasphere system from a global perspective.

1.4 Geophysical Importance of the Plasmasphere

The plasmasphere is a central element in many of the complex interactions within the magnetosphere, and thus knowledge of its dynamics on a global scale is important for a variety of reasons. First of all, the size and shape of the plasmasphere give an indication, although in a complex integral sense, of the recent time history of magnetospheric convection, an important global process within the magnetosphere. Convection in the inner magnetosphere is complex and not accurately described in the simple, but widely used, global models [e.g. *Volland, 1973; Stern, 1975*]. Secondly, the plasmasphere contains a large amount of mass, and during geomagnetic disturbances a significant amount of that mass is removed. Some of this plasma may be lost to the solar wind or the ionosphere or can be energized and redistributed within the magnetosphere. Finally, the cold plasma density is a fundamental parameter in the generation and propagation of plasma waves and the interaction of these waves with energetic particles. Wave-particle interactions play an important role in the loss (through precipitation into the upper atmosphere) of energetic particles and may also contribute to the storm-time acceleration of radiation belt electrons [e.g., *Koyzra et al., 1997; Horne, 2001*].

1.5 Contributions of this Research

This work explores several aspects of plasmaspheric dynamics during periods of enhanced geomagnetic activity. By tracking the location of the plasmopause in sequences of EUV images, we make quantitative measurements of radial and azimuthal motions of the boundary during various phases of geomagnetic disturbances. We examine inward motion of the plasmopause boundary on the nightside of the Earth, the formation and evolution of plasmaspheric “plumes”, and the tendency for mesoscale azimuthal irregularities in the plasmopause radius to develop in a specific local time sector (Chapter 4). A significant amount of mass is removed from the plasmasphere during these disturbance periods and in Chapter 5, we use the global images to make

estimates of this loss. Finally, we explore the the relationship between the plasmaspheric plume and regions of precipitating energetic protons (Chapter 6).

The major contributions of this research can be summarized as follows:

1. Established the relationship between *in situ* measurements of the steep plasmopause boundary and edge features observed in global extreme-ultraviolet images.
2. Carried out the first global quantitative measurements of azimuthal and radial motions of the plasmasphere during geomagnetic disturbances, verifying the predicted formation of plume-like structures in the afternoon local time sector.
3. Determined that azimuthal irregularities of the plasmopause boundary tend to form in a specific magnetic local time sector, located approximately between dawn and the western edge of the plasmaspheric plume, during geomagnetically disturbed conditions.
4. Quantified the total amount of plasma removed from the plasmasphere during five periods of enhanced geomagnetic activity.
5. Identified an association between a subauroral arc produced by precipitating energetic protons and a globally observed plasmaspheric plume.

Chapter 2

Background and Past Research

In this chapter, we review some relevant basic plasma physics concepts and simplifying assumptions generally used in studies of cold plasma, provide a preliminary description of bulk plasma motions in the magnetosphere, and review past research on the structure and dynamics of the plasmasphere.

2.1 Frozen-in Magnetic Flux

A few key concepts underlying space plasma physics are reviewed in this section, while for a more complete introduction the reader is referred to *Baumjohann and Treumann* [1997] and *Parks* [1991]. While there are several levels of theoretical descriptions of plasma phenomena, in magnetospheric physics a magnetohydrodynamic (MHD) approach is often adopted to describe low energy and large scale phenomena. In an MHD formulation, the plasma is treated as a single conducting fluid with macroscopic variables such as average density, velocity and temperature. The set of MHD equations includes the continuity equation, the momentum equation, Maxwell's equations and the generalized Ohm's law.

MHD theory assumes that the plasma is a good conductor and that therefore free charges do not accumulate within the fluid. In addition, the displacement current is considered negligible compared to the conduction current, resulting in the modified

Maxwell's equations given below:

$$\nabla \times \mathbf{E} = -\frac{\partial \mathbf{B}}{\partial t} \quad (2.1)$$

$$\nabla \cdot \epsilon_0 \mathbf{E} = 0 \quad (2.2)$$

$$\nabla \times \mathbf{B} = \mu_0 \mathbf{J} \quad (2.3)$$

$$\nabla \cdot \mathbf{B} = 0 \quad (2.4)$$

A simplified form of the generalized Ohm's law can be expressed as

$$\mathbf{J} = \sigma_0(\mathbf{E} + \mathbf{u} \times \mathbf{B}) \quad (2.5)$$

where \mathbf{u} is the bulk plasma velocity and σ_0 is the electrical conductivity. This equation describes the electrical current constituted by the motion of plasma under the influence of fields \mathbf{E} and \mathbf{B} . It is valid in fully ionized magnetospheric plasmas where the typical collision frequencies are low and the plasma conductivity is high. It is not valid, for example, in the lower part of the ionosphere where frequent collisions in the presence of a strong magnetic field lead to an anisotropic conductivity tensor.

In studies of low energy magnetospheric plasmas, the motion of the plasma and the magnetic field lines are interconnected. In order to examine their relationship we can examine the temporal variation of the magnetic field \mathbf{B} in a conducting fluid. By taking the curl of Ohm's law (2.5) and replacing \mathbf{J} and $\nabla \times \mathbf{E}$ using Maxwell curl equations (2.2) and (2.4), we obtain

$$\frac{\partial \mathbf{B}}{\partial t} = \nabla \times (\mathbf{u} \times \mathbf{B}) + \frac{1}{\mu_0 \sigma_0} \nabla^2 \mathbf{B} \quad (2.6)$$

The first term on the right hand side of Equation (2.6) is known as the flow term while the second term is called the diffusion term. In most MHD problems either one or the other of these terms tends to dominate. For example, if the plasma is at rest ($\mathbf{u} = 0$) the flow term is dropped. The magnetic field slowly diffuses across the plasma smoothing out any local inhomogeneities. The finite conductivity results in Ohmic losses and the magnetic field eventually decays away as magnetic energy is

converted to plasma energy.

On the other hand, when the conductivity is extremely large, the idealized approximation of a perfectly conducting fluid, in which the conductivity approaches infinity, is often used. Neglecting the second term of Equation (2.6) leads to the “frozen-in” flux theorem [e.g. *Parks*, 1991, pp. 162 – 167] which states that the flux of magnetic field through any closed contour moving with the fluid is constant and that fluid elements that lie on a magnetic field line remain on that same field. Therefore, the magnetic field lines are considered to be “frozen” into the fluid. Plasma can flow freely parallel to the magnetic field, but any bulk motion perpendicular to the magnetic field carries the magnetic field lines with the plasma. In studies of low energy magnetospheric plasmas as well as the solar wind, the approximation of infinite conductivity and therefore frozen-in flux is generally considered to be valid over most time scales of interest.

The approximation of infinite conductivity yields the ideal MHD formulation in which Ohm’s law reduces to

$$\mathbf{E} = -\mathbf{u} \times \mathbf{B} \quad (2.7)$$

This relationship implies that an observer at a fixed location would observe an electric field as a result of the convecting plasma. Although the notion that bulk motion in the magnetosphere is driven by electric fields is widely held, *Vasyliūnas* [2001] has recently emphasized that the plasma motion is in fact the fundamental parameter, and thus that electric fields are consequences of the flows and not vice versa. The ideal MHD approximation implies that magnetic field lines are electric equipotential lines ($\mathbf{E} \cdot \mathbf{B} = 0$), i.e., that there are no magnetic field aligned electric potential drops. In the cold plasma approximation, generally used in studies of the plasmasphere, the plasma temperature is assumed to be zero so that the gradient and curvature magnetic drifts, which are proportional to the energy of the particles, as well as gravitational drifts are generally ignored. Thus, the electric equipotential surfaces are parallel to the cold plasma flow.

2.2 Bulk Plasma Motion

There are two main external forces which drive the bulk motion of cold plasma within the magnetosphere. The first is the daily rotation of the Earth and the second is the kinetic energy of the solar wind.

2.2.1 Corotation

Neutral atmospheric particles rotate with the Earth as a result of frictional drag, and thus the ionosphere is also forced to corotate due to frequent ion and electron-neutral collisions. Although the ionosphere is not completely frozen-in due to the high collision frequency and thus finite conductivity, in the absence of other forces, ionospheric flux tubes and their magnetospheric extension also tend to corotate with the Earth. This condition is typically valid in the low and mid-latitude ionosphere [Hines, 1961].

The corotation of plasma and flux tubes is, for a non-rotating observer, equivalent to an electric field of

$$\mathbf{E}_{\text{cor}} = -(\boldsymbol{\Omega}_{\text{E}} \times \mathbf{r}) \times \mathbf{B} \quad (2.8)$$

where $\boldsymbol{\Omega}_{\text{E}}$ is the angular velocity of the Earth. Using the simplifying assumption of a dipole magnetic field centered on the Earth's rotation axis, in the equatorial plane \mathbf{E}_{cor} is directed radially inward toward the Earth and falls off as $1/r^2$.

2.2.2 Convection

The second main driver of bulk plasma motion in the magnetosphere is the solar wind. Since the solar wind is frozen to the interplanetary magnetic field while the plasma surrounding the Earth is frozen to its field, when these two plasmas meet, they should not mix but instead form two distinct regions separated by a thin current sheet. However, the frozen-in condition can break down in this current sheet, and within a relatively small diffusion region, oppositely directed interplanetary and terrestrial field lines can merge across the boundary [Baumjohann and Treumann, 1997, pp. 73 – 82].

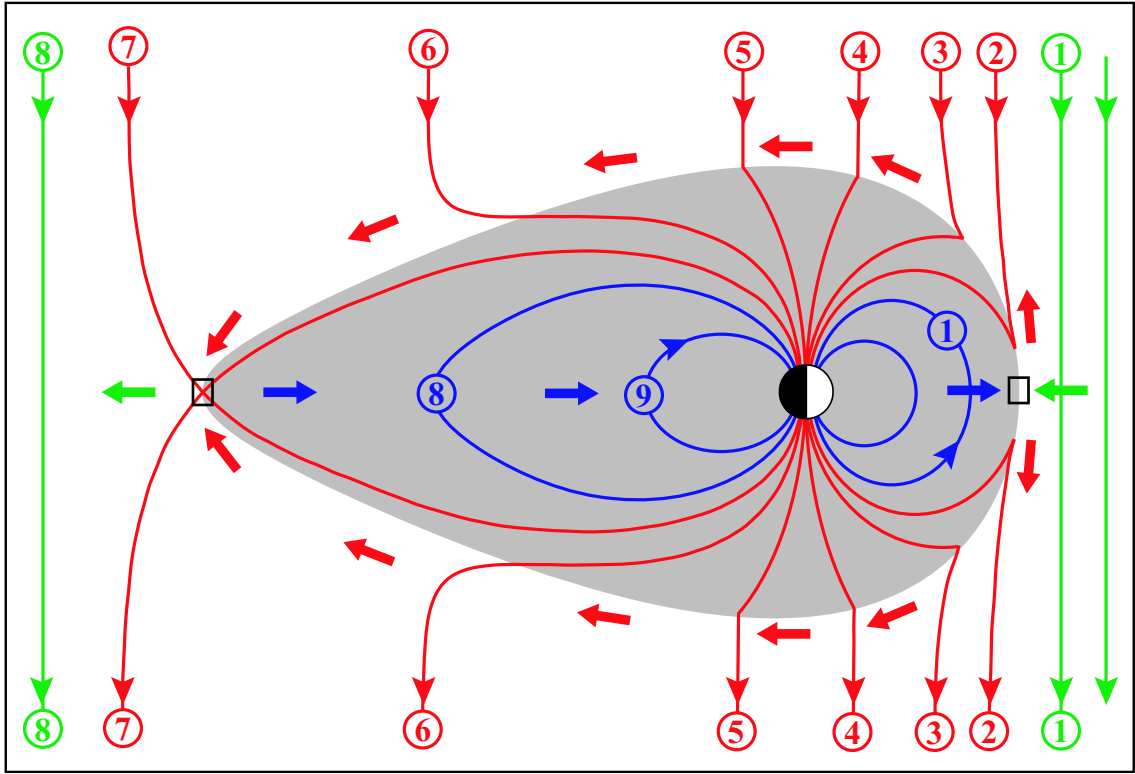


Figure 2.1. Schematic diagram of magnetic field line merging and the resulting convection of plasma flux tubes. Adapted from Figure 5.4 of *Baumjohann and Treumann* [1997].

As shown in Figure 2.1, this process of magnetic field line merging or reconnection [Dungey, 1961] can occur when a southward directed interplanetary field line (denoted by the green field line labeled 1) encounters a northward directed terrestrial field line (blue field line labeled 1) at the equatorial magnetopause. Within the diffusion region (black square), the two field lines merge and split into two open field lines, (labeled 2) each of which has one footprint on the Earth and the other stretching out into the solar wind (eventually reaching back to the Sun). The solar wind transports these merged field lines across the polar cap and down the magnetotail (labeled 3 – 6). At a distance of ~ 100 to $200 R_E$ downtail, the two open field line halves meet and reconnect again in a small diffusion dominated region (labeled 7). Due to magnetic tension and pressure gradients, the stretched tail field line begins to move Earthward (labeled

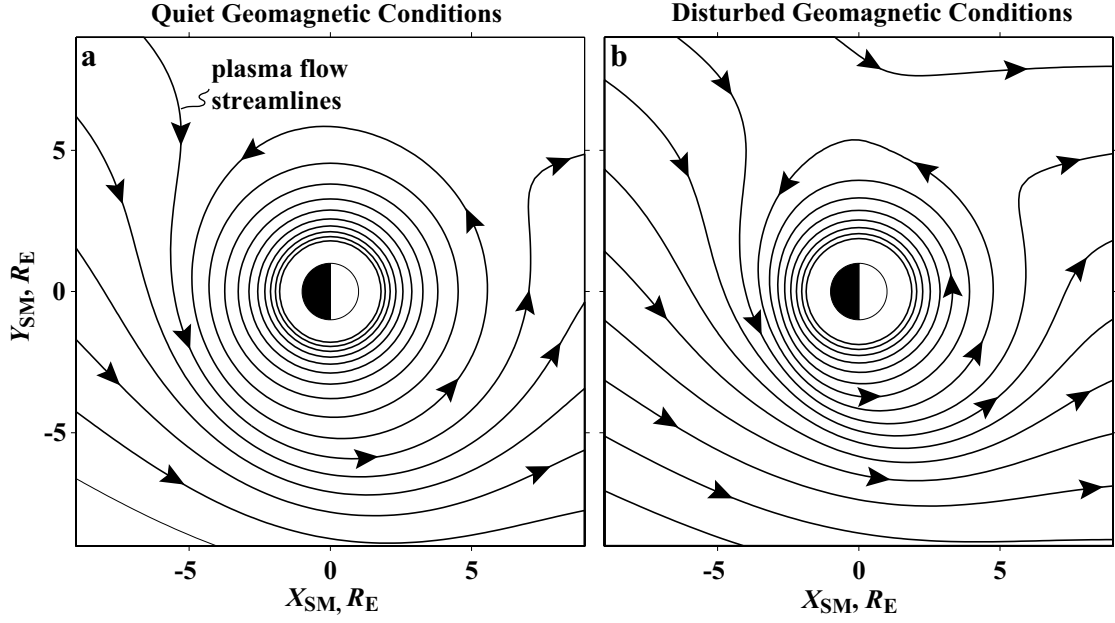


Figure 2.2. Equipotential contours of the E5D equatorial electric field model for two levels of geomagnetic activity, (a) $Kp = 2$ and (b) $Kp = 7$. The equipotential lines are equivalent to plasma flow streamlines for zero energy particles.

8–9), and this field line is eventually brought back to the frontside magnetosphere (labeled 1). The magnetospheric sunward return flow (blue arrows) is referred to as global magnetospheric convection. It should be noted that while magnetic field line merging is one of the most poorly understood processes in space plasma physics [e.g., Vasyliūnas, 1975], the magnetospheric consequences of this process, including but not limited to the flow cycle described above, are well documented [e.g., Burch, 1983].

Like corotation, magnetospheric convection can also be expressed in terms of an electric field. Convection electric fields are generally modeled as potential fields, $\nabla \times \mathbf{E} = 0$ and $\mathbf{E} = -\nabla\Phi$, with the potential Φ assumed to be constant along the field lines. The simplest equatorial convection model assumes a spatially uniform dawn-to-dusk electric field:

$$\mathbf{E}_{\text{con}} = E_0 \hat{\mathbf{y}} \quad (2.9)$$

where the magnitude E_0 is generally less than 1 mV/m.

2.2.3 Global Convection Models

By combining the effects of corotation and convection, simple models of the inner magnetospheric electric field can be constructed. Figure 2.2 shows potential patterns from the so-called E5D model, a semi-empirical equatorial electric field model for two levels of geomagnetic activity [McIlwain, 1986]. During quiet geomagnetic conditions (Figure 2.2a), corotational flows dominate the inner magnetosphere as indicated by the concentric circles. The contours further away from the Earth are open and the flow is dominated by the solar wind induced convection. During times of increased geomagnetic activity (Figure 2.2b), the strength of convection increases, and the region dominated by corotation shrinks. Note that on the dawn side, corotational and convective flows are generally in the same direction, whereas they oppose each other on the dusk side.

Shielding

In addition to the effects of corotation and convection, most electric field models (including the E5D model shown in Figure 2.2) include the effect of shielding [Jaggi and Wolf, 1973]. When the plasma sheet moves Earthward in response to enhanced convection, a zonal charge separation is created as energetic electrons drift dawnward and energetic protons drift duskward around the Earth. The polarization electric field associated with this charge separation is directed from dusk to dawn and thus acts to shield the inner magnetosphere from the full dawn-to-dusk cross tail convection electric field. Shielding takes a finite time to be established, and changes in the convection field or other magnetospheric parameters can cause it to be ineffective for extended periods.

2.3 Past Research on Plasmaspheric Dynamics

2.3.1 Early Discoveries

The existence of a sharp outer boundary of the plasmasphere or plasmopause was first discovered in the early 1960's [Carpenter, 1963; Gringauz, 1963]. Analysis of whistler

waves recorded at ground stations established the plasmapause as a permanent feature within the magnetosphere and also showed the tendency for the plasmapause to move inward during periods of increased magnetic activity [*Carpenter*, 1963]. Further studies showed that the plasmasphere not only shrank but became asymmetric with a bulge in the dusk sector during periods of disturbance whereas during quiet times the plasmasphere expanded and tended to become more circular [*Carpenter*, 1966]. Also, while the plasmasphere appeared to move at the same angular velocity as the Earth, i.e. corotated, in the local time sector from 00 to 17 MLT, its motions were more “confused” in the dusk to midnight quadrant.

2.3.2 Basic Plasmaspheric Dynamics

In response to the first reports from whistlers on the global shape of the plasmasphere and its variations with magnetic disturbance, *Nishida* [1966] and *Brice* [1967] proposed a steady state model which explained the formation of the plasmapause in terms of the interplay between the corotation and convection flows within the inner magnetosphere. These models defined the steady state plasmapause as corresponding to the last closed (i.e., Earth encircling) equipotential of the combined flow with the bulge resulting from a region of stagnation in the dusk sector. These early models, later modified to account for the unsteady nature of convection, provide important insight into why the region exterior to the plasmasphere is low in density and why the plasmasphere should diminish in overall size during periods of increased magnetic disturbance.

If quiet geomagnetic conditions persist for several days (Figure 2.2a), flux tubes following the roughly circular paths enclosing the Earth can be slowly filled by the outflowing ionospheric plasma. Eventually, a diffusive equilibrium distribution of plasma along the magnetic field lines is established resulting from a combination of centrifugal and gravitational forces [*Angerami and Thomas*, 1964]. A sharp plasmapause density gradient may not necessarily be present during long periods of quiet, but instead the profile may decrease gradually with distance.

Even under quiet geomagnetic conditions, a weak convective flow dominates the

trajectories of the cold plasma outside some distance. Convection during quiet conditions may be due to a viscous interaction between the magnetosphere and solar wind [Axford and Hines, 1961]. Although ionospheric outflow still occurs at these latitudes, flux tubes drifting in from the magnetotail do not have the opportunity to be filled to plasmaspheric levels before drifting out to the dayside boundary layers.

If the strength of magnetospheric convection increases due to a southward turning of the IMF (Figure 2.2b), particles that were previously on the outermost closed trajectories suddenly find themselves on open trajectories and drift toward the dayside magnetopause. Thus, the outer layers of the plasmasphere are stripped away and the plasmasphere shrinks.

In the aftermath of a disturbance, the plasmasphere begins the slow process of refilling as corotational flows once again dominate. While the inner plasmasphere may be expected to approach a diffusive equilibrium with the underlying ionosphere much of the time, the outer plasmasphere is more likely to be in a state of partial refilling due to the long refilling times and continually recurring geomagnetic storm and substorm activity [Park, 1974].

It is widely accepted that the plasmapause is essentially the boundary of the region where low energy plasma rotates with the Earth and that beyond it convection overpowers corotation [e.g. Parks, 1991, pp. 229 – 237; Wolf, 1995, pp. 314 – 317]. However, Lemaire [1975; 2001] has suggested that the plasmapause is the limit beyond which cold plasma is easily lost through the interchange instability. Lemaire [2001] proposes that a new sharp density gradient is formed in the post-midnight local time sector as a result of convective instabilities and interchange motion which, in conjunction with enhanced magnetospheric convection, act to pull out and peel off the outer layers of the plasmasphere.

2.3.3 Departures from Corotation

Even at times of quiet magnetic conditions, the plasmasphere may not strictly corotate with the Earth. Quiet day cross- L drift motions of flux tubes in the outer plasmasphere were shown in whistler studies to exhibit a generally repeatable diurnal

pattern [Carpenter and Seeley, 1976]. The cross- L flow near $L = 4$ is characterized by relatively slow outward drifts near midnight ($\sim 0.06 R_E$ per hour), slightly faster outward drifts in the morning sector (~ 0.11 to $0.17 R_E$ per hour), and a reversal to inward flows in afternoon ($\sim 0.17 R_E$ per hour). These plasmaspheric drifts were associated with the solar quiet (Sq) ionospheric current system which is produced by solar heating and tidal oscillations in the atmosphere [Carpenter, 1978].

Slight departures from corotation in the azimuthal direction are not easily detected with the whistler technique since the viewing area of a given ground station generally spans about 30° in longitude. However, azimuthal features observed in EUV global images of the plasmasphere and described as “bite-outs” can persist for long durations under quiet conditions, allowing their rate of rotation to be carefully tracked. Sandel [2003] studied thirteen such events and found that averaged over the lifetime of the feature, the rotation rates were between 77 % and 93 % of corotation.

2.3.4 Reduction in the Plasmapause Radius

Previous experimental work has indicated that the reduction in the plasmapause radius during periods of disturbance occurs primarily in the post-midnight sector. Using *in situ* ion density profiles Chappell *et al.*, [1970a] showed that the plasmapause position on the nightside (22 to 06 MLT) was closely correlated with the average magnetic activity over the preceding 2 to 6-hour period. The plasmapause moved to a lower L and the plasmapause density profile was found to steepen in that sector in response to increasing magnetic activity. On the other hand, the plasmapause position on the dayside (06 to 15 MLT) did not immediately respond to changes in magnetic activity, but its position depended instead on the level of activity present when that region previously corotated through the nightside region [Chappell *et al.*, 1971].

In addition, Carpenter *et al.* [1979] characterized cross- L drift patterns during the expansion phase of substorms near $L = 4$ and found that rapid inward drifts were detected approximately from midnight to dawn, with the fastest drift being of order $0.5 R_E$ per hour in the post-midnight sector and weakening with increasing local

time. However, in the aftermath of an isolated substorm, a reversal to outward drifts in the 02 to 05 MLT sector was frequently observed with a duration and amplitude comparable to the previous inward motion [*Carpenter et al.*, 1972]. Thus, during isolated substorms, the plasmopause radius might be locally modulated but might not have a globally reduced average radius. Sustained activity for periods of 10 or more hours appeared to be necessary to significantly reduce the overall size of the plasmasphere [*Carpenter et al.*, 1972].

2.3.5 Duskside Bulge and Detached Plasma Regions

The dynamic behavior of the duskside bulge was first revealed in whistler studies during magnetospheric substorms [*Carpenter*, 1970]. The westward edge of the bulge was generally observed to be quite abrupt with an increase in the plasmopause radius of 0.5 to 2.5 R_E within about an hour of local time, while the radius on the eastern edge decreased more smoothly with increasing local time. The bulge was observed at earlier local times with increasing levels of magnetic disturbance, assumed to be due to strong westward flows resulting from enhanced convection. In the aftermath of a substorm, the bulge was observed at later local times, a feature interpreted to be the result of the increased influence of the Earth's rotation during periods of quieting.

In addition, regions of high-density cold plasma were first observed outside the plasmasphere by the OGO spacecraft [*Chappell et al.*, 1970b]. In a statistical analysis of such events [*Chappell*, 1974], these so-called detached plasma regions were identified as being outside the main plasmopause and having a density above a specified threshold (100 cm^{-3} at $L = 4$ and reduced by L^{-4} for higher L to account for the increase in flux tube volume). They were found across the entire dayside of the magnetosphere during moderate to disturbed magnetic conditions with a peak occurrence in the afternoon-dusk sector. These detached regions tended to be located near the plasmopause at dusk and progressively farther away at earlier local times. They were variable in size, ranging from $< 0.1 L$ to $> 1 L$ in extent, and tended to exhibit extensive fine scale (50 to 200 km) density structure. Such regions were interpreted as being peeled off (and hence detached) from the plasmasphere near dusk and subsequently

drifting outward and westward toward the magnetopause.

Numerical models have been used extensively to understand the observations of the dusk-side plasmasphere (for a comprehensive review see [*Lemaire and Gringauz, 1998*]). Ideal MHD models typically use a parametrized electric potential distribution, which includes the effects of the corotational electric field and the solar wind driven convection electric field, to calculate the temporal evolution of the plasmopause by following the $\mathbf{E} \times \mathbf{B}$ drift trajectories of plasma flux tubes from an initial location. An early model by *Grebowsky* [1970] assumed that the initial plasmopause location corresponded to the last closed equipotential in a combined corotation and uniform dawn-dusk convection field, resulting in a “tear-drop” plasmasphere with a bulge in the dusk sector. In response to a step increase in the strength of convection, the bulge rotates westward and portions of the outer plasmasphere on the dayside are transported sunward, forming a plasmaspheric plume in the afternoon local time sector. Sometimes referred to as plasma tails, these plumes contain material eroded from the main plasmasphere and extend toward the magnetopause. *Chen and Grebowsky* [1974] used a similar model to show that the observations of detached density structures in the noon to dusk quadrant might in fact be crossings of satellites through such plumes, so that the so-called detached regions may be on a global scale attached to the plasmasphere. In response to a decrease in convection, the modeled plume or bulge would then rotate eastward and possibly wrap around the Earth [e.g. *Chen and Wolf*, [1972]; *Kurita and Hayakawa*, 1985]. It should be noted that the details of the temporal development of the plume in various models depend strongly on the assumed initial plasmasphere shape and the details of the modeled convection field.

The existence of plasmaspheric plumes was directly verified when the first global images of the plasmasphere using the IMAGE EUV instrument were published [*Burch et al.*, 2001; *Sandel et al.*, 2001] and the dynamic development of these observed features is examined in Chapter 4.

2.3.6 The Loss of Plasmaspheric Plasma

A significant amount of material can be removed from the plasmasphere during periods of enhanced geomagnetic activity. Global convection acts to remove the outer layers of the plasmasphere, and significant reductions in the electron density have been observed on flux tubes interior to the new plasmapause boundary as well. Using whistler data during a geomagnetic storm on June 15, 1965, *Park* [1970] estimated that $\sim 3 \times 10^{31}$ electrons and ions were removed from the plasmasphere, more than half the plasma stored in the quiet time plasmasphere, based on removal of essentially all plasma in a belt extending globally from $L = 3.5$ to 5.

Effects of Convection

Global convection models predict that the outer portions of the plasmasphere are convected to the dayside magnetopause and are supported by observations of the duskside bulge as well as by direct measurements of sunward flows of cold, dense plasma at geosynchronous orbit during magnetic storms [e.g. *Lennartsson and Reasoner*, 1978].

Global convection may be aided by fast but latitudinally narrow westward flow channels that develop in the subauroral ionosphere. These flow channels were recently collectively termed subauroral polarization streams (SAPS) [*Foster and Burke*, 2002]. SAPS are believed to result from a coupling between the inner edge of the plasma sheet and the poorly conducting nightside subauroral ionosphere [e.g. *Anderson et al.*, 2001]. On average, the SAPS region in the ionosphere is below the auroral oval, extends $\sim 3 - 5$ degrees in invariant latitude and is concentrated most strongly in the dusk and pre-midnight sectors [*Foster and Ho*, 2002]. When mapped out to the equatorial plane, the flow channel would be $\sim 2 R_E$ in radial extent and may harbor westward flows as fast as several kilometers per second. SAPS may significantly increase the rate of plasma transport from the duskside plasmasphere to the dayside magnetosphere during geomagnetic disturbances [*Goldstein et al.*, 2003d].

Once the eroded plasmaspheric material reaches the outer dayside magnetosphere it may enter the boundary layers or if convection weakens, it may become trapped in

the afternoon-dusk sector of the outer magnetosphere [*Carpenter et al.*, 1993]. Plasmaspheric plasma entering the dayside boundary layers is heated and accelerated to energies of $\sim 1-2$ keV [*Fuselier et al.*, 1989]. The plasma becomes entrained in the strong anti-sunward flow and may be swept back along the flanks of the magnetosphere in the low latitude boundary layer or may cross the magnetopause and be transported on reconnected field lines over the polar cap and down the magnetotail [*Freeman et al.*, 1977]. While some of this heated plasmaspheric plasma may be lost to the solar wind, some of it may eventually populate the plasma sheet. Calculations by *Borovsky et al.* [1997] suggested that material removed from the outer plasmasphere could account for observations of the “super-dense” plasma sheet ($> 2 \text{ cm}^{-3}$). Once in the plasma sheet, the former plasmaspheric material may precipitate into the auroral zone or be recirculated as ring current.

Losses to the Ionosphere

Just inside the new plasmapause boundary, whistler data have shown reductions in density ranging from a factor of ~ 1 to 3 in the aftermath of a disturbance [e.g. *Park and Carpenter*, 1970; *Carpenter et al.* 1993]. Flux tubes inside the shrinking plasmapause remain on closed drift paths and thus losses are likely not due to convection. In order to explain this density reduction as well as nighttime enhancements in the electron density of the mid-latitude ionosphere, *Park* [1971] proposed a draining of the flux tubes along the magnetic field lines and dumping of plasma into the ionosphere. In the topside ionosphere where the O^+ concentration decreases rapidly with altitude, the downward component of the cross- L drift (inward at the equator) results in a reduced O^+ concentration at a given altitude. Below a critical altitude, where H^+ is in chemical equilibrium with O^+ , a reduction in O^+ must be accompanied by a reduction in H^+ . Thus a downward flow of H^+ is induced from the plasmasphere.

2.3.7 Irregular Density Structure

Although empirical plasmasphere density models [e.g., *Carpenter and Anderson*, 1992; *Gallagher et al.*, 2000; *Sheeley et al.*, 2002] treat the radial density profile and azimuthal plasmapause shape as smoothly varying, the plasmasphere has been found to be highly irregular on a wide range of scale sizes. Early whistler studies inferred the existence of longitudinal ripples on the dayside plasmapause, consisting of peak to valley variations in the plasmapause radius of as much as $0.4 R_E$ within less than an hour of local time [*Angerami and Carpenter*, 1966]. More recently, these types of mesoscale features have been observed globally by the EUV imager [*Green et al.*, 2002; *Goldstein*, 2002], but much remains to be learned about the mechanisms of their formation.

High resolution *in situ* data has shown that the outer plasmasphere and plasmapause regularly exhibit fine scale (< 1000 km) density irregularities [e.g. *Carpenter*, 1993]. In a statistical study of CRRES data, *LeDocq* [1994] found that density irregularity amplitudes of at least 10 % occurred 50 % of the time between $L = 2.5$ and 4. At geosynchronous orbit, the level of variability in ion density structures was found to increase with increasing geomagnetic activity [*Moldwin*, 1995].

Chapter 3

Observational Techniques

3.1 IMAGE Satellite Overview

The Imager for Magnetopause-to-Aurora Global Exploration (IMAGE) mission [Burch, 2000] was the first satellite mission dedicated to imaging the Earth’s magnetosphere. IMAGE employs ultraviolet imaging, neutral atom imaging as well as radio techniques to produce comprehensive global images and thus observe, in an unprecedented fashion, the large-scale dynamics of the magnetosphere and the interactions among its constituent plasma populations. The IMAGE spacecraft was launched on March 25, 2000 into a highly elliptical polar orbit with initial apogee at a geocentric radial distance of $8.22 R_E$ in the northern hemisphere and an initial perigee altitude of 1000 km in the southern hemisphere. The orbit period is ~ 14 hours, and the spacecraft has a spin period of 2 minutes with the spin axis perpendicular to the orbital plane.

The two instruments intended for investigations of the plasmasphere are the Extreme Ultraviolet Imager (EUV) and the Radio Plasma Imager (RPI). Figure 3.1 shows an example IMAGE orbit from June 10, 2001 from 03:40 UT to 18:00 UT when the satellite was approximately in the dawn–dusk plane. For ~ 9 hours centered on apogee, the EUV instrument obtains global images of He^+ distribution in the plasmasphere (shown in Figure 3.1 as the portion of the orbit between 04:30 UT and 13:30 UT). For the subsequent ~ 3 hours around perigee, RPI can use active radio sounding as well as passive *in situ* techniques to measure the electron number density

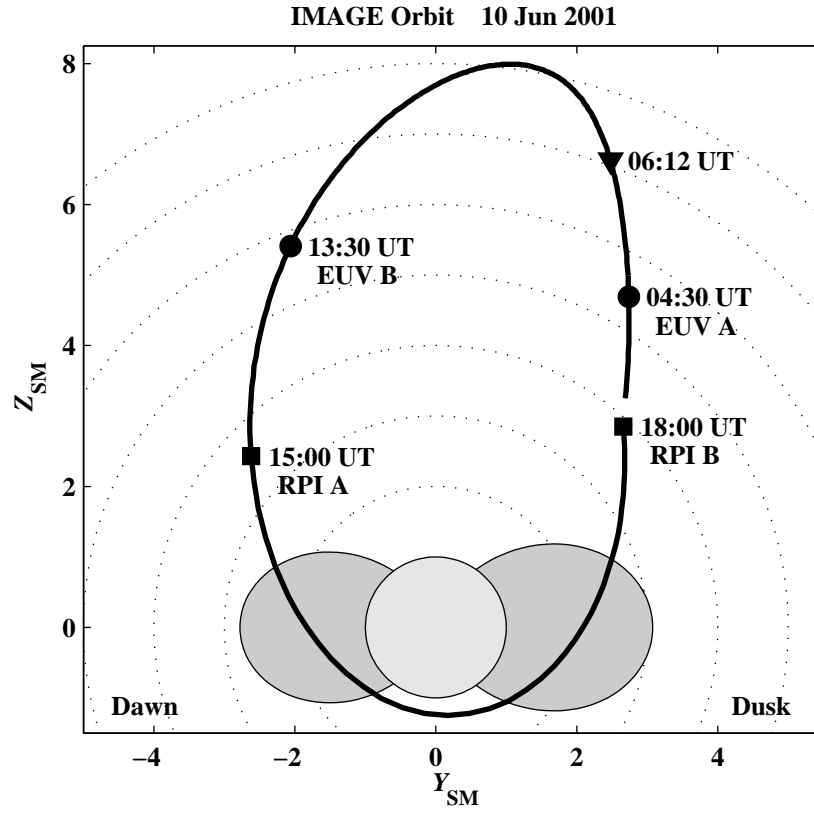


Figure 3.1. An orbit of the IMAGE satellite from June 10, 2001 projected into YZ_{SM} meridional plane. The portion of the orbit over which EUV (RPI) observes the plasmasphere is shown as the portion of the orbit between the points labeled EUV A (RPI A) and EUV B (RPI B). The approximate size of the plasmasphere as observed *in situ* by RPI is indicated by the shaded dipole region.

within and beyond the plasmasphere (shown as the portion of the orbit between 15:00 UT and 18:00 UT).

3.2 Radio Plasma Imager

The RPI instrument [Reinisch *et al.*, 2000] is a low-power radar which operates in the radio frequency bands which contain the plasma resonance frequencies characteristic of the Earth's magnetosphere. RPI can locate regions of various plasma density by observing radar echoes from the plasma that are reflected where the radio frequency

meets cutoff conditions for the various propagating ordinary, extraordinary, and z-modes or at the altitude of steep density gradients in the bottom-side ionosphere for the whistler mode.

RPI is a multi-mode instrument in which sounding and listening frequencies, range detection, pulse characteristics and repetition rate are adjustable parameters over a wide range of values. The instrument covers the frequency range from 3 kHz to 3 MHz with a receiver bandwidth of 300 Hz. There are three orthogonal thin-wire antennas, consisting of two 500-m tip-to-tip dipoles in the spin plane (X and Y) and a 20-m tip-to-tip dipole along the spin axis (Z). The long dipoles are used for transmission, and all three antennas are used for reception. The nominal radiated power from RPI, variable (in terms of free space mode excitation) from 0.1 mW at low frequencies to ~ 10 W per dipole at 200 kHz, was reduced by 3 dB on May 8, 2000 when the power supply for the Y axis transmitter failed. A further 3 dB reduction occurred on October 3, 2000, when one of the X axis monopoles was partially severed, apparently by a micrometeorite.

An important result of the active sounding is the identification of small-scale field-aligned density structures within and beyond the plasmasphere [Carpenter *et al.*, 2002]. During sounding of the plasmasphere from both outside and inside the plasmopause, RPI echoes that follow non-field-aligned ray paths are usually not the discrete traces on range-versus-frequency records that are predicted by ray-tracing simulations using smooth magnetospheric density models. Instead, such RPI echoes exhibit various amounts of spreading, from ~ 0.5 to $2 R_E$ in virtual range (defined as the range assuming speed of light propagation). The range spreading is attributed to scattering from, partial reflection from, and propagation along geomagnetic-field-aligned electron density irregularities.

In addition to the active sounding, RPI also makes passive measurements of the local plasma wave environment. Figure 3.2 show a dynamic spectrogram from June 10, 2001 taken over the portion of the orbit between the points labeled RPI A and RPI B in Figure 3.1. The record was obtained by sweeping the 300-Hz bandwidth RPI receiver through 243 frequency steps between 3 kHz and 1 MHz. The interval of 3 kHz – 20 kHz was covered by 44 steps of 400 Hz, while another 199 frequency steps

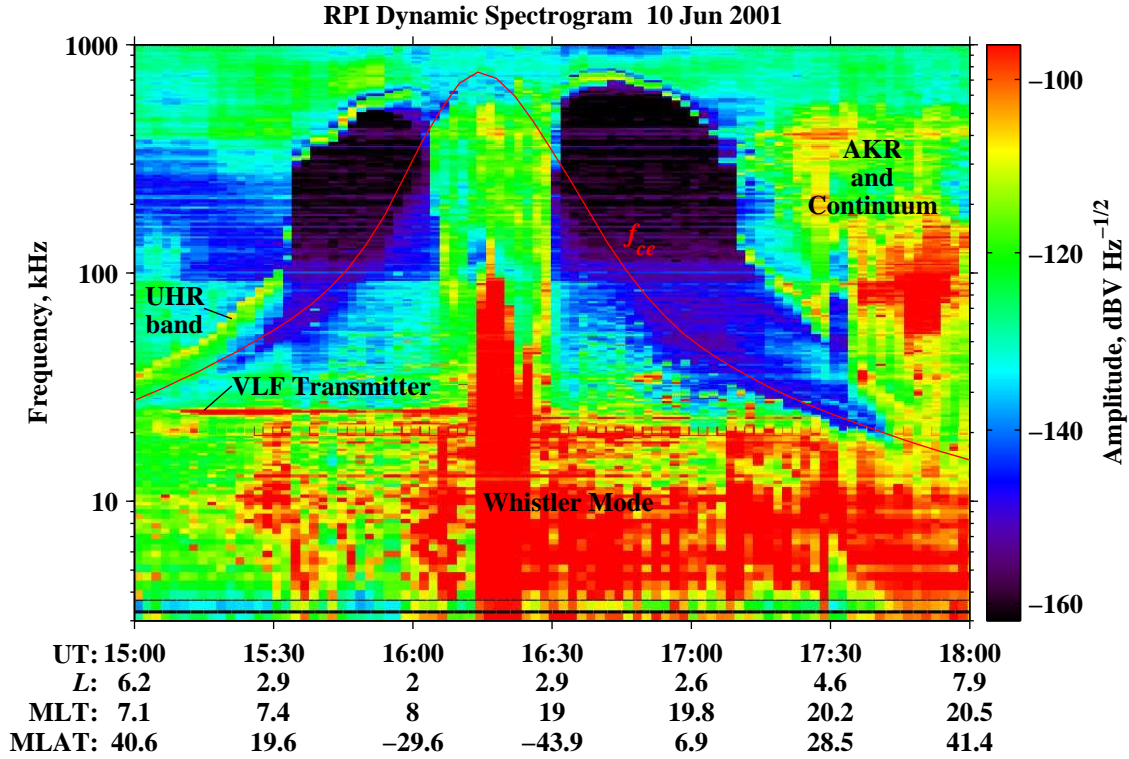


Figure 3.2. RPI dynamic spectrogram from June 10, 2001 showing a typical pass through the plasmasphere. The orbital parameters L , magnetic local time, and magnetic latitude are shown as well.

(2% increments) covered the 20 kHz – 1 MHz interval. At each frequency step, RPI sampled the receiver amplitude 36 times at 3.2 ms intervals and calculated a series of eight 25.6 ms running averages. In this way, transient signals tend to be suppressed and relatively steady signals such as local resonances and continuum radiation are emphasized. A frequency sweep is run every 2 to 6 minutes, each sweep taking about 1 minute to complete.

In Figure 3.2, the solid red curve indicates the cyclotron frequency estimated from the T96 magnetic field model [Tsyanenko and Stern, 1996]. The T96 model has an uncertainty of a few percent in quiet times and an order of magnitude during storm periods. The strong emissions at frequencies generally below the cyclotron frequency are whistler mode signals, and between ~ 20 –40 kHz VLF transmitters can be seen as discrete horizontal lines. The frequency banded emission above the cyclotron

frequency is the upper hybrid resonance (UHR) noise band from which estimates of the electron density can be made as described below. Above the UHR band, auroral kilometric radiation (AKR) and continuum radiation can be observed.

3.2.1 Deriving Electron Density from UHR Measurements

We use the technique described by *Mosier et al.* [1973] to derive electron number density profiles from the intense plasma noise bands typically observed near the upper hybrid frequency. The upper hybrid frequency is a combination of the electron cyclotron frequency, f_{ce} , and the electron plasma frequency, f_{pe} .

$$f_{uh} = \sqrt{f_{pe}^2 + f_{ce}^2} \quad (3.1)$$

The electron cyclotron frequency is a function of the magnetic field strength, B ,

$$f_{ce} = \frac{|q_e|B}{2\pi m_e} \quad (3.2)$$

and the electron plasma frequency is a function of the electron number density, n_e ,

$$f_{pe} = \frac{1}{2\pi} \left(\frac{n_e q_e^2}{m_e \epsilon_0} \right)^{1/2} \quad (3.3)$$

where q_e is the charge of electron, m_e is the mass of an electron, and ϵ_0 is the permittivity of free space.

As was also seen in the Imp-6 radio instrument used by *Mosier et al.* [1973], in RPI dynamic spectrograms the intense UHR noise band typically extends from f_{uh} down to f_{pe} with a generally less intense emission extending down to the z-mode cutoff frequency given by

$$f_z = \frac{1}{2} \left[-f_{ce} + \left(f_{ce}^2 + 4f_{pe}^2 \right)^{1/2} \right] \quad (3.4)$$

The upper limit of the noise band at f_{uh} is usually the most pronounced cutoff in the RPI data. Thus, in order to determine the electron density profile for a given spectrogram, the f_{uh} is visually identified and the electron number density is

determined using Equation (3.1) and the cyclotron frequency inferred from the model magnetic field. In order to verify the correct identification of f_{uh} , both the f_{pe} and f_z are calculated and overlayed on the spectrogram. Figure 3.3a shows an example of the procedure used for density extraction with the frequencies of interest identified. Figure 3.3b shows the calculated electron density using the selected f_{uh} and the model f_{ce} . The red error bars show the range of density values corresponding to a $\pm 20\%$ variation in the magnetic field values (i.e., f_{ce}).

Errors in the magnetic field model cause significant changes in the derived density only when the plasma and cyclotron frequencies are of the same order of magnitude. Such errors are minimized in the outer plasmasphere where electron densities are high but the magnetic field strength is relatively low.

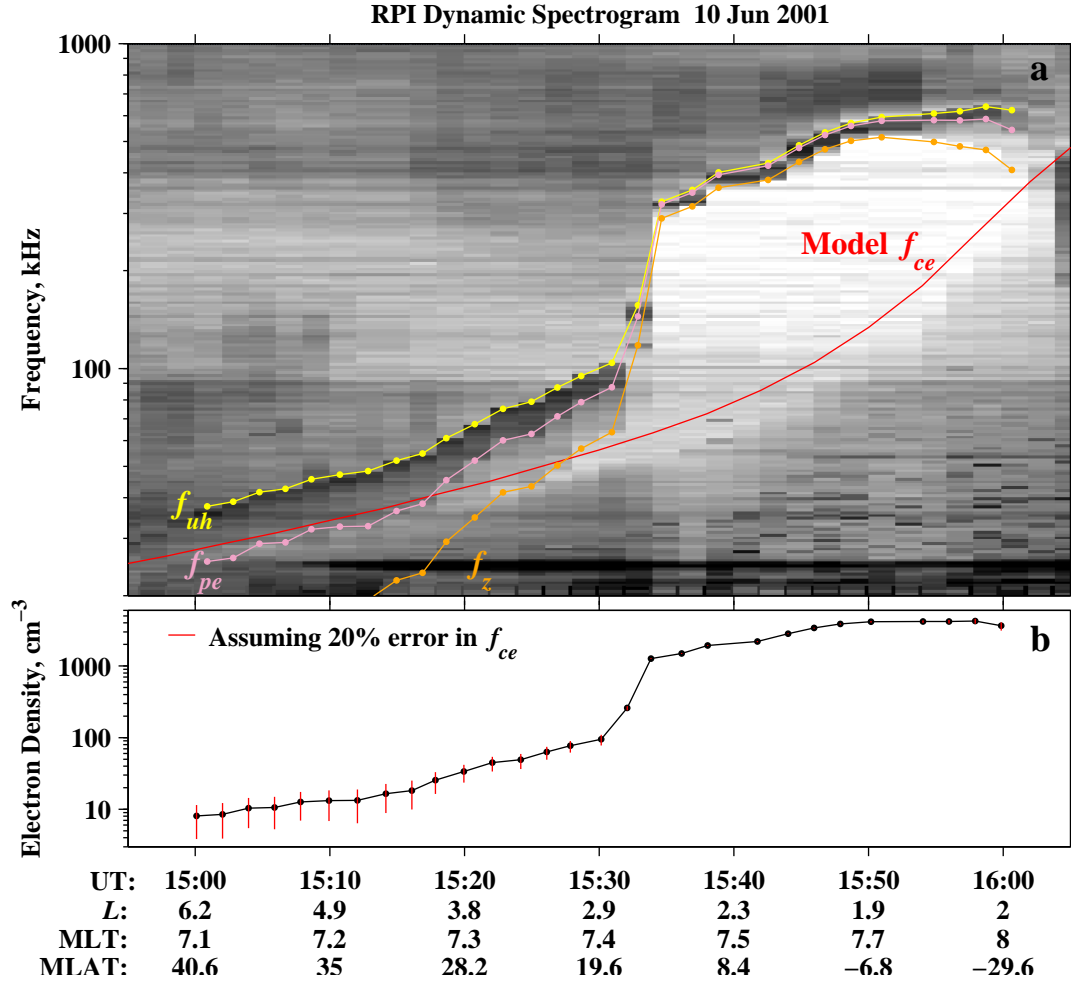


Figure 3.3. (a) RPI dynamic spectrogram with the upper hybrid frequency, f_{uh} , identified and the plasma, f_{pe} , and z-mode cutoff, f_z , frequencies overlaid using the model cyclotron frequency. (b) The derived electron density with the red error bar corresponding to $\pm 20\%$ error in the magnetic field model.

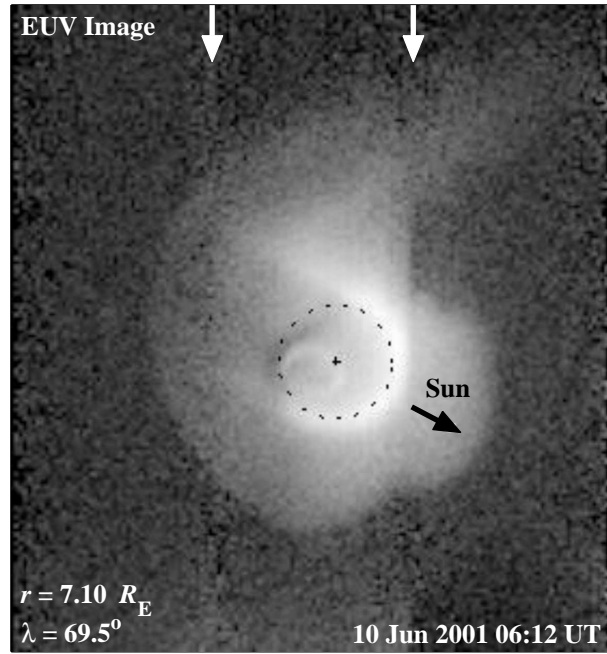


Figure 3.4. An EUV image of the plasmasphere taken on June 10, 2001 at 06:12 UT as IMAGE satellite approached apogee. The Earth is indicated by the dashed circle and the Sun direction by the black arrow.

3.3 Extreme Ultraviolet Imager

The EUV instrument [Sandel *et al.*, 2000] images the He^+ distribution in the Earth's plasmasphere by detecting resonantly scattered solar 30.4-nm radiation. He^+ is the second most abundant ion species in the plasmasphere, after H^+ which has no optical emission, and constitutes between 3 % and 30 % of the total ion distribution [Craven *et al.*, 1997]. Since the plasmaspheric He^+ emission is optically thin, the integrated column density of He^+ along the line of sight through the plasmasphere is directly proportional to the intensity of the emission.

EUV consists of three identical sensor heads, each having a 30° conical field of view. The sensor heads are tilted relative to one another by 27° to cover a fan-shaped instantaneous field of view of $84^\circ \times 30^\circ$. As the satellite spins, the instrument sweeps an $84^\circ \times 360^\circ$ swath across the sky. The sensitivity of the instrument is ~ 1 count per second per Rayleigh. EUV integrates the intensity of 30.4-nm emissions over 5

spins of the IMAGE satellite. Overlapping fields of view from 3 camera heads are then merged to form one complete image every 10 minutes. EUV collects images for $\sim 7 - 9$ hours out of each 14-hour orbit, generally operating where $L_{\text{dipole}} \geq 14$. The spatial resolution of EUV is $\sim 0.1 R_E$ in the equatorial plane as seen from apogee ($\sim 8 R_E$).

Figure 3.4 shows an EUV image from 06:12 UT on June 10, 2001 when the satellite was at a geocentric distance of $7.10 R_E$ and 69.5° magnetic latitude (location of the triangle in Figure 3.1). The universal time indicated for each EUV image refers to the center of the 10-minute integration window. The size and location of the Earth are indicated by the dashed circle, and the Sun direction is indicated by a black arrow. The shadow of the Earth is faintly visible in the anti-sunward direction due to the lack of solar illumination on the nightside of the Earth. Imperfect flat-fielding in the 3 camera heads appears as two vertical dark narrow bands across the image, indicated by the 2 white arrows. The haze around the Earth is the He^+ distribution in the plasmasphere. The dayside limb of the Earth exhibits a bright arc that contains the 30.4-nm He^+ emission as well as some leakage of neutral He airglow at 58.4-nm into the instrument passband.

Figure 3.4 was taken in the aftermath of a geomagnetic disturbance during which Kp reached a maximum value of 5+. The azimuthal structure of the plasmasphere is generally typical of that observed during disturbed periods, and the dynamic development of the features seen in Figure 3.4 is examined in Chapter 4.

3.3.1 Mapping EUV Images to the Equatorial Plane

As the spacecraft moves along the orbit from point EUV A to EUV B in Figure 3.1, the distance to the plasmasphere as well as the viewing angle continuously change. In view of such variations, the first step in the analysis of EUV data is to eliminate (or attempt to minimize) the distortion in the images due to the changing perspective by mapping the images to the magnetic equatorial plane. Throughout this section, we assume that the He^+ distribution as seen by EUV can be used as a proxy for the entire plasmasphere, and that the “sharp” intensity gradient in the He^+ distribution

can be reliably associated with the plasmopause boundary. This assumption is further investigated in Section 3.4.

Mapping the Plasmopause to the Equatorial Plane

Figure 3.5a shows a model He^+ distribution in the dawn meridional plane shown with a logarithmic color scale. An equatorial electron density distribution was taken from the Global Core Plasma Model (GCPM) [Gallagher *et al.*, 2000] for MLT = 06 and $Kp = 3-$, and He^+ was assumed to uniformly comprise 10% of the total ion distribution. The equatorial He^+ density profile used is shown in Figure 3.5b. A diffusive equilibrium model was used for the distribution of He^+ along the geomagnetic field lines. The expression for the density along the magnetic field line normalized to the equatorial density was taken from Park [1972], and a plasma temperature of 1 eV was assumed.

The red and green lines in Figure 3.5a represent two different possible lines of sight from the vantage point of the EUV instrument through the He^+ distribution. Both lines of sight are tangent to the plasmopause boundary ($L = 4.53$) but at different geomagnetic latitudes (red: $\lambda = 0^\circ$, green: $\lambda = 20^\circ$). Figure 3.5c shows the model He^+ distribution along each line of sight. The distribution is plotted as a function of distance, in L , away from the minimum L ($L_{\min} = 4.53$ for both lines). There is a rather sharp peak in the distribution due to the contribution from L values very near the minimum L . The -3 dB full width of both peaks is $\sim 0.04 L$. Therefore, the contribution to the line of sight column density is primarily due to the contribution from the minimum L value when the line of sight is tangent to the plasmopause, regardless of the viewing angle. There is very little contribution to the line of sight column density from $L > L_{\min}$.

In order to use these types of considerations to eliminate the effects of the changing perspective, two additional assumptions must be made: (1) the plasmopause is a field aligned surface, and (2) a tilted dipole magnetic field model can be reliably used throughout the field of view of the EUV instrument. The second assumption is the more tenuous of the two especially in regions where L is greater than approximately 5 and during periods of moderate to strong geomagnetic activity. However, the dipole

assumption greatly reduces the complexity of the mapping routines that need to be used.

Using software routines provided by the EUV instrument team, the plasmopause boundary as observed in the global EUV images is mapped to the magnetic equatorial plane as follows. The points corresponding to the plasmopause boundary are manually selected along the sharp brightness gradient on each image. Figure 3.6a shows the plasmopause locations selected manually for the image of Figure 3.4. Next, the minimum L along the line of sight is found for each selected point, and the field line is traced to the magnetic equator (XY_{SM} plane) using a centered, tilted dipole model. Figure 3.6b shows the mapping of the selected points plotted as function of L versus magnetic local time (MLT). Concentric dotted circles are spaced $1 R_E$ apart, and $L = 4$ is indicated by the dashed circle. MLT spokes are drawn every 2 hours with noon being in the $+X_{\text{SM}}$ direction. The uncertainty associated with this mapping method is discussed in Section 3.4.

A plasmopause location is selected only at local times for which a sharp brightness gradient can be identified. In some cases, the plasmopause boundary may lie outside the field of view or the brightness may fall off gradually with distance so that no sharp gradient can be reliably identified. In this context, it is important to note that *Goldstein et al.* [2003a] and *Moldwin et al.* [2003] have estimated the lower sensitivity of the EUV cameras to be equivalent to $30 - 50$ electrons cm^{-3} . Accordingly, those transitions that represent a “sharp” density change, from typical plasmaspheric densities of several hundreds of electrons per cm^{-3} to several tens of electrons per cm^{-3} within about a half an R_E , are best suited for this type of visual identification.

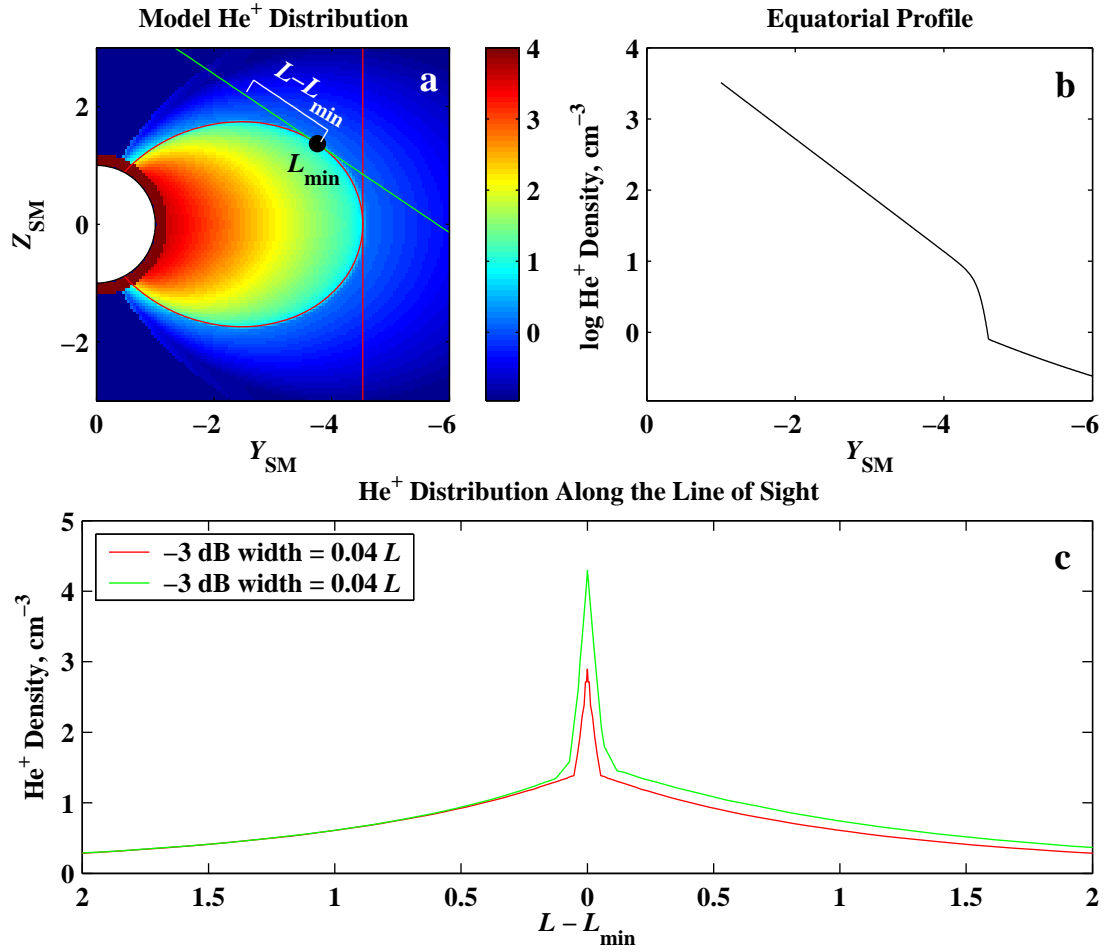


Figure 3.5. (a) The model He⁺ distribution in the dawn meridional plane constructed using an equatorial profile shown in (b) and assuming a diffusive equilibrium distribution along the field lines. Two line of sights (red and green) pass through a minimum L (L_{min}) of 4.53. (c) The He⁺ distribution along the two line of sights, red and green lines in (a), showing that the maximum contribution to the column density comes from field lines within $0.05 L$ of L_{min} .

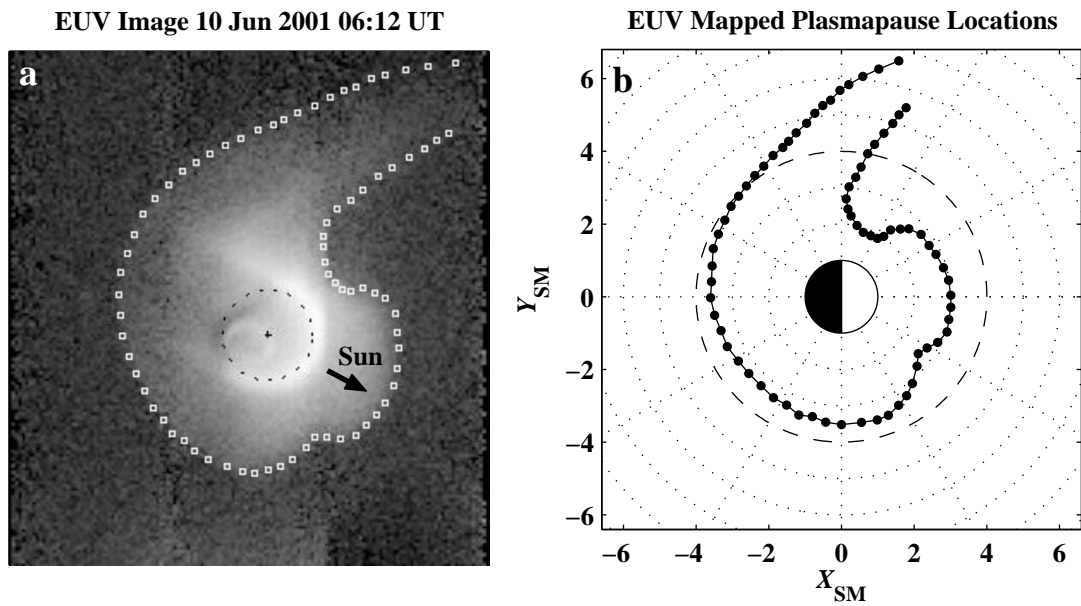


Figure 3.6. (a) An EUV image from June 10, 2001 at 06:12 UT, with the plasmopause locations indicated by the white squares. (b) The equatorial mapping of the plasmopause locations from (a) using the minimum L technique.

Mapping the Entire He^+ Distribution to the Equatorial Plane

The technique described in the previous section can also be used to map points interior to the plasmopause to the geomagnetic equatorial plane although the uncertainty associated with such a mapping is higher than that for the mapping of just the boundary points. This increased uncertainty can be seen in Figure 3.7 in which the same meridional density distribution as in Figure 3.5 has been used, but with the two lines of sight being tangent to a field line ($L=3.53$) interior to the plasmopause. There still are peaks in the He^+ density along the line of sight (Figure 3.7c) corresponding to the minimum L value, but there now are also significant contributions from $L > L_{\min}$. The -3 dB width of the peaks is greater than a third of an L , but once again we see that the line of sight distribution is not strongly dependent on the viewing angle.

Figure 3.8 shows the EUV image of June 10, 2001 at 06:12 UT with each pixel mapped to the magnetic equatorial plane using the minimum L technique. The format is similar to that of Figure 3.6b with being noon to the right and white dashed circle corresponding to $L=4$. The image has also been calibrated so that the color scale is the log of the He^+ column density, in cm^{-2} , along the line of sight of each pixel. The calibration is a function of the instrument response as well as the input solar 30.4-nm flux which varies daily and is obtained from the SOLAR2000 empirical solar irradiance model [Tobiska *et al.*, 2000].

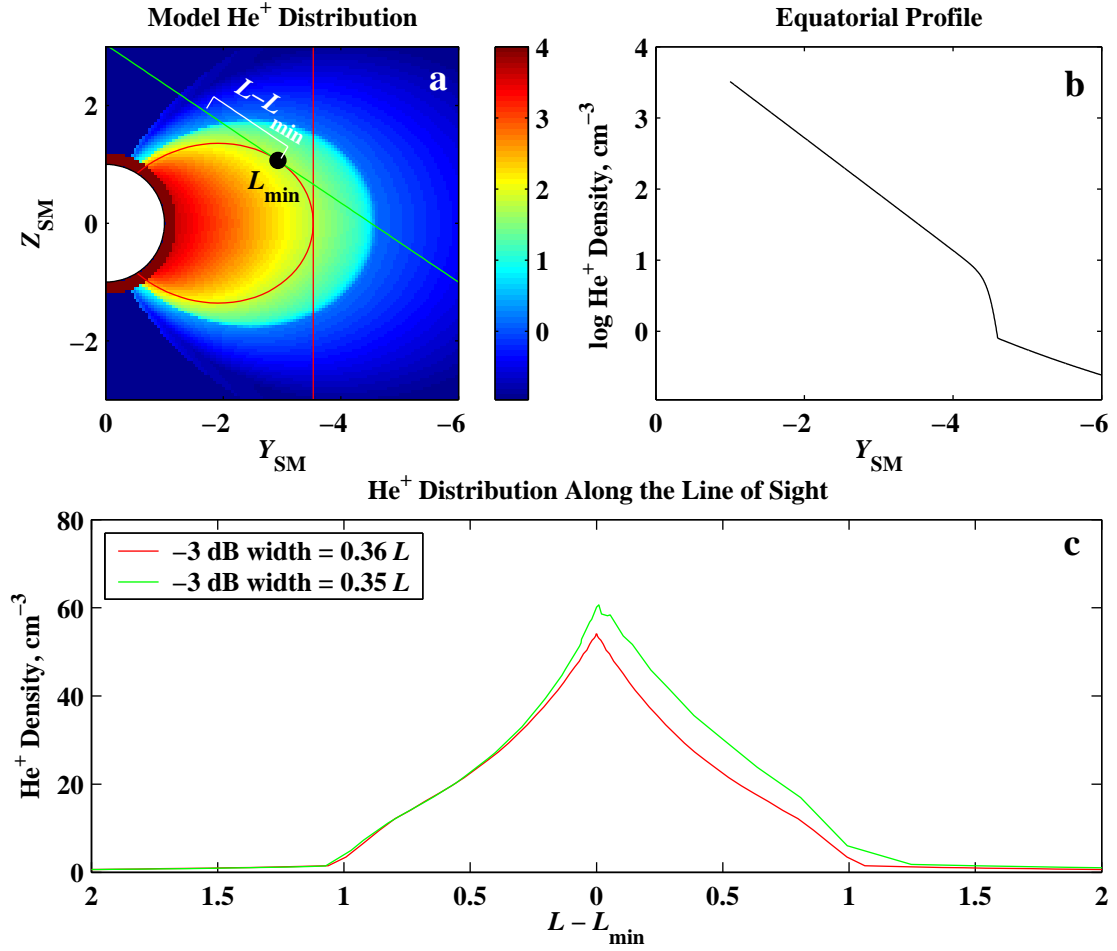


Figure 3.7. The format is the same as that of Figure 3.5, but in this case the lines of sight are tangent to a field line interior to the plasmopause ($L_{min} = 3.53$) and thus there is more contribution to the column density from L values greater than L_{min} .

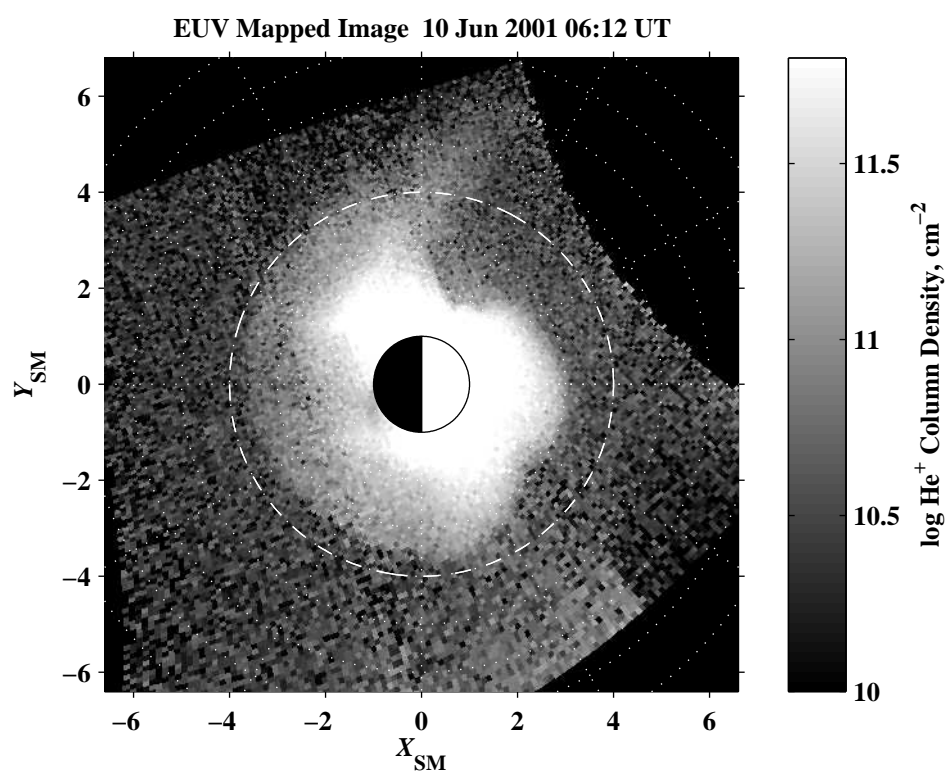


Figure 3.8. The EUV image from Figure 3.4 with each pixel mapped to the magnetic equatorial plane using the minimum L technique.

3.4 The He^+ Edge and the Plasmapause

Since the ratio of the He^+ density to the total number density within the plasmasphere is known to vary both spatially and temporally [e.g., *Craven et al.*, 1997], it is necessary to investigate the degree to which the He^+ distribution as seen by the EUV instrument can be used a proxy for the entire plasmasphere. In the EUV images the plasmapause is assumed to be the outermost sharp edge where the intensity of the 30.4-nm radiation drops “abruptly”, henceforth called the “ He^+ edge”. A quantitative test of this assumption is made possible by comparing the location of the steep electron density gradient at the plasmapause observed *in situ* by RPI to the location of the He^+ edge observed by EUV when the satellite is near apogee. The results of this study were originally published as *Goldstein et al.* [2003a].

3.4.1 Methodology

A statistical analysis was performed for all inbound (dawn local sector) plasmapause crossing for the month of June 2001 using the following methodology:

1. For each dawnside plasmapause crossing, a steep gradient was visually identified in the RPI dynamic spectrogram. A line segment of n_e versus L was recorded for each gradient.
2. Two EUV images were selected, one before and one after the RPI-observed plasmapause crossing. The time difference between the RPI measurement and each of the EUV images was minimized.
3. From each image the He^+ edge was extracted at approximately the same magnetic longitude as the RPI gradient (typically within $1^\circ - 2^\circ$), implicitly assuming that the plasmasphere strictly corotated in the intervening time between the measurements.
4. The L values of the RPI gradients and the EUV He^+ edges were compared. When possible, the EUV L value was calculated as an average of two EUV images that bracketed the RPI measurement in time. This averaging was found

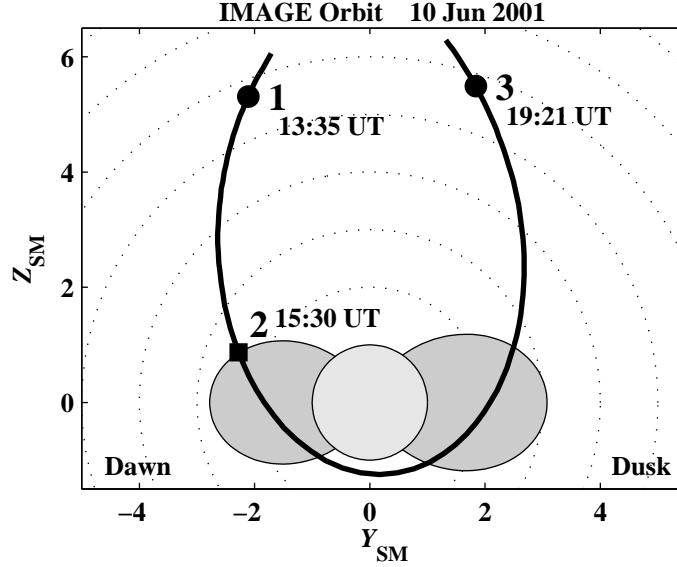


Figure 3.9. IMAGE orbit from June 10, 2001 showing the location of the RPI measurement of the dawn side plasmopause crossing (“2”) and the two EUV images closest in time to that crossing (“1” and “3”).

necessary to minimize the effects of inward or outward drifts of plasmaspheric flux tubes or expansion of the plasmasphere due to refilling in the intervening time.

The procedure 1 to 4 was attempted for the dawnside plasmopause crossings in each of the 51 orbits of the IMAGE satellite during June 2001. Duskside plasmopause crossings were not included in this study. Two of the 51 orbits had RPI line segments for which both of the endpoints were below 50 cm^{-3} and were excluded on the grounds that such low densities were near or below the lower sensitivity threshold of EUV. Two of the orbits had no available/interpretable EUV images. Out of the remaining 47 orbits, 15 orbits had only one EUV image (either before or after the RPI measurement) that permitted reliable extraction of the He^+ edge. Thus, 47 orbits were analyzed using this methodology: 32 used two EUV measurements per RPI dynamic spectrogram, and 15 used only one EUV measurement per RPI dynamic spectrogram. The maximum time difference between the RPI and EUV measurements was 10.8 hours, and the average time difference was 4.6 hours.

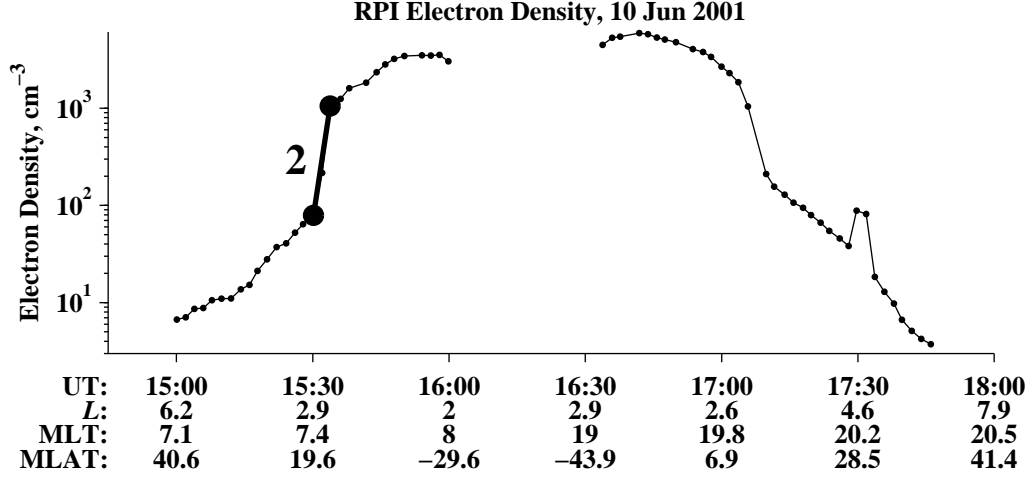


Figure 3.10. Density profile extracted from the RPI dynamic spectrogram on June 10, 2001. The dawnside plasmopause gradient is identified as the bold line segment labeled “2”.

3.4.2 Example Cases

We use the orbit from June 10, 2001 (Figure 3.9) as an example to illustrate the details of the methodology outlined above. Figure 3.10 shows the electron density profile extracted from RPI data (as described in Section 3.2.1) obtained from 15:00 to 18:00 UT on this day. IMAGE crossed the dawnside plasmopause at 15:30 UT (location labeled “2” in Figure 3.9). The steep gradient in electron density is shown by a single line segment over-plotted on the density profile as a bold line. The two endpoints of this line segment (indicated as filled circles) both occur at 7.4 MLT. The outer (inner) endpoint has an L value of 2.9 (2.6).

EUV images for this orbit were produced during two intervals, 04:21 – 13:35 UT and 19:21 – 23:57 UT. The two EUV images closest in time to the 15:30 UT plasmopause crossing are therefore from 13:35 UT (~ 2 hours before) and 19:21 UT (~ 4 hours after). In Figure 3.9, these locations are labeled as “1” and “3” respectively. The extracted He^+ edges from these two times are shown in Figure 3.11. The location of the RPI observed plasmopause gradient is shown both at the MLT of the original measurement (open circles) and at the MLT assuming strict corotation of the plasmasphere, i.e., rotated -1.91 hours of MLT in panel “1” and rotated $+3.85$ hours of

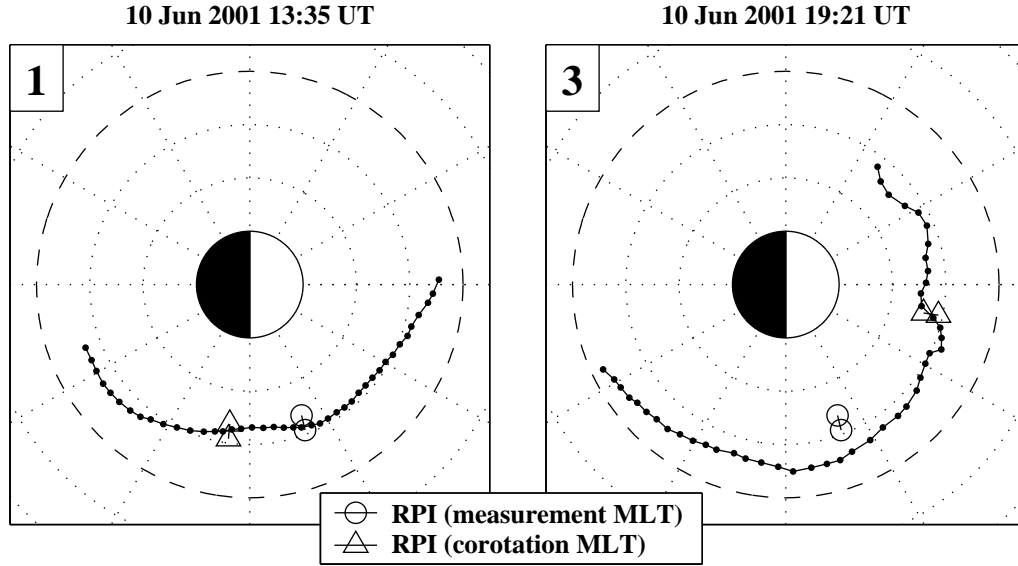


Figure 3.11. The extracted He⁺ edges from the two EUV measurements which bracket in the time the RPI plasmopause crossing. The original MLT and L of the RPI gradient are shown as a pair of open circles, and the MLT assuming corotation of the plasmasphere is shown as a pair of open triangles.

MLT in panel “3”.

In this example, when the plasmopause is assumed to corotate in the intervening time between measurements, there is excellent agreement between the RPI measurement of the plasmopause density gradient and the location of the He⁺ edge as measured by EUV both before and after the RPI measurement. This same information is displayed in a slightly different way in Figure 3.12. The RPI gradient is shown as a line segment of electron density versus L and the L location of the He⁺ edges are shown as vertical lines. This example suggests that the He⁺ edge is indeed a visual signature of a steep density gradient at the plasmopause.

As can be seen in Figure 3.12, any azimuthal variation in the plasmopause radius can effect the comparison between the *in situ* measurement of the density gradient and the He⁺ edges, especially if the assumption of strict corotation is violated. While corotation is a reasonable assumption on the dawnside, it may be a very poor assumption in the dusk sector [Carpenter and Park, 1973]. In addition, shallow

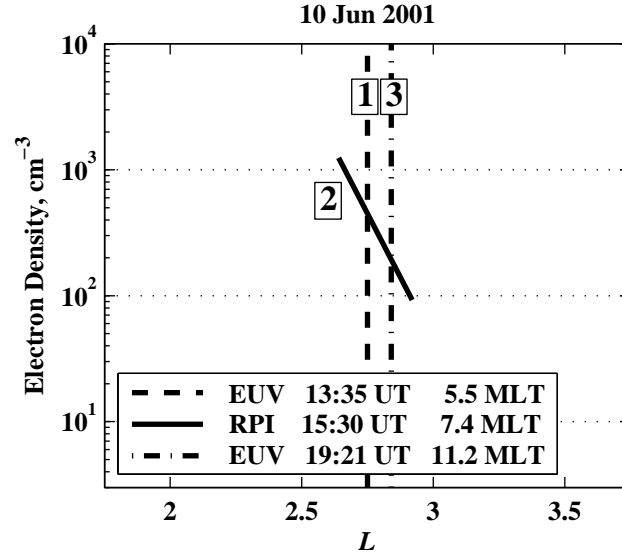


Figure 3.12. RPI measurement of the plasmopause gradient overlayed with the L location of the He^+ edges as observed by EUV on June 10, 2001.

density gradients with no clear plasmopause appeared more frequently in the RPI duskside plasmopause crossings. Thus, duskside plasmopause comparisons were not included in our statistical study.

In addition to spatial variations, temporal changes in the plasmopause location due to varying geomagnetic activity would tend to decorrelate the RPI and EUV measurements. In general, during active conditions the plasmopause can be expected to move inward on the dawn sector (on times scales as fast as an hour or two) while during recovery periods, we expect the boundary to drift outward and the plasmasphere to slowly refill (over the course of one to several days). Thus, it is useful to consider the geomagnetic conditions when comparing temporally separated plasmopause measurements.

The values of the Kp index for June 10, 2001 (Figure 3.13) indicate that all three measurements (i.e., “1”, “2” and “3” as shown in Figure 3.9) were made in the aftermath of a geomagnetic disturbance which occurred early in the day, and hence the plasmopause was observed to be at $L < 3$ in all three measurements. However, Kp was fairly steady in the intervening time between the three measurements, and

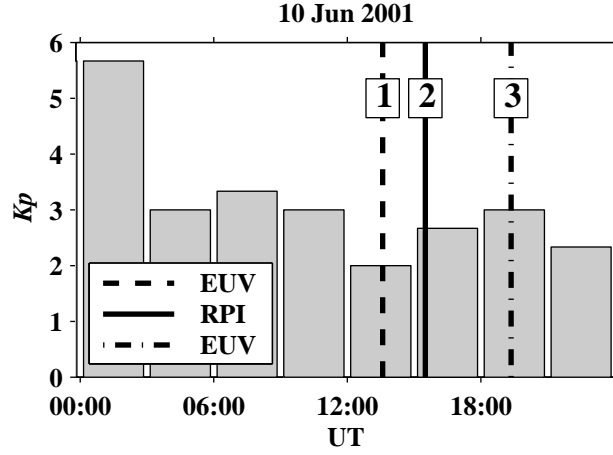


Figure 3.13. The Kp index for June 10, 2001 with the times of the RPI and EUV measurements identified.

thus good agreement between the measurements can be expected.

In contrast to the case of good agreement between the two EUV images and the RPI *in situ* measurements, Figure 3.14 illustrates a case on June 2, 2001 when the plasmopause was observed to move progressively inward between the three measurements. The Kp index from this time (Figure 3.15) indicates relatively strong activity, consistent with inward motion of the plasmopause.

The third example (Figure 3.16), illustrates a case of outward motion of the boundary during a period of relatively low geomagnetic activity (Figure 3.17). In this case the outward motion is attributed to outward drifting flux tubes and/or refilling of flux tubes during this period of recovery.

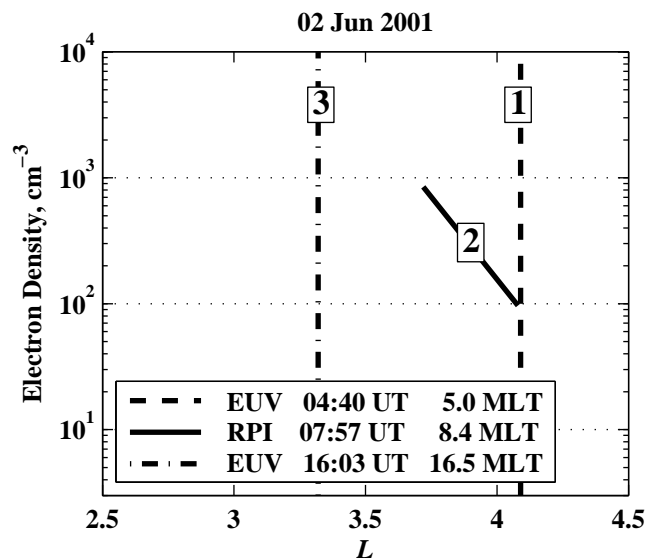


Figure 3.14. RPI and EUV measurements from June 2, 2001 showing an inward progression of the plasmapause.

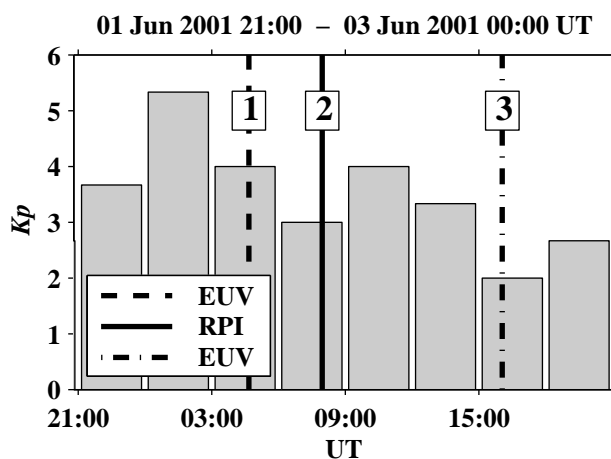


Figure 3.15. The Kp index for the observed inward motion of the plasmapause on June 2, 2001.

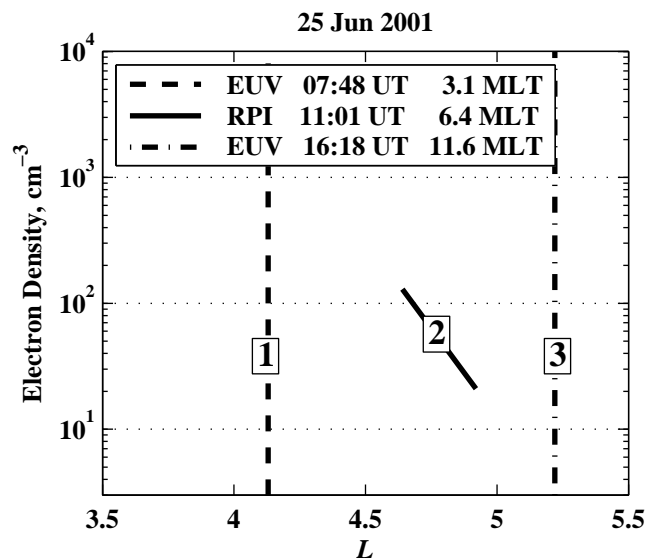


Figure 3.16. RPI and EUV measurements from June 25, 2001 showing an outward progression of the plasmapause.

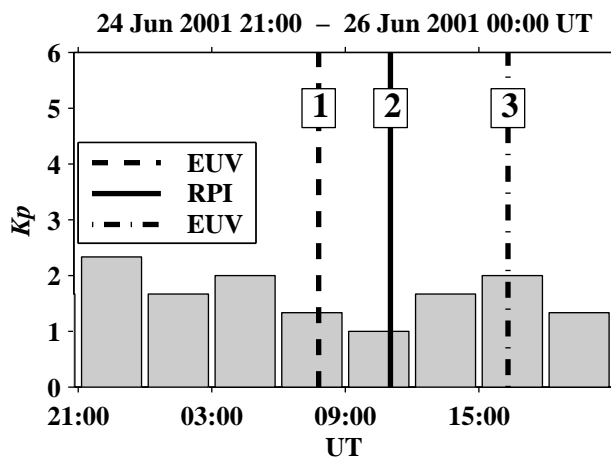


Figure 3.17. The Kp index on June 25, 2001 indicates relatively quiet geomagnetic conditions.

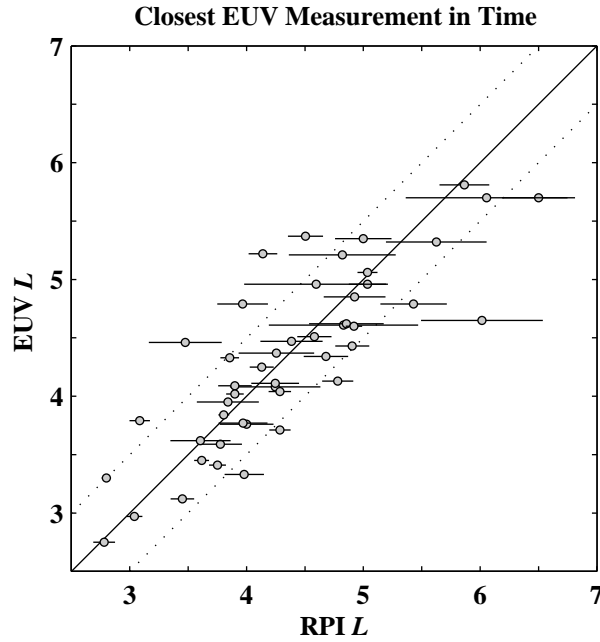


Figure 3.18. Correlation between the closest-in-time EUV measurement of the He^+ edge and the RPI midpoint L value of the density gradient. The length of the horizontal bar on each data point is inversely proportional to the steepness of the density gradient.

3.4.3 Statistical Analysis

The two cases of temporal variation of the plasmopause position illustrated in Figures 3.14 and 3.16 are not atypical. Of the 32 orbits in which there were two EUV measurements available (with an average time difference of ~ 9 hours), approximately two-thirds showed plasmopause displacements of $0.5 L$ or more.

One way to minimize the effects of the temporal separation of the measurements is to compare the EUV measurement that occurred closest in time to the RPI plasmopause crossing. Except in the case where EUV data gaps occurred, the closest EUV measurement was typically taken a few hours before the RPI measurement. The results of this comparison are shown in Figure 3.18 where the RPI L is defined as the L value at the midpoint of each RPI density gradient line segment. The length of the

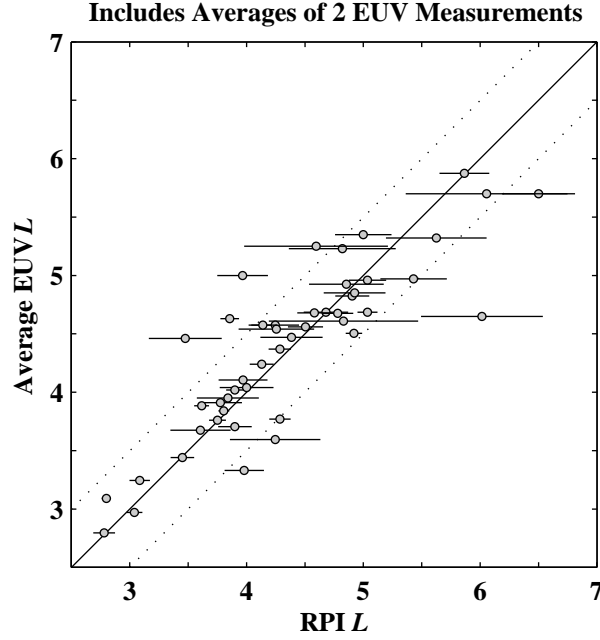


Figure 3.19. Correlation between the average EUV L (includes orbits with both one and two EUV measurements available) and the RPI L .

horizontal bar on each data point is

$$\left[\frac{\Delta(\log n_e)}{\Delta L} \right]^{-1}$$

representing the uncertainty in the assessment of the plasmopause position which is inversely proportional to the steepness of the RPI density gradient. The solid diagonal line indicates perfect agreement between the two measurements, and 36 out of the 47 data points (77%) are within $0.5 L$ of perfect agreement (the dotted diagonal lines). There appears to be slightly less scatter in the steeper gradients (short horizontal lines). The correlation between the closest (in time) EUV measurement ($L_{\text{EUV,closest}}$) and the RPI measurement (L_{RPI}) is 0.83 (highly significant).

A second way to minimize the effects of erosion or recovery in the intervening time between the measurements is to take advantage of the fact that 32 orbits had two EUV measurements available, one before and one after the RPI measurement. Thus, an average of the two EUV measurements ($L_{\text{EUV,avg}}$) was constructed to compare

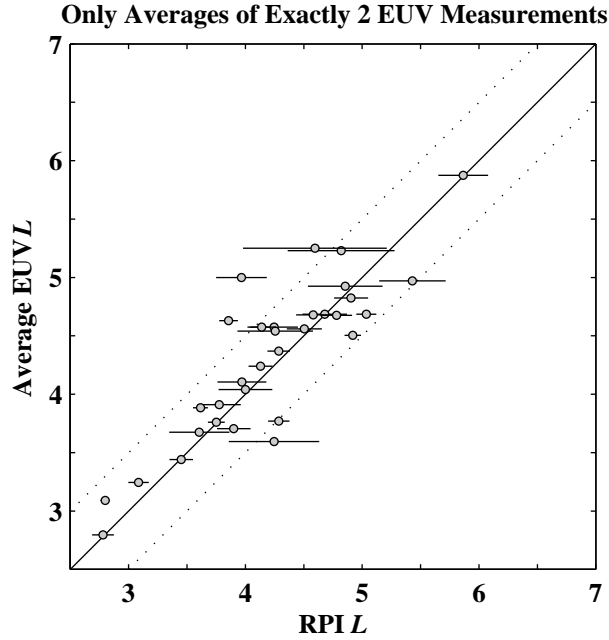


Figure 3.20. Correlation between the average EUV L (includes only those orbits with exactly two EUV measurements available) and the RPI L .

with the RPI measurement. In the example event of June 25, 2001 (Figure 3.16), the average of the two EUV measurements is several tenths of an L closer to the RPI measurement than either EUV measurement alone. For the June 2, 2001 case, the closest in time measurement and the average measurement are equidistant from the RPI measurement so that the averaging does not change the comparison. Figure 3.19 shows the correlation between $L_{\text{EUV,avg}}$ and L_{RPI} . This plot contains all 47 orbits and thus includes orbits for which only one EUV measurement was available. When the average EUV measurement is compared to the RPI measurement 55 % of the points are within $0.25 L$ of perfect agreement and 81 % are within $0.5 L$. The correlation coefficient is 0.86 (highly significant). The tendency of steeper gradients to be less scattered from the center line is more pronounced.

Figure 3.20 also presents a plot of $L_{\text{EUV,avg}}$ versus L_{RPI} , but in this case includes only the 32 orbits for which there were exactly two EUV measurements available for averaging. The correlation coefficient in this case is 0.87 (highly significant).

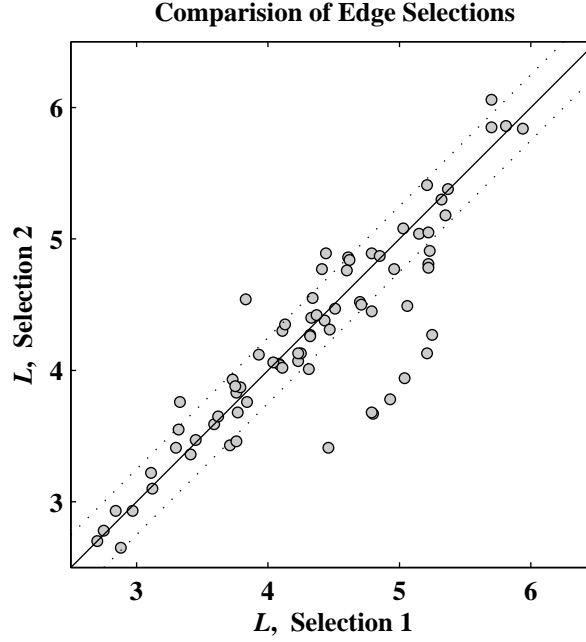


Figure 3.21. Comparison of the two independent EUV He⁺ edge extractions. The solid diagonal lines indicates perfect agreement and the dotted lines are $\pm 0.25 L$.

One source of error in this study is the intrinsic subjectivity involved in the manual extraction of the He⁺ edges from the raw EUV images. As an attempt to quantify this uncertainty, two versions of this study were performed independently. Two individuals separately performed the extraction of all the EUV edges corresponding to the RPI gradients for each of the orbits in June 2001. The difference between the two measurements was judged to be the uncertainty due to subjectivity in the EUV edge extraction. Figure 3.21 shows a comparison of the two independent extractions. The difference was less than $0.25 R_E$ for 73 % of the images. The images for which there was greater than $0.25 R_E$ difference tended to correspond to a gradual roll-off in the intensity of the image rather than a sharp, well-defined He⁺ edge.

3.4.4 Conclusions

In examining a month of RPI and EUV data, we have found an excellent correlation between steep electron density gradients measured *in situ* by RPI and He⁺ edges

observed in the EUV images. Maximum correlation between the data sets is found when the RPI measured plasmopause location is compared to an average of two EUV measurements which bracket (in time) the RPI measurements. The averaging appears to reduce the effects of erosion or recovery in the intervening hours between the measurements and a correlation coefficient of 0.87 is obtained. Based on our results, we conclude that a well-defined He^+ edge may be reliably interpreted as the plasmopause.

Chapter 4

The Global Response of the Plasmasphere to a Geomagnetic Disturbance

In this chapter, we use global images of the plasmasphere obtained by the Extreme Ultraviolet (EUV) imager on the IMAGE satellite to study the evolving structure of the plasmasphere during two geomagnetic disturbances. By tracking the location of the plasmapause as a function of L shell and magnetic local time, quantitative measurements of radial and azimuthal motions of the boundary are made for intervals ≥ 7 hours in duration with a time resolution of 10 minutes. The two cases presented are June 26 – 27, 2001, a period of relatively weak but isolated geomagnetic disturbance, and June 9 – 10, 2001, a period moderate disturbance activity with a multi-staged onset and recurring substorm activity after the main disturbance.

In support of the global images, *in situ* density measurements available from several instruments were used. The density of ions in the range of $\sim 1 - 130$ eV/ q are provided by the Los Alamos magnetospheric plasma analyzers (MPA) [*Bame et al.*, 1993; *McComas et al.*, 1993] onboard two geosynchronous satellites ($L = 6.6$) 1991–080 and 1994–084. Electron density profiles are also obtained from passive mode dynamic spectrograms recorded by the IMAGE Radio Plasma Imager (RPI) when the satellite is at low magnetic latitudes.

The results of this study were originally published as *Spasojević et al.* [2003].

4.1 Case I: June 26 – 27, 2001

On the 26th through 27th of June, 2001, the magnetosphere experienced a mild geomagnetic disturbance, and the response of the plasmasphere was observed globally by IMAGE EUV and *in situ* by the LANL MPA instruments and IMAGE RPI. Although a relatively weak substorm-related disturbance with Kp reaching a maximum value of 4, this is a particularly interesting study period because of the isolated nature of the event. For over 40 hours prior to the onset of the disturbance, Kp remained ≤ 2 , and immediately after the disturbance Kp dropped to ≤ 1 — for over 30 hours. The geomagnetic and solar wind conditions for a 30 hour period from 04:00 UT on the 26th through 20:00 UT on the 27th of June 2001 are shown in Figure 4.1. From top to bottom, the panels indicate Kp , $SYM-H$ which is essentially a 1-minute version of the Dst index, AE , polar cap potential (PCP) derived from measurements from the SuperDARN radar network [*Shepherd and Ruohoniemi, 2000*], and solar wind B_z from ACE MAG [*Smith et al., 1998*] time shifted by 54.8 minutes to correspond to the average propagation time to the magnetopause for this interval. The solar wind dynamic pressure (not shown) for this interval as observed by ACE SWEPAM [*McComas et al., 1998*] stayed relatively constant at values ≤ 3.7 nPa. During this time period, there are three intervals for which global EUV images of the plasmasphere are available (indicated by the matching sets of vertical lines): June 26, 05:56 – 14:27 UT; June 26, 18:53 – June 27, 03:55 UT; and June 27, 10:22 – 18:23 UT.

4.1.1 Quiet Geomagnetic Conditions

The series of EUV global images from 05:56 to 14:27 UT on June 26, 2001, between the dashed lines in Figure 4.1, captured the onset of the geomagnetic disturbance on June 26, 2001. Figure 4.2a shows the EUV extracted plasmopause location at 08:59 UT on June 26 before the disturbance onset plotted in the equatorial plane as a function of L (or R) versus magnetic local time (MLT). The view is from the north

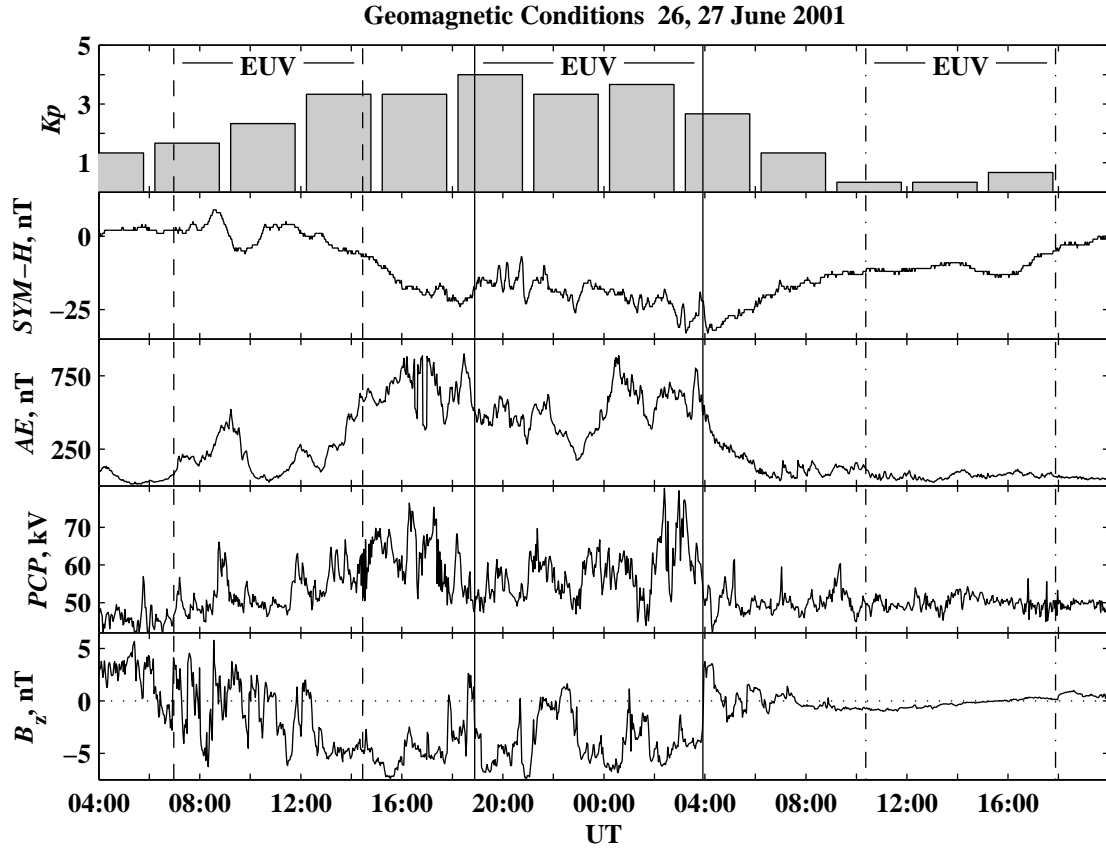


Figure 4.1. Geomagnetic and solar wind conditions for a 40 hour period from 04:00 UT on June 26, 2001 to 20:00 UT on June 27, 2001. From top to bottom, the panels indicate K_p , $SYM-H$, AE , polar cap potential (PCP), and solar wind B_z (in GSM coordinates) from ACE MAG time shifted by 54.8 minutes. Intervals between sets of matching vertical lines indicate time periods for which EUV global images of the plasmasphere are available.

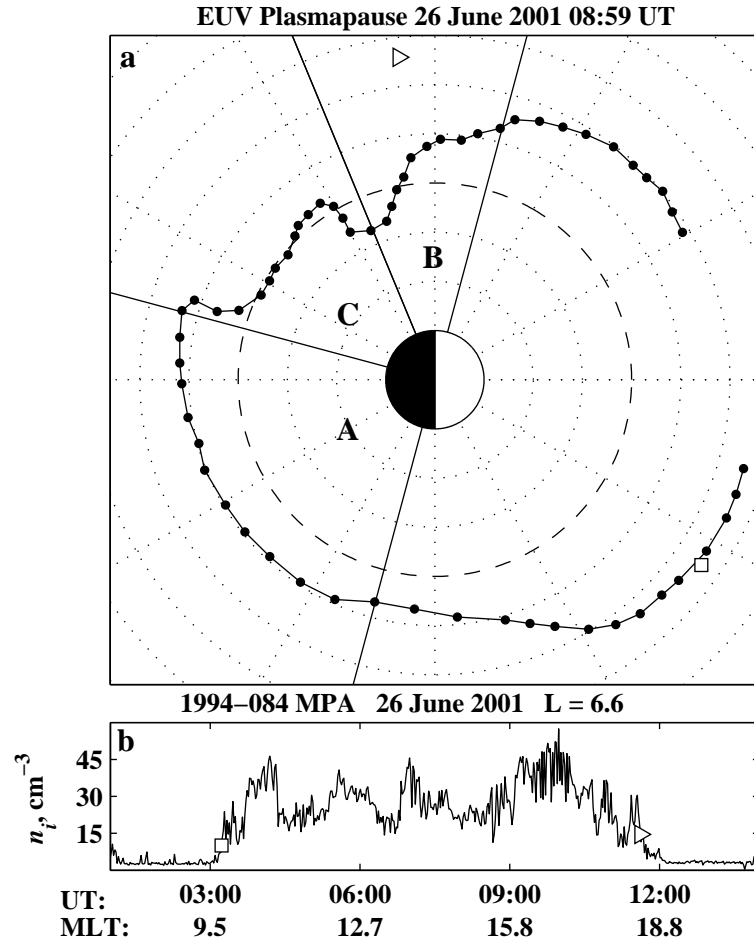


Figure 4.2. (a) The EUV extracted plasmopause location at 08:59 on June 26, 2001 before the onset of a weak geomagnetic disturbance. The view is from the north pole and the sun is to the right. Concentric dotted circles are spaced $1 R_E$ apart, $L = 4$ is indicated by the dashed circle, and MLT spokes are drawn every 2 hours. (b) Ion number density observed along geosynchronous orbit indicating a dayside bulge of plasmaspheric plasma.

pole and the sun is to the right. Concentric dotted circles are spaced $1 R_E$ apart, and $L = 4$ is indicated by the dashed circle. MLT spokes are drawn every 2 hours. At this time the average plasmapause location was $L \simeq 5$ as may be expected under quiet conditions. However significant azimuthal variation in the plasmapause radius was observed with a minimum of $L = 3.3$ near 19.6 MLT and a maximum of greater than 6.6 on the dayside where between 10.9 and 14 MLT the boundary was outside the field of view of EUV.

The MPA instrument on LANL satellite 1994–084 also observed a bulge of plasmaspheric plasma along its geosynchronous orbit ($L = 6.6$) throughout most of the dayside (Figure 4.2b). The local time extent of this bulge is indicated as the local time between the open square and open right-facing triangle in Figure 4.2a.

EUV commonly observes variations in the plasmapause radius with local time on the order of $1 - 2 R_E$ during quiet periods that can persist for as long as 60 hours [Sandel *et al.*, 2003]. This observation is consistent with a statistical analysis by Moldwin *et al.* [1994] in which it was noted that, during low activity levels, a geosynchronous satellite can commonly encounter bulges of plasmaspheric plasma with a range of local time durations throughout the day and evening portions of its orbit.

4.1.2 Disturbance Onset

Erosion on the Nightside

Beginning after 11:20 UT EUV images captured an inward movement of the plasmapause in the midnight to dawn local time quadrant. The approximate local time sector is labeled **A** in Figure 4.2a although by 11:20 the sector had rotated such that the western edge was located near midnight. No inward movement of the boundary could be detected at any other local time, yet it should be noted that the plasmapause in the dusk to midnight quadrant was already at reduced L .

Figure 4.3a shows the progression of the boundary plotted as L shell versus magnetic local time. Each curve represents the extracted plasmapause location at the universal time specified in the legend. Near the end of the interval as the IMAGE

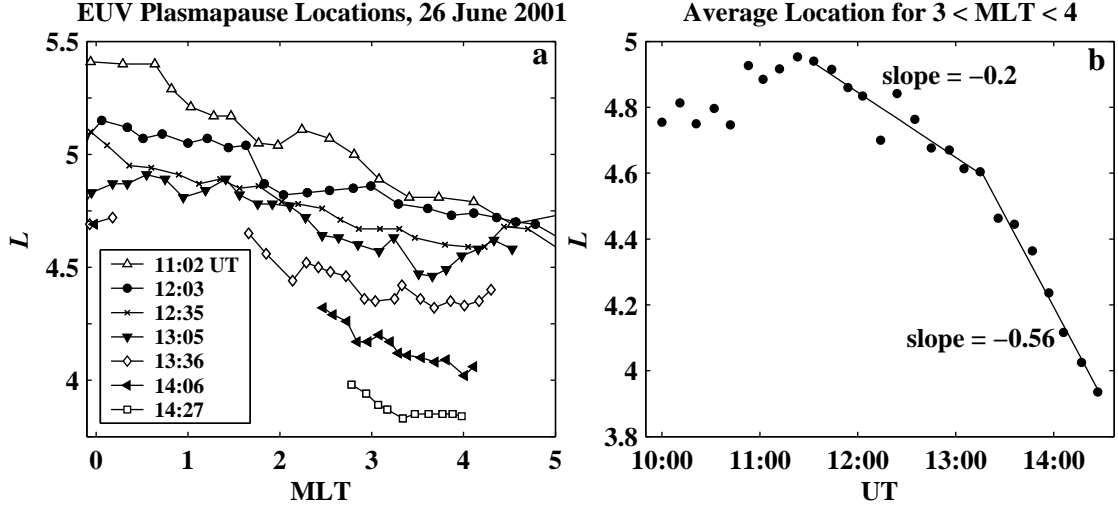


Figure 4.3. (a) Plasmopause locations in L for in the 00 – 05 MLT sector at selected universal times. (b) The average plasmopause location is tracked between 3 and 4 MLT in all EUV images between 10:00 and 14:30 UT.

satellite moved toward perigee, the plasmopause boundary began to move outside of the field of view of the EUV instrument. Hence after 13:05 UT, the plasmopause location was available in only a limited local time sector until the EUV cameras were turned off after the image at 14:27 UT. Figure 4.3b shows the average plasmopause location in the local time sector $3 \leq \text{MLT} \leq 4$ plotted as L versus UT. Plasmopause locations from all available EUV images from 10:00 UT to 14:30 UT are included. Beginning after $\sim 11:30$ UT, the plasmopause began moving inward in L at an average rate of $0.20 L$ per hour of UT, calculated in a linear least-squares sense. Subsequently from $\sim 13:15$ to 14:27 the average erosion rate increased to $0.56 L$ per hour of UT.

Both the initial onset of erosion and the increase in the rate were correlated with southward turnings of the IMF B_z . At 11:00 UT, a southward turning of the IMF which lasted about 45 minutes reached the magnetopause. After ~ 32 minutes the PCP began to rise, and the plasmopause began moving inward. Then at $\sim 12:30$ UT B_z turned and remained steadily southward for > 5 hours. This longer period of southward IMF is correlated with the increased average erosion rate. The instantaneous radial velocity of the plasmopause (dL/dt) in the post-midnight sector calculated

from each of the points in Figure 4.3b was correlated with high statistical significance with both the polar cap potential and the IMF B_z (time shifted by 32 minutes in addition to propagation delay from the ACE satellite to the magnetopause). This result is consistent with the recent report of *Goldstein et al.* [2003b] discussing the timing between the IMF B_z and another EUV observed plasmaspheric erosion event. The additional time delay for the IMF B_z is attributed to a combination of the delay due to propagation from the magnetopause to the ionosphere and the ionospheric reconfiguration time [*Goldstein et al.*, 2003b and references therein].

Smoothing of Azimuthal Features

While the EUV images captured inward motion in the post-midnight sector, flows in the pre-midnight sector led to a smoothing of the azimuthal features labeled sectors **B** and **C** in Figure 4.2a. For ~ 5 hours from 9 UT to 13 UT, the average rotation rate of the features in sector **B** was estimated to be $\sim 60\%$ of the corotation velocity, while sector **C** rotated at only $\sim 30\%$ of corotation. The differential rotation in the dusk to midnight quadrant led to distortion and essentially a smoothing of the azimuthal features seen in Figure 4.2a.

4.1.3 Disturbance Main Phase

After 14:27 UT, the EUV cameras were turned off for ~ 4.5 hours as the IMAGE satellite passed through perigee. The next available sequence of EUV images, identified as the time period between the solid vertical lines in Figure 4.1, captured the formation of a plasmaspheric plume in the noon to dusk quadrant. The interval began with Kp at its maximum value of 4 for the disturbance. The IMF B_z component was primarily southward during this interval but approached and remained near zero for several hours. The end of the EUV measurement interval at 03:55 UT on June 27 coincided with an abrupt northward turning of the IMF and a drop in the cross polar cap potential after which Kp and AE began to steadily decline and $SYM-H$ (Dst) began to recover from its minimum value of -33 nT.

Figure 4.4 shows a sequence of selected EUV plasmopause locations from this

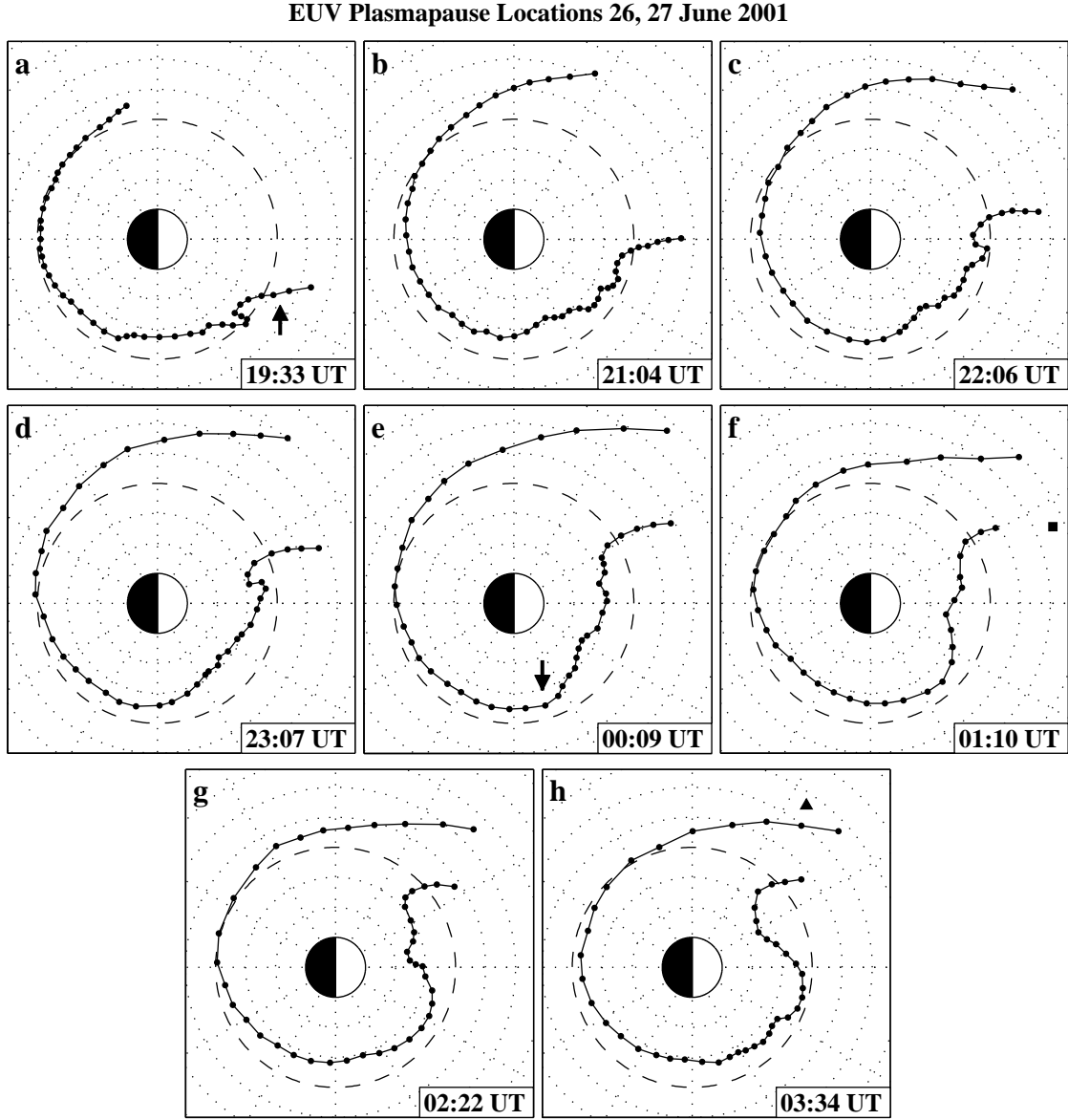


Figure 4.4. EUV extracted plasmopause locations from June 26 – 27, 2001, showing the formation of a plasmaspheric plume and a morningside shoulder. The black square in (f) and the triangle in (h) indicate the approximate UT and MLT times between which *in situ* density observations of the plume are available (Figure 4.6).

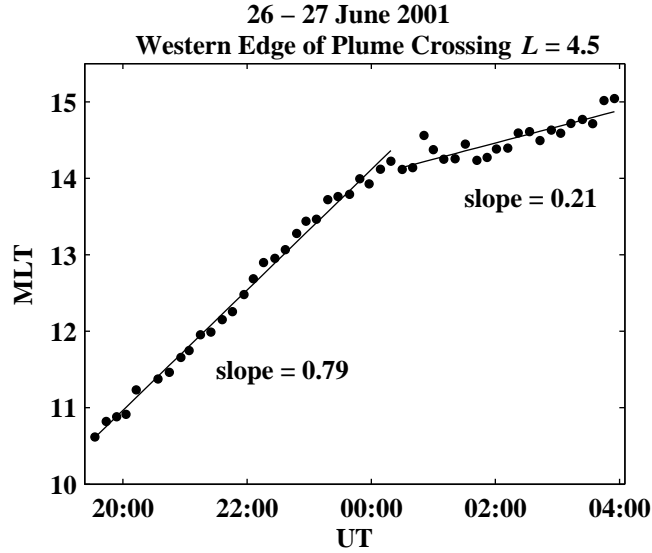


Figure 4.5. The MLT location at which the western edge of the plume crossed $L=4.5$ is tracked as function of UT. The plume rotated at 0.79 of corotation until it crossed $\text{MLT} \simeq 14$ where it slowed to 0.21 of corotation.

interval. Figure 4.4a corresponds to the image taken at 19:33 UT when the satellite was still at a relatively low magnetic latitude ($\lambda \simeq 64^\circ$) such that the plasmopause gradient in the noon to dusk sector was outside of the field of view of the EUV cameras. A comparison of Figure 4.2a and Figure 4.4a shows the inward displacement of the plasmopause boundary across the morningside and the loss of a large volume of plasma especially from 8 to 10 MLT.

By 21:04 UT (Figure 4.4b) IMAGE had moved to a higher latitude and the dusk-side plasmopause had come into the field of view. Near midnight, the plasmopause was located at $L \simeq 3.5$ while plasmaspheric plasma extended to $L > 6$ between noon and 16 MLT. The azimuthal irregularities in the plasmopause radius in the dusk to midnight quadrant seen in Figure 4.2 are no longer apparent, and in fact the nightside plasmopause through the entire sequence appears smooth at least to the resolution of EUV.

Plume Formation

The formation of a plasmaspheric plume can be seen in this sequence as the plasmopause appeared to stagnate in the pre-dusk sector forming the eastern edge of the plume while the western edge of the plume, indicated by the arrow in Figure 4.4a, moved steadily across the noon sector. By 03:34 UT (Figure 4.4h) a distinct plume of cold plasma extended sunward and the minimum plasmopause radius of $L = 2.5$ was located in the local time sector just west or noonward of the plume.

Figure 4.5 tracks the rotation rate of western edge of the plume as a function of UT. Each point represents the MLT location at which the plasmopause on the western edge of the plume crossed $L = 4.5$ for each EUV image from 19:30 UT on June 26, to 04:00 UT on the 27th. From 19:30 to 00:20 the plume edge moved from ~ 10 to 14 MLT at a rate of 0.79 hours of MLT per hour of UT (or equivalently at 79 % of corotation). Once the edge of the plume crossed 14 MLT, its rotation rate slowed considerably to 21 % of corotation.

While azimuthal flows on the dayside formed the western edge of the plume, the location of the plasmopause boundary across the afternoon and evening sector remained relatively stationary, thus forming the eastern edge of the plume. However, there was some motion in those local time sectors. For example from 00:09 UT to 01:10 UT (Figure 4.4e – f) at 18 MLT the plasmopause moved earthward about $0.6 R_E$. This motion can be attributed to unsteady convection due to the variable solar wind IMF during this period. For instance, the radial velocity of the plasmopause at 22 MLT during this period (19:33 UT – 03:55 UT) was correlated with high statistical significance to the strength of IMF B_z with southward IMF leading to radially inward motion. For maximum correlation, the IMF data were shifted an additional 20 minutes.

On the other hand, there does not appear to be a correlation between a change in the IMF and the decrease in the azimuthal velocity of the western edge of the plume (Figure 4.5). It appears that the transition in azimuthal flow may be attributed to the spatial distribution of the magnetospheric flow pattern rather than a temporal change in that flow although it is perhaps unexpected that the transition should occur over such a narrow range in local time.

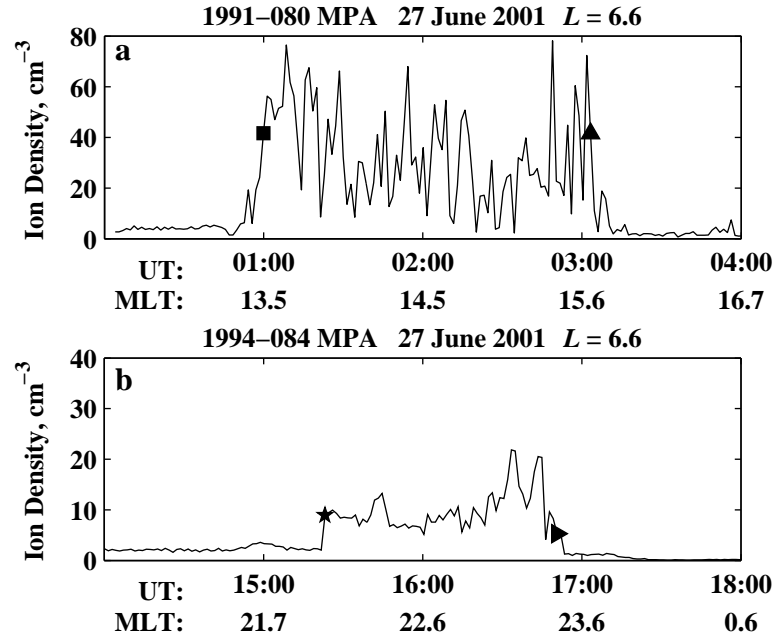


Figure 4.6. *In situ* density measurements of the plume made by LANL satellites 1991–080 and 1994–084 at geosynchronous orbit. (a) The density structure within the plume as it was observed early in the day on June 27, 2001 in the afternoon sector. (b) Reduced densities were observed in the plume later in the day after it had rotated to the pre-midnight sector. The square and triangle (star and right-facing triangle) in panel a (b) correspond to the L and MLT locations indicated in Figure 4.4 (4.7).

Plume Density Structure

The black square in Figure 4.4f at $\text{MLT} \simeq 13.5$ and the triangle in Figure 4.4h at $\text{MLT} \simeq 15.7$ indicate the approximate universal and magnetic local times between which the MPA instrument of the LANL 1991–080 satellite encountered the plume at $L=6.6$. The location of the western edge of the plume (square) is well correlated between the EUV and MPA measurements. However, there is disagreement in the location of the eastern edge (triangle) possibly due to the sensitivity threshold of EUV or the dipole field assumption used in the mapping routines.

The cold ion density profile measured by MPA within the plume is shown in Figure 4.6a. Although not apparent in the global image (perhaps due to the line of sight integration), the plume contained a great deal of irregular structure with average

fluctuations that were $\sim 60\%$ of the mean density value.

Azimuthal Structure

In addition to the formation of the plume, there are several other features of interest in Figure 4.4. Although the nightside plasmapause location varies considerably from $L=5.1$ at dusk to $L=3.4$ at dawn, the variation is quite smooth in azimuth. Yet in the local time sector from approximately dawn to the western edge of the plume, the plasmapause exhibited highly irregular azimuthal structure. This irregular structure can be seen particularly well in Figure 4.4b – e, which correspond to EUV images taken when the IMAGE was at the highest magnetic latitudes so that the distortion of the images due to viewing angle was minimized. These mesoscale variations or “crenulations” on the plasmapause surface are on the order of a few tenths of an R_E and appear to be limited to the local time sector between dawn and the western edge of the plasmaspheric plume.

The formation of a morningside bulge or plasmaspheric “shoulder” was also seen during this event. The appearance of shoulders in EUV global images was first reported by *Burch et al.* [2001]. *Goldstein et al.* [2002, 2003c] in studying two such EUV observations, May 24, 2000 and July 28 – 29, 2000, have proposed that plasmaspheric shoulders can be created in response to an overshielding condition triggered by sudden and strong northward IMF turnings. Overshielding leads to radially outward flows concentrated in the pre-dawn local time sector, producing a bulge which then rotates eastward. *Goldstein et al.* [2002] acknowledged that shoulders may also form under other circumstances as well, for example as a result of outflows in the pre-noon sector resulting from an undershielding condition, and unfortunately in both events studied the initial formation of the shoulder was not observed and the view was limited to the time of its subsequent rotation across the dayside.

The shoulder formation of June 26 – 27, 2001, appears to be initiated by a northward turning of the IMF at $\sim 21:15$ UT. After a time delay of ~ 30 minutes, outward motion was observed across the entire nightside plasmapause while the plasmapause location in the post-dawn sector remained about the same (Figure 4.4c – d). Subsequently at 23:15 the IMF turned southward, and once again after a delay of ~ 30

minutes, the nightside plasmopause began moving inward (Figure 4.4e – f). However, in the intervening time between the northward and southward turnings, plasma from the pre-dawn sector corotated to the post-dawn sector so that following the southward turning and the inward motion pre-dawn, a bulge remained in the post-dawn sector (arrow in Figure 4.4e. The bulge or shoulder continued to rotate eastward, and as it approached the pre-noon sector, began moving outward in L (Figure 4.4g – h).

4.1.4 Recovery Phase

By the time of the third EUV interval indicated as the time period between the dot-dashed lines in Figure 4.1, geomagnetic conditions had quieted significantly, and the magnetosphere was in a recovery phase.

Plume Rotation

A sequence of four EUV extracted plasmopause locations from this interval is shown in Figure 4.7. Figure 4.7a was taken ~ 6.8 hours after Figure 4.4h in which time the entire plasmaspheric plume rotated ~ 4.25 hours of magnetic local time to the post-dusk sector. The irregular azimuthal structure observed earlier just west of the plume still persisted and a wide bulge had formed pre-noon. It is likely that the plume began to rotate through the dusk sector sometime around or after 04:00 UT corresponding to the abrupt drop in the polar cap potential.

The rotation rate of the plume was measured by tracking the MLT location of the $L=4$ plume crossing for each EUV image from 10:22 to 17:43 (Figure 4.8). Both the western and eastern edges of the plume rotated at 87% of corotation for the entire interval.

Density Structure

Prior to the EUV image at 10:22, the IMAGE satellite passed through perigee, and the electron density profile along the orbit was measured by RPI (Figure 4.9a). Figure 4.9b is a dawn to dusk meridional slice (viewed from the sun direction) indicating the orbit of the IMAGE satellite along with shading where RPI encountered regions of

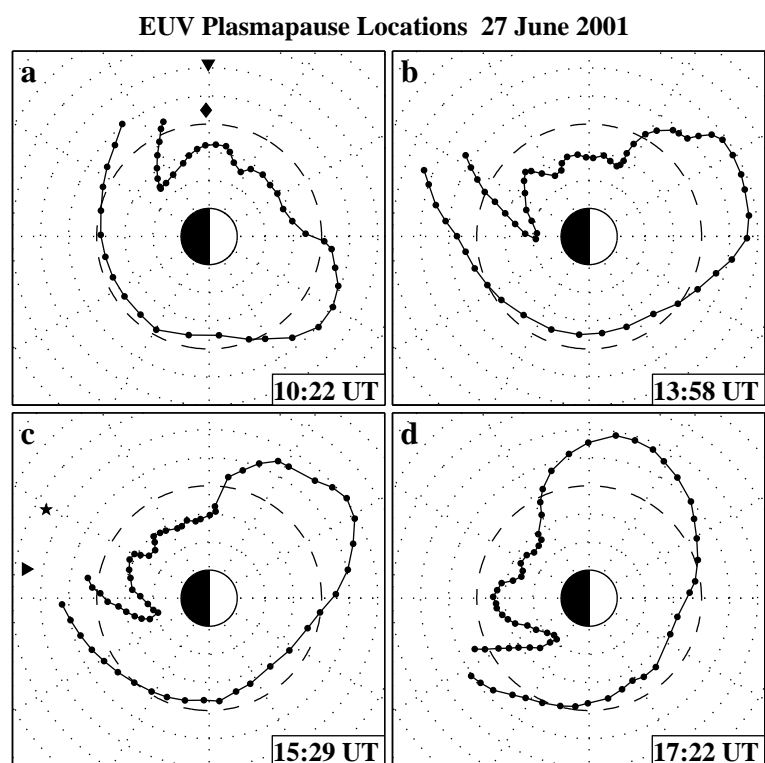


Figure 4.7. EUV extracted plasmopause locations from June 27, 2001 showing the rotation of the plume across the nightside. *In situ* density measurements are available between the down-facing triangle and the diamond (star and right-facing triangle) in Figure 4.9 (4.6).

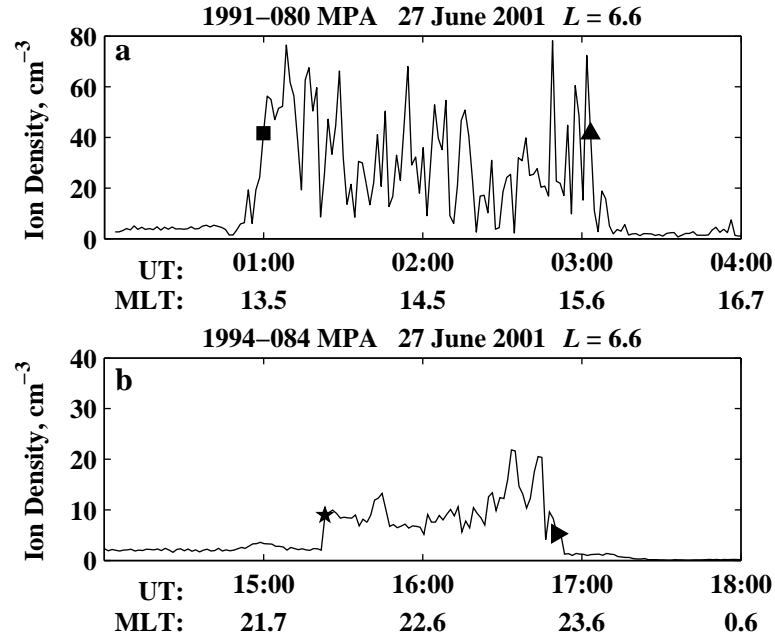


Figure 4.8. The MLT location at which both the eastern and western edge of the plume crossed $L=4.0$ is tracked as a function of UT.

enhanced electron density. On the inbound portion of the orbit (dawn), RPI measured the steep plasmapause gradient at $L \simeq 3.4$. As the satellite then traveled outbound in the dusk sector, RPI measured a steep gradient at $L \simeq 2.6$ which corresponds to the sector of low L just west of the base of the plume in Figures 4.4h and 4.7a. An outlying region of enhanced density was then observed between $L \simeq 4.5$ and $L \simeq 6.1$. This outlying density region was the mid-latitude field-aligned extension of the plasmaspheric plume at an intermediate MLT position between Figures 4.4h and 4.7a. The black diamond and triangle in Figure 4.7a correspond to those of Figure 4.9 and indicate the L extent of the plume as measured by RPI.

The peak electron density in the plume region was 168 cm^{-3} at the lower L edge of the plume (which corresponds to the western edge as observed by EUV), and the density within the plume varied relatively smoothly. Although the RPI data show a smoother profile than that observed by MPA (Figure 4.6a), it should be noted that the spatial and temporal resolution of RPI (147 seconds, 520 km in the plume region) is about half that of the MPA instrument (86 seconds, 254 km).

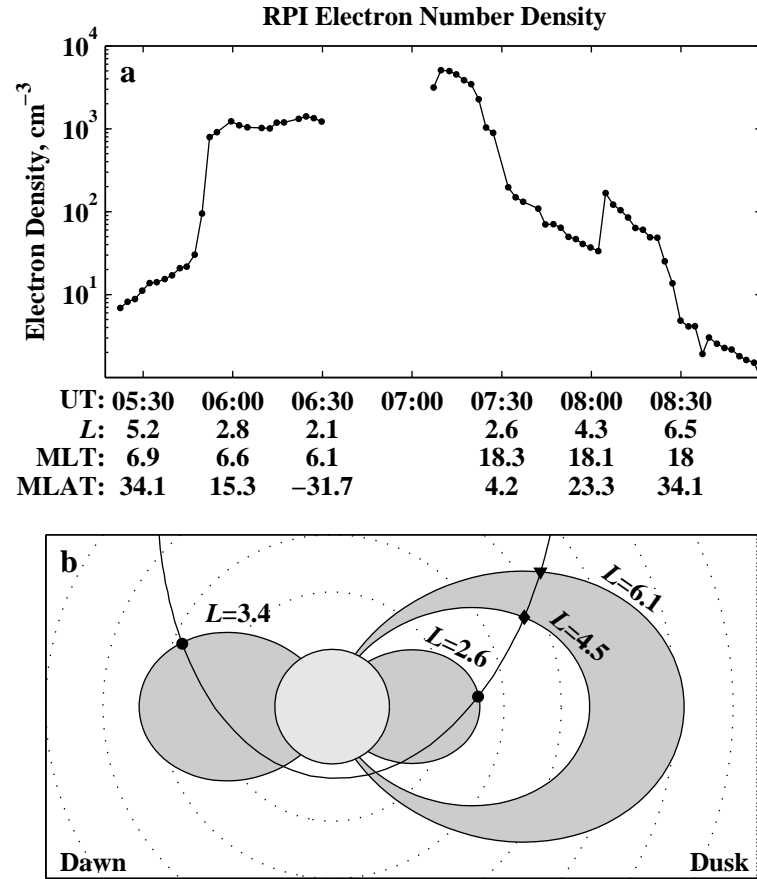


Figure 4.9. (a) *In situ* electron density profile observed by IMAGE RPI along the orbit of panel (b). Shaded regions in (b) indicate where RPI encountered the main plasmasphere in the dawn and dusk sectors as well as an outlying density enhancement at dusk.

In Figure 4.7c in the local time sector between the star and the right-facing triangle, the LANL 1994–080 satellite passed through the plume, and the density profile observed is shown in Figure 4.6b. The average density within the plume has been reduced to $\sim 10 \text{ cm}^{-3}$ from $\sim 33 \text{ cm}^{-3}$ as measured in the previous geosynchronous encounter some 12 hours earlier. The density reduction within the plume is presumably due to the loss of plasma resulting from sunward outflows during the earlier periods of enhanced convection.

In the EUV images from later in the day on June 27 to early hours of June 28, 2001, the remnants of the plume could still be seen as it rotated across the dayside. However, due to refilling the edges of the plume became quite hazy and less distinct.

4.2 Case II: June 9 – 10, 2001

The second study interval of June 9 – 10, 2001 was a time of a slightly larger and more complicated disturbance than the previous example. Geomagnetic and solar wind conditions for a 46 hour period from 02:00 UT on June 9 to 24:00 UT June 10 are shown in Figure 4.10. The bottom panel displaying ACE MAG solar wind B_z data has been time shifted by 59.4 minutes from the beginning of the interval to 12:00 UT on June 9 and 44.5 minutes afterward to account for the average propagation delay to the magnetopause during those intervals. Quiet conditions prevailed prior to the disturbance with Kp remaining below 2+ on June 8, 2001, and during the peak of the disturbance Kp reached a maximum of 5+ and $SYM-H$ a minimum of -44 nT . However the evolution of the plasmaspheric density structures differs considerably from the June 26 – 27, 2001 case due to a multi-staged disturbance onset and recurring substorm activity after the main disturbance.

Four EUV image collection intervals are indicated in Figure 4.10 by the sets of matching vertical lines with the beginning of the first interval and end of the last interval outside the range of the plot. Unfortunately due a spacecraft pointing error, only a total of ~ 20 high quality EUV images were available for the first 2 intervals of Figure 4.10, and therefore precise calculations of radial or azimuthal motions for these intervals cannot be presented only general trends. Full 10-minute resolution

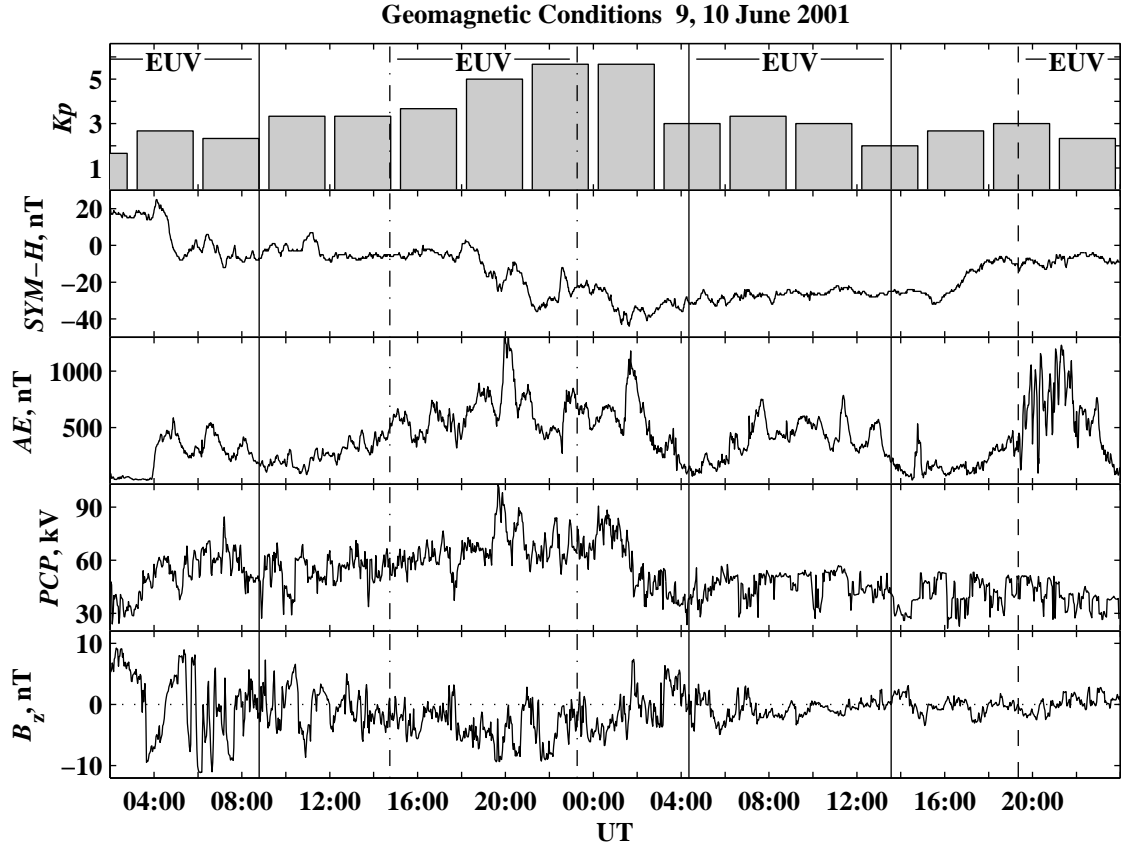


Figure 4.10. Geomagnetic and solar wind conditions for a 46 hour period from 02:00 UT on June 9 to 24:00 UT on June 10. The format is identical to that of Figure 4.1. Four EUV image collection intervals are indicated the sets of matching vertical lines with the beginning of the first interval and end of the last interval outside the range of the display.

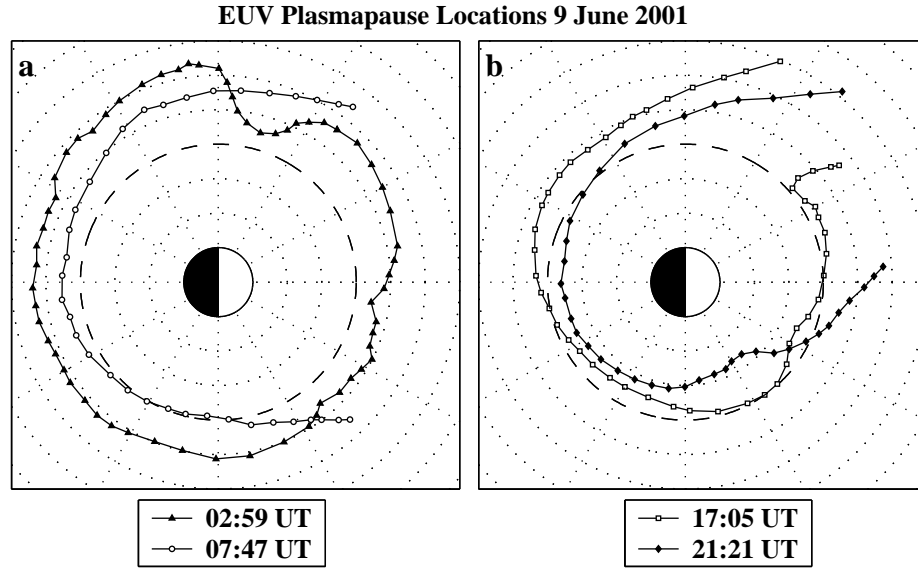


Figure 4.11. EUV plasmopause locations on June 9, 2001 at the times indicated in the legends.

images were available for the third and fourth EUV intervals.

4.2.1 Multi-staged Onset

The plasmopause location, extracted from the EUV image of June 9, 02:59 UT, prior to the disturbance commencement is indicated by the curve connecting the solid triangles in Figure 4.11a. The average plasmopause location was $L = 5.3$, yet in the dusk sector an azimuthal variation of $> 1.5 R_E$ was present within one hour of magnetic local time.

An increase in geomagnetic activity on June 9, 2001, occurred in two stages as perhaps can be seen best in the $SYM-H$ index in Figure 4.10. $SYM-H$ dropped sharply after 04:00 UT in response to a southward turning of the IMF about 20 minutes earlier, remained fairly steady for many hours until 18:00 UT when it began to decline, again correlated with a southward IMF turning about 20 minutes prior.

Initial Nightside Erosion and Plume Formation

An inward motion of the plasmapause boundary was first captured in eight EUV images between 04:00 and 08:00 UT, and the plasmapause location at 07:47 UT is indicated by the line connecting the hollow circles in Figure 4.11a. The plasmapause location on the entire nightside (dusk to dawn) was reduced by $\sim 1 R_E$ with the bulk of that motion occurring before 06:00 UT. The azimuthal variation near dusk was smoothed apparently as a result of sunward flows in that sector. Also, a sunward motion of plasma moved the plasmapause outside of the EUV field of view across much of the dayside.

The plasmapause location at 17:05 UT (second EUV interval) after ~ 9 hours of fairly steady conditions is indicated by the hollow squares in Figure 4.11b. The plasmapause in the pre-midnight sector was located at approximately the same radial distance as at 07:47 UT but had drifted slightly inward post-midnight. A plasmaspheric plume had formed in the afternoon sector due to corotation flow across the dayside as was shown in Figure 4.4 for June 26 – 27, 2001. In addition, azimuthal variations in the plasmapause radius had formed from dawn to the western edge of the plume.

Secondary Erosion and Sunward Surge

The combined effects of the second stage of geomagnetic activity can be seen from the location of the plasmapause at 21:21 UT, solid diamonds in Figure 4.11b. The plasmapause moved inward $\sim 0.7 R_E$ at midnight, and sunward flows moved the eastern edge of the plume to earlier local times with the $L=6$ crossing moving from 17.3 MLT to 16.2 MLT. However, the most pronounced motion from 17:05 UT to 21:21 UT was a sunward surge of plasma on the dayside. For example at a magnetic local time of 14:00, the plasmapause moved from $L=4.4$ to $L \geq 6$. This outward motion effectively moved the western edge of the plume to an earlier magnetic local time.

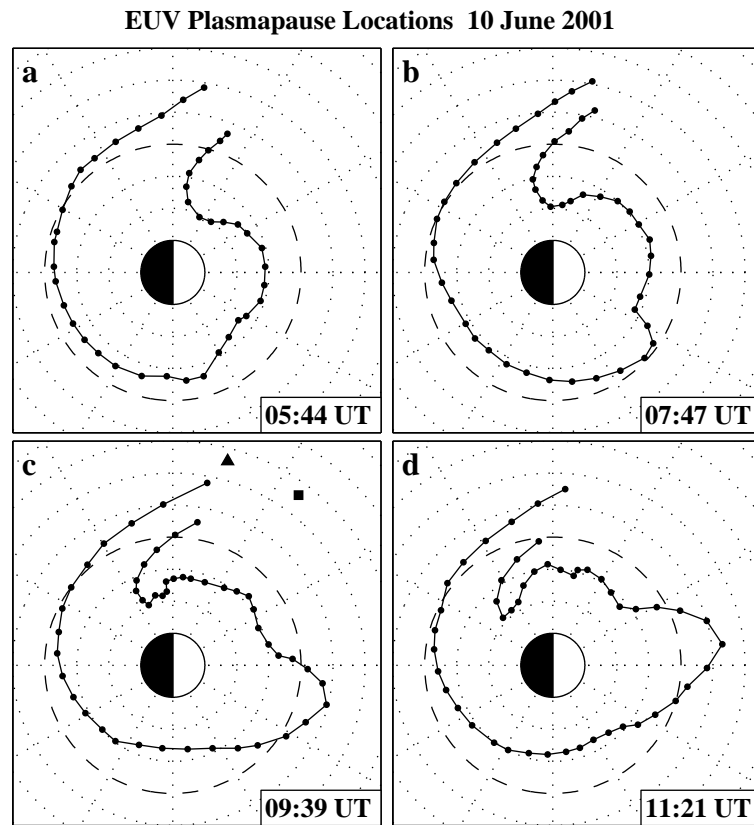


Figure 4.12. EUV plasmopause locations on June 10, 2001 showing the wrapping of the plume around the main plasmasphere and the formation of prominent bulge or shoulder on the dayside. *In situ* density measurements in the region between the square and the triangle in (c) are shown in Figure 4.14.

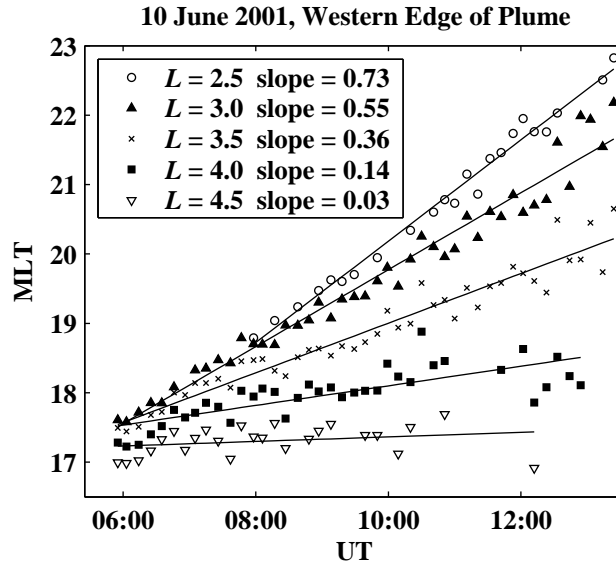


Figure 4.13. The rotation rate of the western edge of the plume is tracked at different L values. The plume rotated faster at lower L .

4.2.2 Recurrent Substorm Activity

After $\sim 06:00$ UT on June 10, the IMF B_z hovered near zero, but the AE index indicated that substorm activity continued throughout the remainder of the day. The evolution of plasmaspheric density structures during the third EUV interval from Figure 4.10 is captured in Figure 4.12. At 05:44 UT (Figure 4.12a) a well defined plume was present in the dusk sector with the plasmapause at $L=2$ in the local time sector just west of the plume. The subsequent snapshots show that this low L sector along with the western edge of the plume rotated toward midnight while the eastern edge of the plume remained stationary.

Wrapping of the Plume

Using all of the extracted plasmapause locations from 05:50 UT to 13:24 UT, the azimuthal motion of the western edge of the plume was tracked as a function of L . Various symbols in Figure 4.13 indicate the L shell crossing of the western edge of the plume from $L = 2.5$ (hollow circles) to $L = 4.5$ (hollow inverted triangles) as a

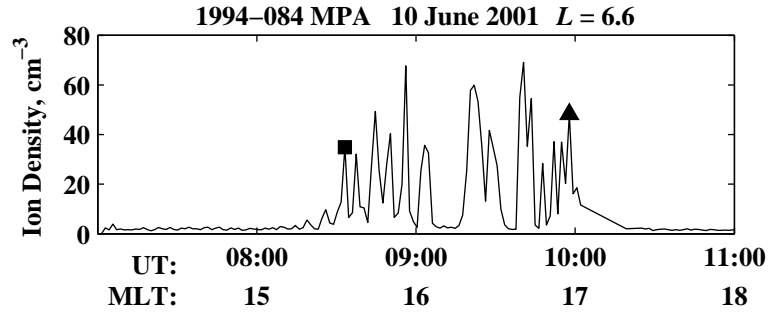


Figure 4.14. *In situ* density measurements of the plume at geosynchronous orbit corresponding to the local time between the triangle and square in Figure 4.12.

function of MLT and UT. The slope of the line fitted to each set of points yields the azimuthal motion of the boundary in hours of MLT per hour of UT or equivalently as a percentage of corotation. At $L = 2.5$, the plume rotated at 0.73 of corotation, at $L = 3.5$ at only 0.36 of corotation, and at $L = 4.5$, the plume edge was basically stationary. Differential rotation of the western edge of plume in L and the stagnation of the eastern edge led to the formation of a low density channel and the wrapping of the plume around the main plasmasphere.

Plume Density Structure

The 1994–084 satellite passed through the plume along its geosynchronous orbit in approximately the region indicated between the black square and the triangle Figure 4.12c. The cold density measured by the MPA instrument, Figure 4.14, shows the highly irregular density structure within the plume with average density fluctuations that were $\sim 90\%$ of the mean.

Azimuthal Structure

The sequence shown in Figure 4.12 also captured the development of a shoulder type feature on the dayside. In Figure 4.12a the shoulder can be seen as a slight ($\sim 0.1 - 0.2 R_E$) bulge just post-dawn which moved outward as it corotated to become a large scale protrusion near noon in Figure 4.12d. The outward motion of the shoulder was tracked by following the plasmopause location at a magnetic longitude of 95° as

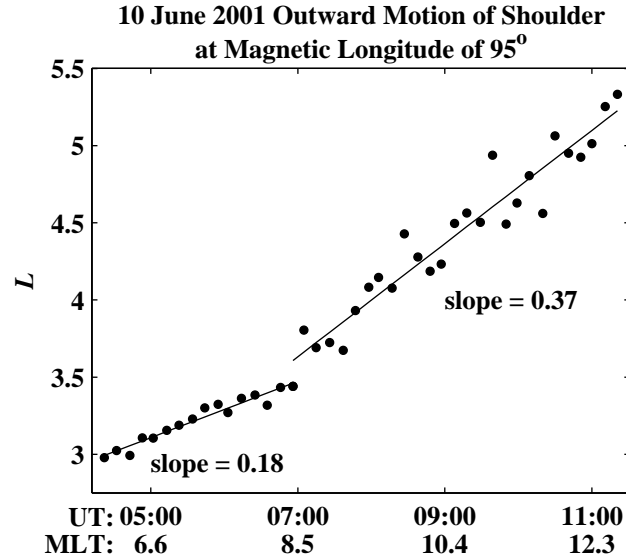


Figure 4.15. The outward motion of the shoulder on June 10, 2001 at a magnetic longitude of 95° is tracked by as function of L and UT.

shown in Figure 4.15. From 04:22 UT to 06:55 UT, the shoulder moved outward at a rate of 0.18 L per UT hour after which the rate doubled to 0.37 L per hour.

Multiple Plume Formation

At 13:30 UT the EUV cameras were turned off for several hours, and at the start of the fourth EUV interval of Figure 4.10, Figure 4.16 shows the extracted plasmopause location from the EUV image taken at 19:29 UT. The channel of low density cold plasma between the main plasmasphere and the plume extended from 21 MLT to 06 MLT. The width of the channel was ~ 0.5 to $0.6 R_E$ from midnight to 05 MLT. Again mesoscale crenulations on the plasmopause surface have formed on dayside.

A second plasmaspheric plume is also present in Figure 4.16 which appears to have been formed by the rotation of the shoulder feature into the dusk sector. Differential azimuthal velocities in L on the western edge have formed the distinct plume shape. Using the results of a numerical simulation, *Lemaire* [2000] proposed that plasmaspheric plumes could be formed in just this manner. The model predicts that a bulge can develop in the pre-noon sector as a result of enhanced sunward convection in

EUV Plasmopause 10 June 2001 19:29 UT

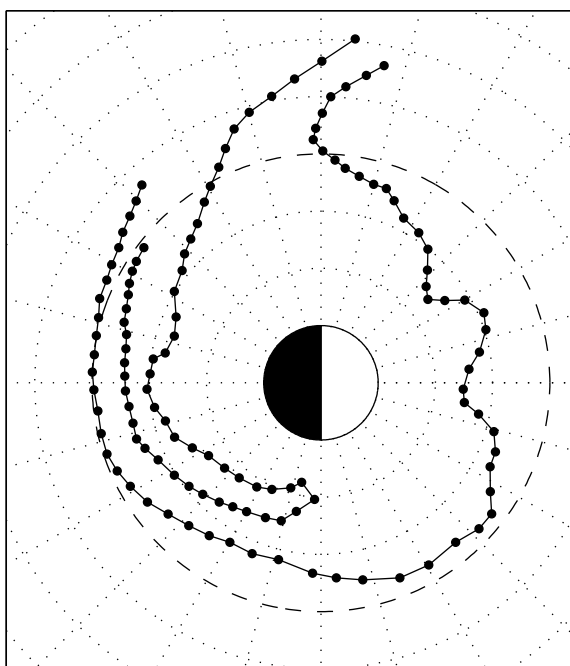


Figure 4.16. EUV extracted plasmopause location from 19:29 UT on June 10, 2001. The plasmaspheric plume has wrapped around the main plasmopause and second plume has formed as a result of the rotation of the shoulder into the dusk sector.

the 08 – 14 MLT sector which then rotates eastward and develops into a plume like feature as a result of smaller azimuthal velocities at larger equatorial distances.

In the subsequent EUV images of this interval, the plume that was present in the dusk sector at 19:29 UT began to wrap around the main plasmasphere while the channel across the nightside became less distinct possibly due to the refilling of this region from the underlying ionosphere.

4.3 Conclusions

We presented here two detailed case studies of the global dynamics of the plasmasphere during geomagnetically disturbed periods. This work is part of a larger set of case studies, the results of which appear consistent with the general morphology presented for the June 26 – 27, and June 9 – 10, 2001 events. Among our findings are both essentially new results and also results that confirm and extend previous work. We find that the plasmasphere is highly structured and complex, but clearly reproducible features evolve during disturbed periods.

When geomagnetically quiet conditions have prevailed for a day or two, the EUV imager observes an expanded plasmasphere, and although the average plasmopause radius can extend to greater than $L \simeq 5$, significant azimuthal variations that have formed during previous disturbed periods can persist. Thus, quieting had evidently not led to the large dawn-dusk asymmetry or tear-drop form that has been used in introductory discussions of the “steady state” plasmasphere shape [e.g. *Parks*, 1991, pp. 229 – 237; *Wolf*, 1995, pp. 314 – 317]. Furthermore, the mesoscale irregularities in radius are not predicted in traditional explanations of plasmasphere behavior during recovery periods [e.g., *Chen and Wolf*, 1972].

At the onset of a geomagnetic disturbance, inward motion of the plasmopause across the nightside can be observed, with rates greater than 0.5 L per hour, along with a sunward surge of plasma on the dayside. The onset of erosion is correlated with a southward turning of the IMF B_z with a time delay on the order of 20 to 30 minutes. For the June 26 – 27, 2001 event, the instantaneous velocity of the plasmopause on the nightside was highly correlated to the strength of the IMF B_z . Also, any azimuthal

variations in the plasmopause radius existing across the nightside appear to become smoothed out near the onset of erosion.

A distinct plasmaspheric plume forms after a period of ~ 12 hours, as a result of sunward flows from dusk which form the eastern edge of the plume and corotational flows across the dayside which form the western edge of the plume.

Bulges or shoulders are frequently observed in the morning sector during disturbed periods. In the June 26 – 27 case, the formation of a shoulder was attributed to a combination of a northward turning of the IMF followed ~ 2 hours later by a southward turning. In the June 9 – 10, 2001 event, a particularly large shoulder feature developed into a plume shape in the afternoon sector as a result of differential rotation velocities in L . Differential rotation does not appear to be the primary plume formation mechanism, since such large dayside bulges have not been observed in the other cases studied so far. Further work is required to determine the degree to which plumes may form in this manner.

In addition, crenulations on the plasmopause surface on the order of ≤ 0.5 in L and ≤ 2 hours MLT are regularly observed during disturbed times, and their formation appears to be limited to the local time sector between dawn and the western edge of the plume. Conversely, the nightside plasmopause tends to remain rather smooth throughout the disturbance.

During June 26 – 27, 2001, after the main disturbance the magnetosphere entered a period of deep quiet, and thus corotational flows dominated the inner magnetosphere. The plasmaspheric plume was observed to rotate rather rigidly with the main plasmasphere from the afternoon sector across the nightside at a rate slightly less than the corotation velocity.

In contrast, during June 9 – 10, 2001, the plume became wrapped around the main plasmasphere and a low density channel was formed between the plume and the main plasmasphere. The wrapping of the plume is attributed to the lingering geomagnetic activity after the main disturbance as indicated by the AE index. By tracking the eastern edge of the plume in the afternoon sector, we were able to observe the transition from primarily corotational flows at low L to sunward directed convection, associated with substorm electric fields, at higher L .

In situ density data for these events show highly irregular density structure within the plume as measured at geosynchronous orbit ($L=6.6$) whereas a measurement by IMAGE RPI suggests there may be less structure near the base of the plume closer to the main plasmasphere. This assertion requires further investigation in view of the lower temporal and spatial resolution of RPI.

During these events as well as others studied but not presented here, we do not find evidence of dense plasma elements that are detached from the main plasmasphere. In the afternoon sector, plasmaspheric plumes appear to remain connected to the plasmasphere in contrast to earlier interpretations of *in situ* observations by Chappell [1974]. In addition, we do not see evidence of the detachment of plasma in the post-midnight local time sector as proposed by Lemaire [2001]. However, the existence of detached plasma cannot be completely ruled out at this stage, and the lack of observation by EUV may result from limitations of the instrument. For example, it is possible that detached elements may lie outside the EUV field of view (generally less than L of 5 to 6), be below the sensitivity threshold (equivalent to about 30 electrons cm^{-3}), or be washed out by the effects of the line of sight integration.

The ability to track the plasmopause on a global scale has led to new or broader insights on the plasmasphere dynamics during relatively weak to moderate geomagnetic disturbances. However, many additional questions remain to be answered such as those concerning the response of the plasmasphere during great magnetic storms, the loss of plasma along and perpendicular to the magnetic field, and the behavior at densities below the present EUV threshold.

Chapter 5

The Loss of Plasmaspheric Plasma

The previous chapter focused on characterizing the evolving shape of the plasmasphere during a geomagnetic disturbance. In this chapter, we focus on quantifying the amount of plasma removed from the plasmasphere during a set of disturbed periods.

5.1 Estimating Plasma Loss

Five disturbance periods were selected in order to study the loss of plasmasphere material as observed globally by the EUV imager: May 8 – 9, 2001; May 28, 2001; June 2, 2001; June 18, 2001; June 26, 2001. For each disturbance, two EUV images were selected, one from before or near the disturbance onset and another from near the end of the main phase or the beginning of recovery. The two images were selected one orbit apart with the requirement that at all magnetic local times, $L \leq 5.5$ was within the field of view. The total time between the “before” and “after” images was between 12.4 and 15.5 hours for each of the five events.

Figure 5.1 shows an example from June 18, 2001. The EUV image at 02:53 UT (Figure 5.1a) captured the He^+ distribution in the plasmasphere before the disturbance onset, and ~ 14.1 hours later, the image from 17:01 UT (Figure 5.1b) captured the beginning of the recovery phase. In order to directly compare the two images, the regions outside $L = 5.5$, inside $L = 1.5$, and behind the Earth in the shadow region are masked out. Qualitatively, a comparison of the two EUV images shows that a

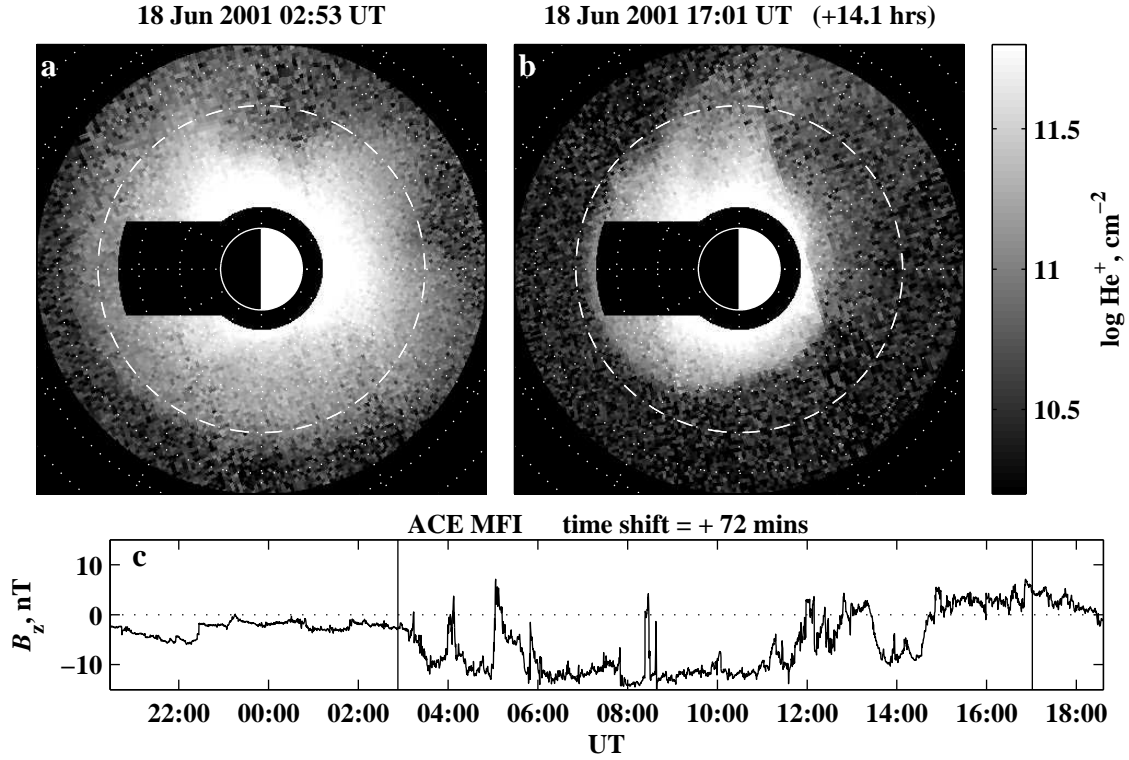


Figure 5.1. Equatorially mapped EUV images before the disturbance onset (panel a) and at the beginning of the disturbance recovery (panel b) for June 18, 2001. The image has been masked out for $L < 1.5$, $L > 5.5$, and in the shadow region. Panel c shows the ACE IMF B_z in GSM coordinates with a propagation delay of 72 minutes applied. The vertical lines indicate the times of the EUV images.

large volume of plasma has been removed especially from the outer plasmasphere. During the intervening time between the two images, the IMF B_z (Figure 5.1c) had been strongly southward for many hours. A plasmaspheric plume had formed and after the northward IMF turning at $\sim 15:00$ UT, began to rotate through the dusk sector. Similar displays for the other 4 events are shown in Figures 5.2 – 5.5.

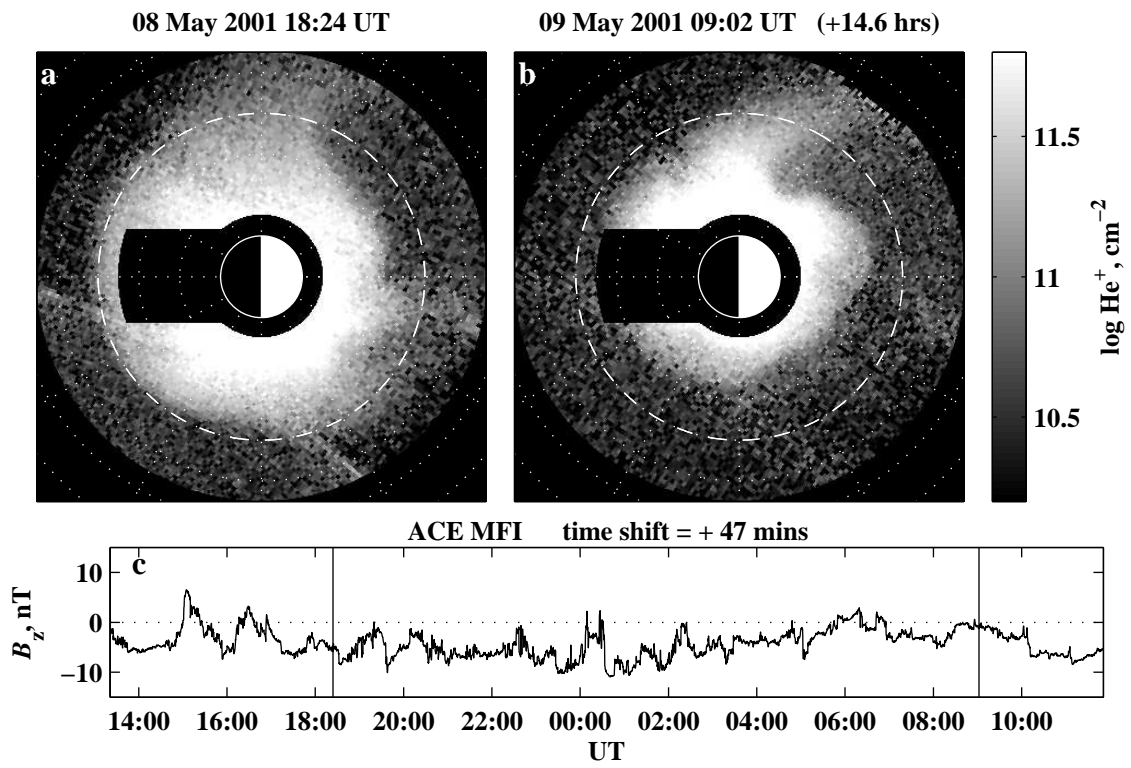


Figure 5.2. Same format as Figure 5.1 for the May 8 – 9, 2001 disturbance.

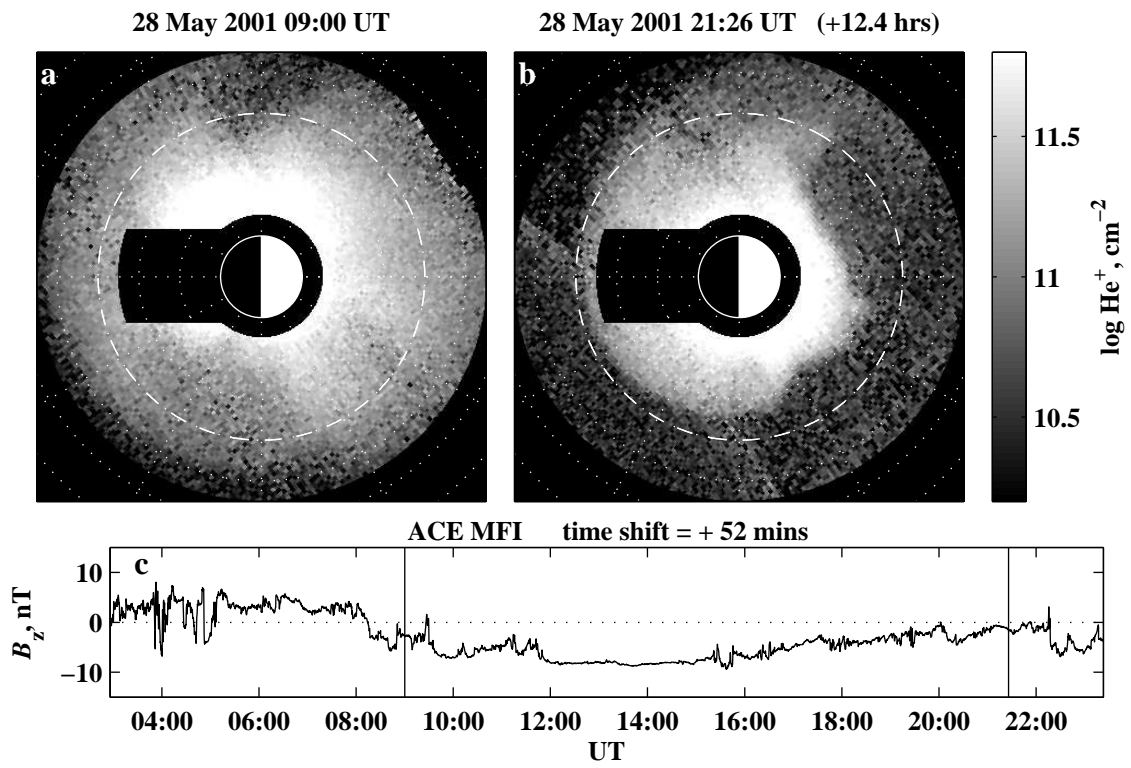


Figure 5.3. Same format as Figure 5.1 for the May 28, 2001 disturbance.

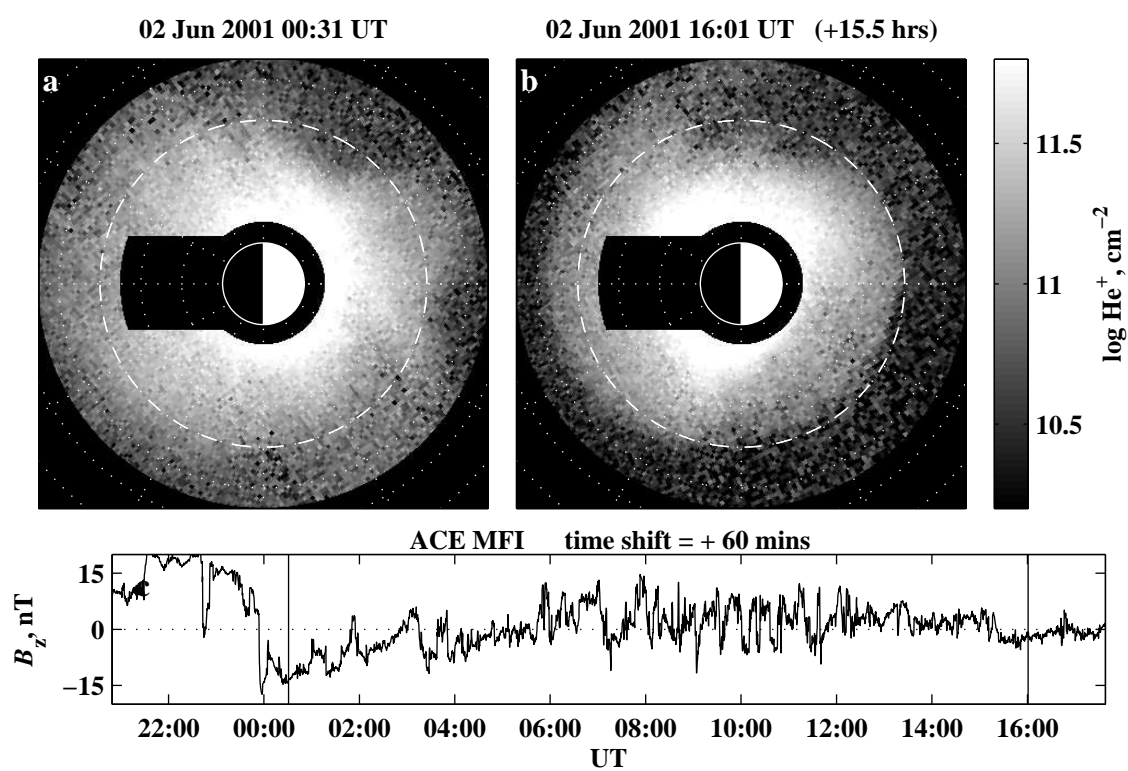


Figure 5.4. Same format as Figure 5.1 for the June 02, 2001 disturbance.

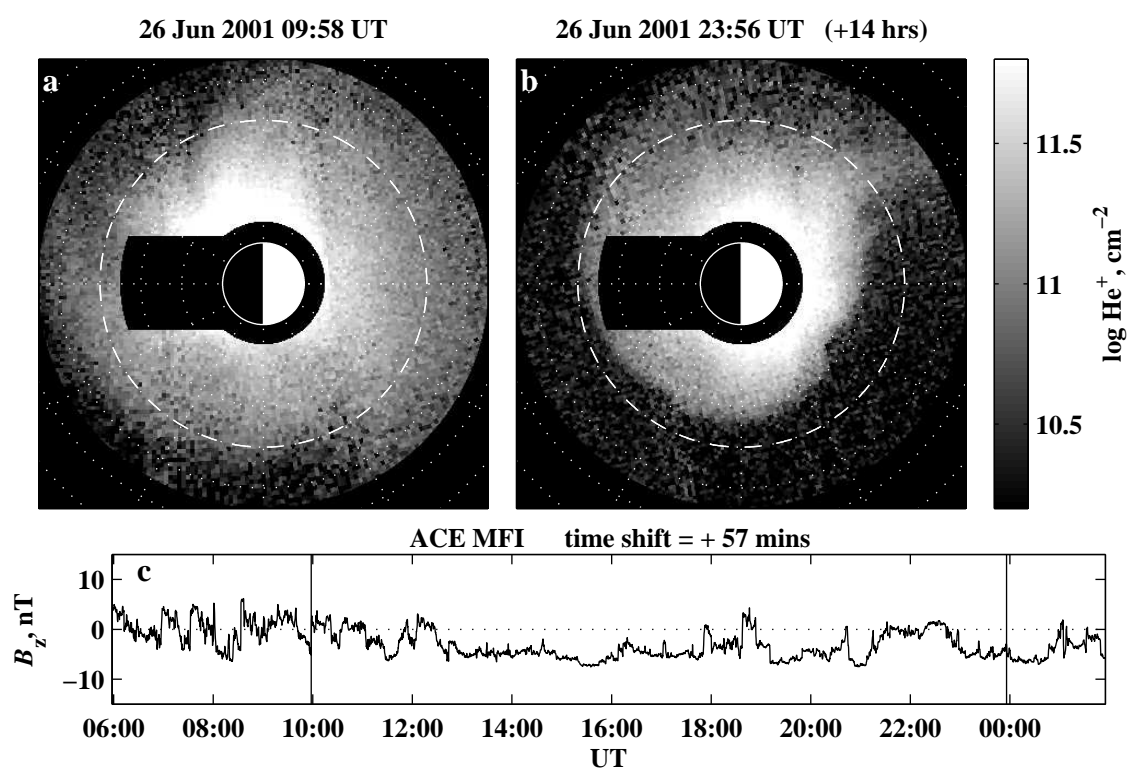


Figure 5.5. Same format as Figure 5.1 for the June 26, 2001 disturbance.

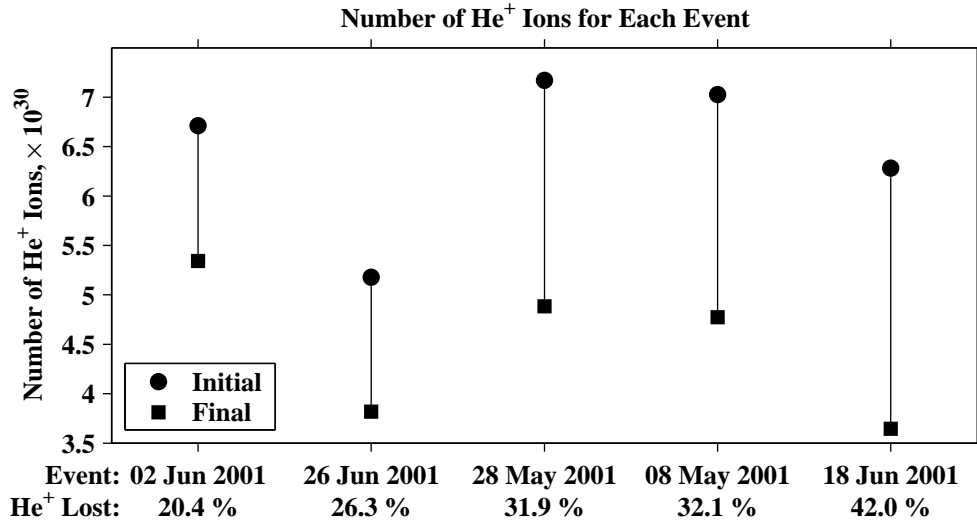


Figure 5.6. The initial and final He^+ abundance as well as the loss percentage for each of the five events.

5.1.1 Calculating the Amount of He^+ Removed

For each of the five disturbance periods, the total number of He^+ ions in the plasmasphere before and after the disturbance was calculated by integrating the He^+ column density over the entire equatorial plane (excluding the masked out regions), and the results are summarized in Table 5.1 and Figure 5.6. For each of the events, $\sim 1\text{--}3 \times 10^{30}$ He^+ ions were lost which constituted between 20 % and 42 % of the initial He^+ distribution.

Event	He^+ Ions Start	He^+ Ions End	He^+ Ions Lost	% Lost	ΔUT , hrs
02 Jun 2001	6.71×10^{30}	5.34×10^{30}	1.37×10^{30}	20.4 %	15.5
26 Jun 2001	5.18×10^{30}	3.82×10^{30}	1.36×10^{30}	26.3 %	14.0
28 May 2001	7.17×10^{30}	4.88×10^{30}	2.29×10^{30}	31.9 %	12.4
08 May 2001	7.03×10^{30}	4.77×10^{30}	2.25×10^{30}	32.1 %	14.6
18 Jun 2001	6.28×10^{30}	3.65×10^{30}	2.64×10^{30}	42.0 %	14.1

Table 5.1. Summary of the He^+ loss calculations for the five disturbance periods.

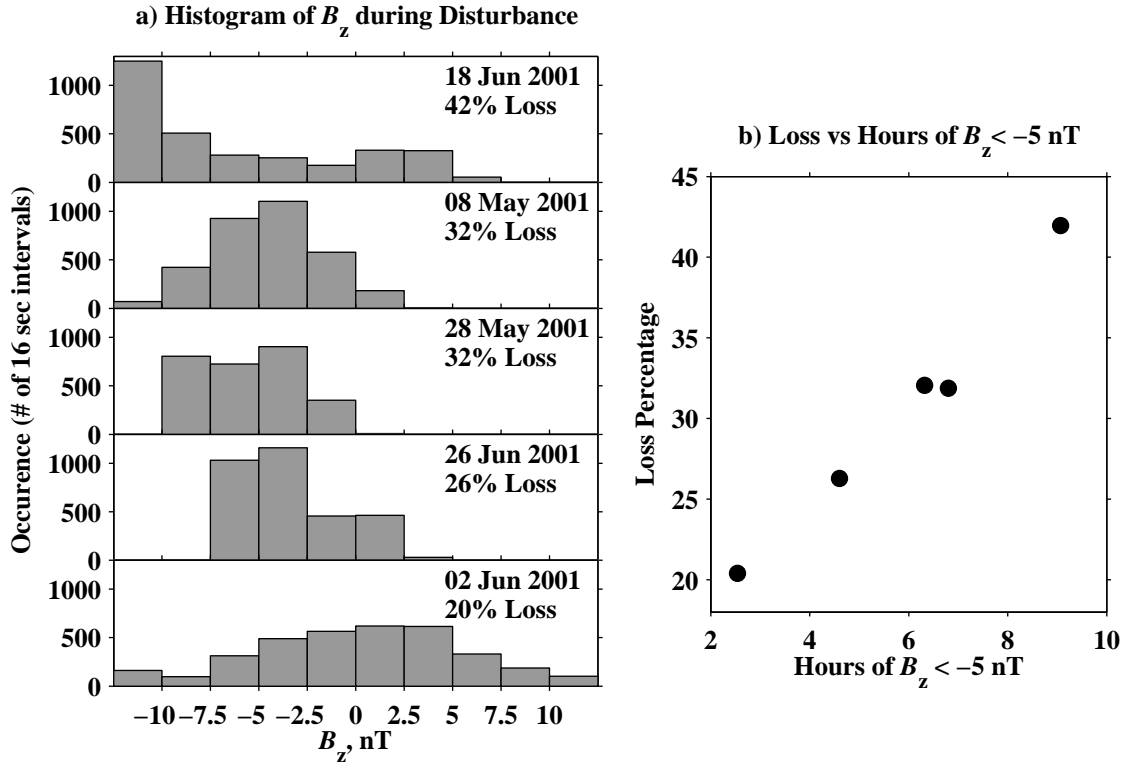


Figure 5.7. Panel a shows a histogram of the IMF B_z as observed by the ACE MFI instrument in GSM coordinates during the disturbance interval. Panel b shows the relationship between the percentage of lost He^+ during the disturbance with the number of hours of $B_z < -5$ nT.

5.1.2 Correlation of the Loss Percentage with IMF B_z

An attempt was made to correlate the percentage of He^+ lost to various geophysical parameters such as the magnetic indices Kp and Dst as well as solar wind parameters number density, velocity, and IMF. The only direct correlation was found to be with the strength and direction of the IMF B_z . This result is perhaps not surprising given that global magnetospheric convection is driven by magnetic field line reconnection between oppositely directed solar wind and terrestrial magnetic fields. In addition, strong coupling between motion of plasma in the inner magnetosphere and the strength and direction of B_z was established in Chapter 4.

Figure 5.7a shows a histogram of the value of B_z during the disturbance interval

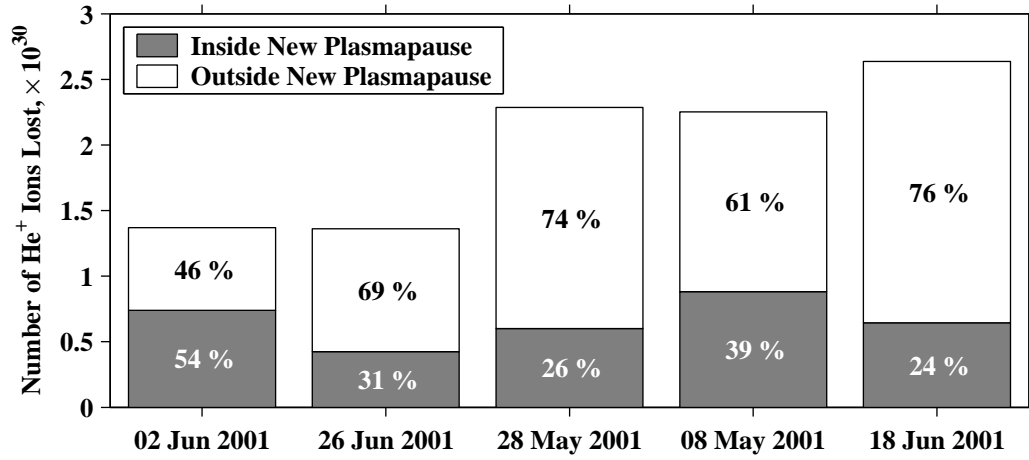


Figure 5.8. The total number of He^+ ions removed from the plasmasphere is broken down by the estimated amount lost inside versus outside the new plasmopause boundary. For example on June 18, 2001, 76 % of the plasma loss occurred outside the new plasmopause boundary.

(time between the solid vertical lines in Figures 5.1c – 5.5c). Occurrence is defined as the number of 16 second samples in each range of B_z values. The events have been ordered from top to bottom by decreasing total percentage loss. For the event with the lowest percentage loss, June 02, 2001, the values of B_z are distributed among positive and negative values, with a low occurrence of strongly negative values. As the loss percentage increases so does the occurrence of southward IMF, and the event with highest loss percentage has a strong peak in the histogram for $B_z < -10$ nT. Figure 5.7b shows a linear relationship between the total number of hours of $B_z < -5$ nT and the loss percentage. The total number of hours of $B_z < 0$ did not correlate with loss percentage as well since the 3 middle events (May 28, 2001; May 08, 2001; and June 26, 2001) all had more total hours of $B_z < 0$ than the largest loss event (June 18, 2001). Nevertheless, the many hours of strongly negative B_z appear to be important in contributing to the large loss percentage on June 18, 2001.

5.1.3 Comparing Losses Inside and Outside the New Plasmopause

Next, we estimate the amount of He^+ lost inside versus outside the new plasmopause boundary. In the second of the set of two images for each case, a plasmopause boundary was selected, and the two images were compared on either side of that boundary. The results are shown in Figure 5.8. For all except the June 2, 2001 event, a greater percent of the total loss occurred outside the newly established plasmopause boundary.

However, it is important to note that the shadow region for all of the cases was almost entirely contained within the new plasmopause so that any loss in that region is not properly accounted for. On the other hand, as discussed in Section 3.3.1, points mapped inside the plasmopause boundary contain contributions from other field lines due to the line of sight integrated nature of the EUV measurement. Thus, the loss inside the new boundary (the shadow region excluded) is slightly overestimated.

In order to more accurately determine the loss on either side of the boundary, an image inversion could be performed to produce a three-dimensional density distribution. This procedure would also have some uncertainty, since the inversion inherently depends on the assumed field aligned distribution.

5.1.4 Estimating the Total Mass of Material Lost

In order to calculate the total mass of material lost from the plasmasphere for each of the disturbed periods, an assumption needs to be made on the relative concentration of He^+ to the other ion species, primarily H^+ and O^+ . One simple approach is to use a constant density ratio between species throughout the entire plasmasphere. However, a more accurate estimate can be made by using an empirical relationship derived from a statistical study of data from the retarding ion mass spectrometer (RIMS) on the Dynamics Explorer [Craven *et al.*, 1997]. Using DE 1/RIMS data over a 3.25 year period covering both high and low solar activity, this study examined the number density ratio

$$\alpha = \frac{n_{\text{He}^+}}{n_{\text{H}^+}}$$

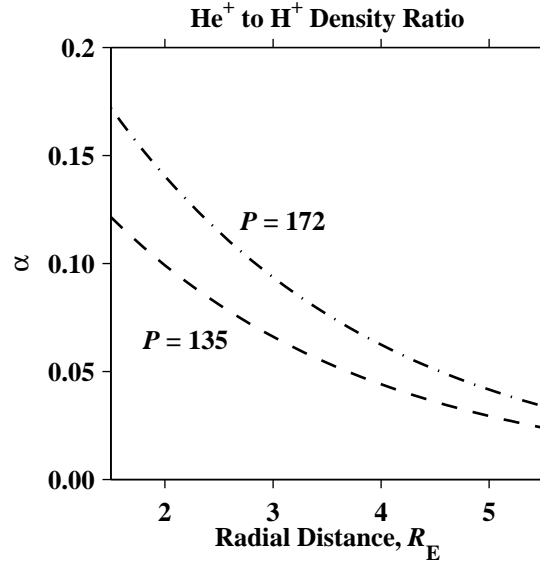


Figure 5.9. The He^+ to H^+ density ratio as a function of radial distance for the minimum ($P=135$) and maximum ($P=172$) solar activity of the five study intervals.

and found that α is primarily a function of geocentric distance and the solar EUV input. The ratio appeared to have no dependence on geomagnetic activity, and a weak dependence on local time, season, latitude and L value. The authors empirically derived the follow expression for the ratio:

$$\log_{10} \alpha = -1.541 - 0.176r + 8.557 \times 10^{-3}P - 1.458 \times 10^{-5}P^2 \quad (5.1)$$

where r is geocentric radial distance in R_E and P is a proxy measure of solar activity defined by

$$P = \frac{F_{10.7} + F_{10.7A}}{2}$$

where $F_{10.7A}$ is the 81-day average of the daily 10.7-cm solar flux ($F_{10.7}$).

Figure 5.9 shows the density ratio computed using Equation 5.1 for the minimum ($P=135$) and maximum ($P=172$) solar activity of the five study intervals. Based on this dependence of α on R_E and since EUV measures only the He^+ content, using a constant density ratio will tend to overestimate the total number density at small radial distances and underestimate the total number density at larger radial distances.

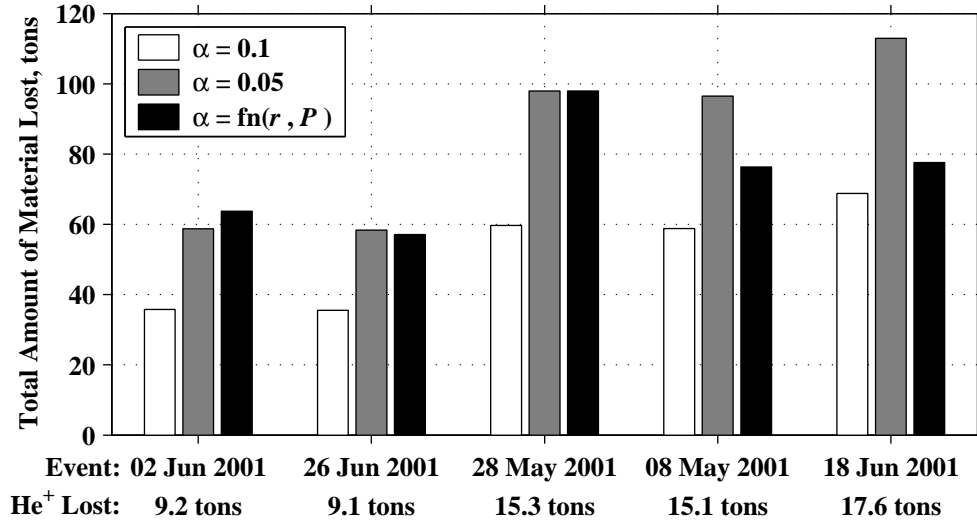


Figure 5.10. The total mass of plasma in metric tons removed for each of the disturbance intervals calculated using two constant density ratios, $\alpha = 0.1$, and $\alpha = 0.05$ and by allowing the ratio to vary as a function of radial distance and solar EUV input.

For each of the five study intervals, the total mass of plasma removed from the plasmasphere was estimated 3 different ways: 1) using a constant ratio $\alpha = 0.1$, 2) using $\alpha = 0.05$, and 3) using Equation 5.1. A constant He^+ to O^+ density ratio of 0.10 was used for all three estimates. The total mass was calculated as the sum of the total masses of H^+ , He^+ , O^+ ions with an equal number of electrons. As can be seen in Figure 5.10, the choice of α can cause the total estimated mass to vary significantly. When using a constant ratio, the total mass loss scales linearly with He^+ mass lost (shown below the event date). However, the initial plasma distribution as well as the He^+ mass lost contributes to the total mass lost when using Equation 5.1. For example, on both the May 28, 2001 and May 8, 2001 events, about 15 metric tons of He^+ was lost, and thus when using the constant ratio, the total mass lost is similar between the two events. However, when estimating the total mass lost using Equation 5.1, the May 28, 2001 loss estimate is ~ 22 tons higher than May 8, 2001. This result is due to the fact that the initial plasma distribution on May 28, 2001 (Figure 5.3) extended to higher radially distances where the He^+ distribution underestimates the total distribution.

The total number of electrons lost for the cases varied from ~ 1.5 to 4.8×10^{31} for all of the cases using the three values of α in agreement with the *Park* [1970] estimate of $\sim 3 \times 10^{31}$ electrons based on the removal of essentially all plasma in a belt extending globally from $L = 3.5$ to 5.

5.2 Conclusions

For a set of moderate disturbance periods, we calculated the total amount of He^+ removed from the plasmopause using calibrated global EUV images. For each of the events, between ~ 1 and 3×10^{30} He^+ ions were lost which constituted between 20 % and 42 % of the initial He^+ distribution. The lost percentage was correlated with the number of hours of strongly southward IMF ($B_z < -5$ nT). From these calculations the total amount of plasma removed from the plasmasphere was estimated by using several values of the He^+ to H^+ number density ratio. The total mass lost was found to be in the range of 50 to 100 metric tons for each of the cases with variations on the order of tens of metric tons depending on the He^+ to H^+ density ratio used.

As discussed in Section 2.3.6, the plasma removed from the plasmasphere during these disturbance periods is either transported to the dayside boundary layers or lost to the ionosphere. Although in the current analysis we cannot distinguish between these two mechanisms, we did attempt to estimate the loss inside versus outside the new plasmopause boundary and found that in the four cases with the largest loss percentage, the majority of that loss occurred in the region exterior to the new plasmopause boundary. This suggests that while losses to the ionosphere may be significant, a greater fraction of the material is lost due to convection.

The plasmaspheric material convected to the dayside boundary layers is then transported on open field lines over the polar cap and down the magnetotail [Su *et al.*, 2001]. Plasma sheet ion density and composition measurements [e.g., Lennartsson and Shelley, 1986] imply that although some small fraction of this eroded plasmaspheric material may join the plasma sheet, the vast majority of it is likely lost to the solar wind before the field line reconnects in the distant magnetotail.

Chapter 6

The Plasmaspheric Plume and the Precipitation of Energetic Protons

Studies of the plasmasphere are particularly important since the cold plasma density is a fundamental parameter in the generation and propagation of various types of plasma waves as well as the interaction of these waves with energetic particles. The interaction of plasma waves with geomagnetic trapped energetic particles results in significant losses of those particles through precipitation into the upper atmosphere. This chapter focuses on the observation of a subauroral arc produced by precipitating energetic protons and the association of this precipitation with the plasmaspheric plume.

6.1 Detached Subauroral Proton Arcs: Past Observations

The first global images of the Earth's proton aurora have been provided by the Far Ultraviolet (FUV) Spectrographic Imager (SI) [*Mende et al.*, 2000] onboard the IMAGE satellite [*Burch*, 2000]. On a number of occasions, arcs of precipitating protons have been observed at latitudes equatorward of and separated from the main proton

oval. First reported by *Immel et al.* [2002], these detached subauroral proton arcs appear over several hours of local time in the afternoon sector during geomagnetically disturbed periods and preferentially at times of high solar wind dynamic pressure. Further case studies by *Burch et al.* [2002] show that the subauroral arcs can appear after a change from negative to positive of either the B_z or B_y component of the interplanetary magnetic field (IMF). As a result of either IMF transition, the main proton oval contracts poleward, while the equatorward part of the oval remains at its original latitude. Thus, a separation of several degrees in latitude is created between the new oval position and the presumably pre-existing proton arc.

In situ satellite observations from both studies confirm the presence of precipitating protons and an absence of precipitating electrons in these subauroral arcs. While emissions in the main proton oval are due to particles with energies less than 10 keV, the subauroral arcs appear to be produced by precipitating ring current protons with energies in the range of ~ 10 to 30 keV.

In both studies, the authors noted the tendency for the subauroral arcs to be located in the mid-afternoon sector where, during disturbed periods, plumes of eroded plasmaspheric material can extend sunward from the main plasmasphere. Predicted by numerical modeling for many years [e.g., *Grebowsky*, 1970; *Chen and Grebowsky*, 1974], plasmaspheric plumes were first observed globally by the IMAGE Extreme Ultraviolet (EUV) imager (see Chapter 4).

Unfortunately, no EUV plasmaspheric data were available for the detached proton arc events previously reported. However in one of the previously reported cases, the Magnetospheric Plasma Analyzer (MPA) [*Bame et al.*, 1993] onboard the geosyn-chronously orbiting 1989–046 spacecraft observed enhanced fluxes of low energy plasmaspheric ions in the region where the equatorial extension of the subauroral arc was expected to map [*Burch et al.*, 2002]. Previously, good correspondence has been found between the evolving global structure of the plasmasphere observed by EUV and *in situ* plasma observations [*Moldwin et al.*, 2003; *Spasojević et al.*, 2003].

We present here the results of a case study of a geomagnetic disturbance on June 18, 2001 during which a direct association has been found between a detached subauroral proton arc observed by FUV and a plasmaspheric plume observed globally

by EUV.

6.2 Plasmaspheric Plume Formation

After several days of relatively quiet conditions, a minor geomagnetic storm occurred on June 18, 2001 which was characterized by an ~ 10 hour period of predominantly southward IMF and relatively high solar wind dynamic pressure (Figure 6.1). Signatures of multiple substorms were seen in the *AE* index, and the *SYM-H* (*Dst*) index reached a minimum -84 nT (-61 nT). The disturbance onset was initiated by a southward turning of the IMF at $\sim 03:00$ UT in conjunction with a steady rise in the solar wind dynamic pressure.

Figure 6.2 shows the plasmopause locations in the SM equatorial plane as extracted from the EUV global images at four times during the disturbance (labeled a – d in Figure 6.1). The evolution of the plasmasphere during this disturbed period is similar to the detailed case studies described in Chapter 4. Just prior to the disturbance onset (Figure 6.2a), the average equatorial plasmopause location was $L \simeq 5$, yet variations in the plasmopause radius on the order of $1 - 2 R_E$ were present in noon to dusk quadrant.

Figure 6.2b shows the plasmopause locations ~ 3 hours after disturbance onset. In response to the southward turning of the IMF at $\sim 03:00$ UT, inward motion of the plasmopause was observed across the entire nightside. For example at magnetic midnight, the plasmopause moved inward $\sim 1.6 R_E$ in ~ 3 hours (i.e., at a rate of $\sim 0.53 R_E$ per hour). In addition, a sunward surge of plasma was observed on the dayside. This motion is particularly evident by the sunward elongation of the azimuthal feature near dusk. The sunward motion effectively moved the plasmopause location inward $\sim 1.1 R_E$ at 18 MLT, and a narrow low density channel remained between the previously observed azimuthal features.

By the time of the next IMAGE observation period, the IMF B_z had been primarily negative for ~ 7 hours, and a distinct plasmaspheric plume had formed in the afternoon sector as a result of continued enhanced sunward convection and corotational flows across the dayside. The EUV image at 13:06 UT (Figure 6.2c) was taken

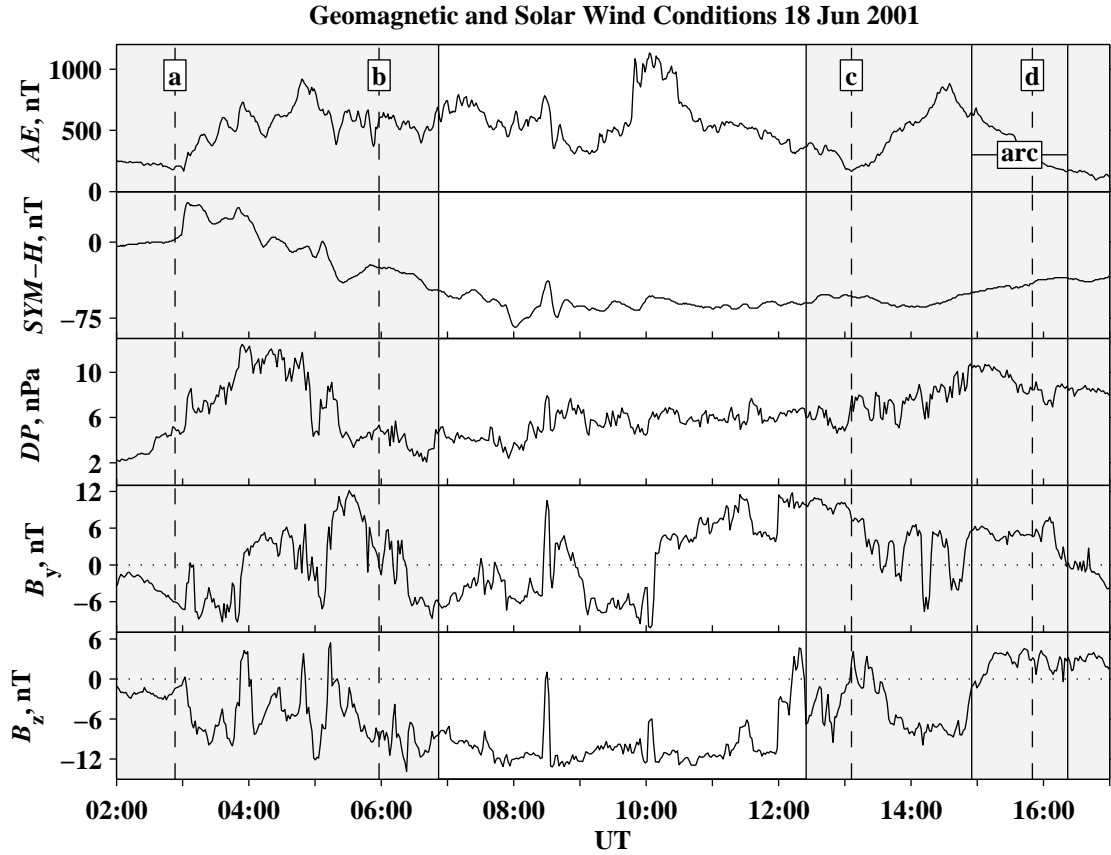


Figure 6.1. Geomagnetic and solar wind conditions from June 18, 2001. The panels from top to bottom are AE , $SYM-H$, solar wind dynamic pressure (from WIND SWE), IMF B_y and IMF B_z (from WIND MFI). The solar wind data have 22.5 minute transition time correction applied. The gray shaded regions are times for which IMAGE data are available, times of the EUV data shown in Figure 6.2 are labeled a – d, and the time between the solid vertical lines (labeled ‘arc’) is approximately when FUV observed the detached proton arc.

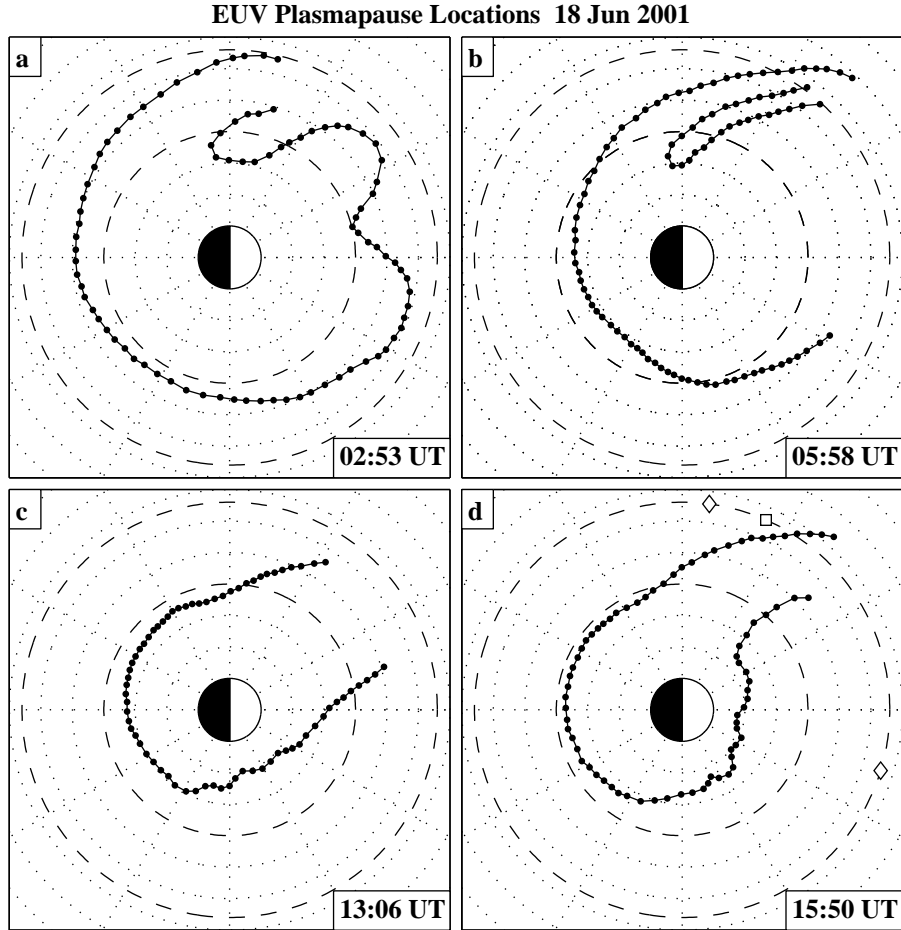


Figure 6.2. EUV plasmopause locations mapped to the SM equatorial plane on June 18, 2001. The dashed circles indicate $L = 4$ and 6.6 . The open square in (d) indicates the location of LANL-01a at 15:50 UT, and open diamonds bound the region over which enhanced cold plasma densities were observed *in situ* (Figure 6.3).

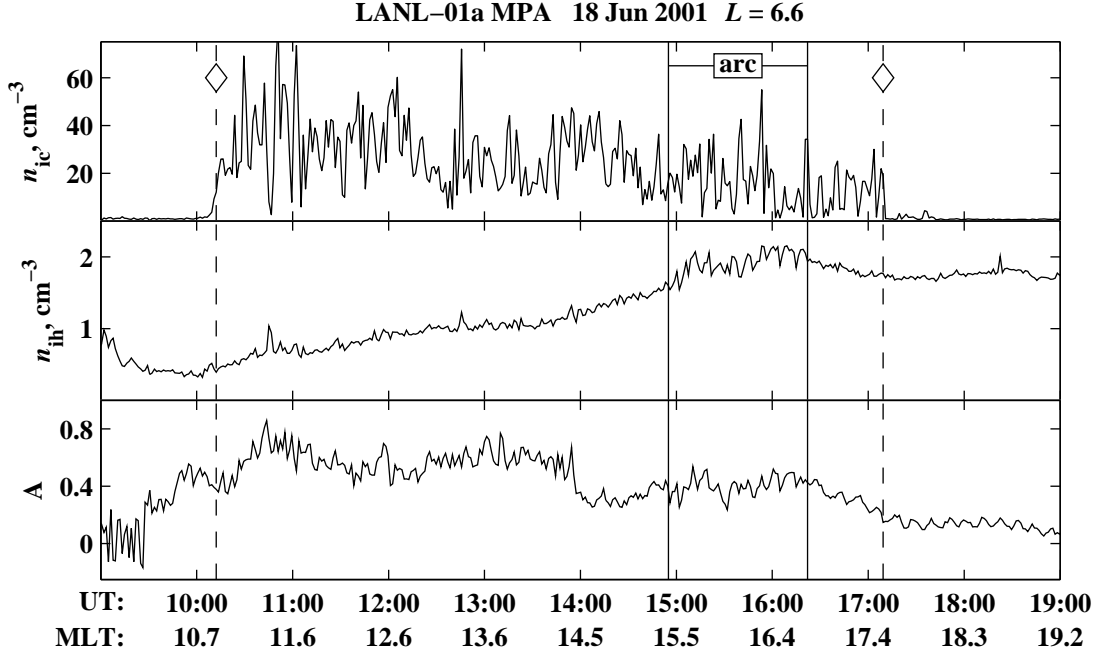


Figure 6.3. *In situ* measurements by the MPA instrument on LANL-01a on June 18, 2001. The top panel is the cold ion ($1 - 130$ eV/ q) density n_{ic} , the middle panel is the hot ion ($0.13 - 45$ keV/ q), density n_{ih} , and the bottom panel is the hot ion anisotropy ($A \equiv T_{\perp}/T_{\parallel} - 1$). The open diamonds correspond to the MLT locations indicated in Figure 6.2d, and the detached proton arc was visible in the FUV data over the interval labeled as ‘arc’.

when the satellite was still at a relatively low latitude ($\lambda \simeq 57^\circ$) so that the plume beyond $L \simeq 5.5$ was outside the field of view.

As is often observed during disturbed periods, the plasmapause location across the nightside varied smoothly whereas ripples or “crenulations” in the plasmapause surface were observed from ~ 04 MLT to noon.

Just before 15:00 UT, the IMF B_z turned and remained positive for several hours. As a result, the strength of magnetospheric convection decreased, and corotation flows began to dominate the inner magnetosphere. The eastern edge of the plume (Figure 6.2d) was observed to approximately corotate at $L = 4$, but the rate of rotation decreased with increasing radial distance to $\sim 87\%$ of corotation at $L = 5$ and only $\sim 40\%$ at $L = 6$.

During the period of plume formation, the LANL-01a satellite was traversing the dayside, and Figure 6.3 shows the observed density of cold ions (in the range of $\sim 1-130$ eV/ q) from the MPA instrument. Between $\sim 10:00$ and $17:00$ UT (local time sector between the two open diamonds in Figure 6.2d), MPA measured enhanced cold ion densities ($n_{ic} > 10$ cm $^{-3}$) associated with the initial sunward surge, subsequent plume formation and later plume rotation. In Figure 6.2d at 15:50 UT, LANL-01a is shown to be located (open square) east of the plume boundary as determined by EUV. However, cold ion densities of ~ 15 cm $^{-3}$ associated with the plume were measured by MPA but were likely below the sensitivity threshold of EUV estimated to be equivalent to 30 – 50 electrons cm $^{-3}$ [Goldstein *et al.*, 2003a; Moldwin *et al.*, 2003].

6.3 Detached Subauroral Proton Arc

The SI12 channel of the IMAGE FUV instrument produces global images of the proton aurora by detecting Doppler-shifted Lyman- α emission (121.8 nm) from charge-exchanging precipitating protons. An SI12 image from 15:50 UT on June 18, 2001 (the same time as Figure 6.2d) is shown in Figure 6.4. A detached subauroral proton arc can be seen in the afternoon sector extending to lower latitudes at later magnetic local times (from $\lambda \simeq 72^\circ$ at ~ 13 MLT to $\lambda \simeq 64^\circ$ at ~ 16.5 MLT).

A keogram centered on 16 MLT from the SI12 instrument in Figure 6.5 shows the temporal development of the detached arc. From $\sim 14:30$ to $15:00$ UT, bright proton aurora can be seen between $\sim 64^\circ - 70^\circ$ latitude. At $\sim 14:55$ UT, a northward and eastward turning of the IMF occurred, and in response the main proton oval contracted poleward and by 15:50 UT was centered at $\sim 72.5^\circ$. However, the equatorward portion of the oval remained at approximately the original latitude, and thus the main oval and the most equatorward arc became separated by several degrees. After $\sim 16:20$ UT, the emissions in the detached arc began to fade.

The amount of separation between the main oval and the detached arc increased with increasing magnetic local time. For example, at 15:50 UT at 16 MLT (Figure 6.5), there was $\sim 8^\circ$ of separation between the peak emission in each arc and a

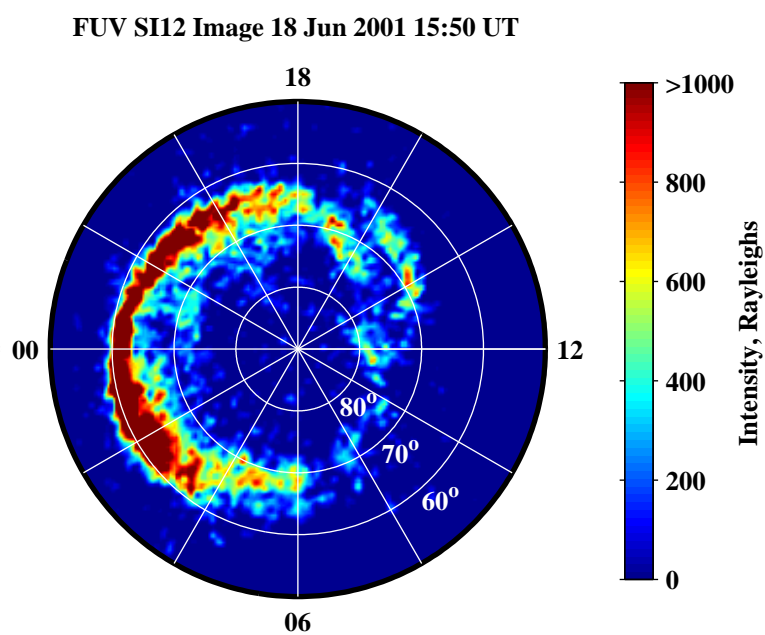


Figure 6.4. A proton aurora image from FUV SI12 on June 18, 2001 at 15:50 UT mapped onto magnetic latitude and MLT coordinates with the color corresponding to intensity in Rayleighs. Noon is to the right and 60°, 70° and 80° latitude circles are drawn.

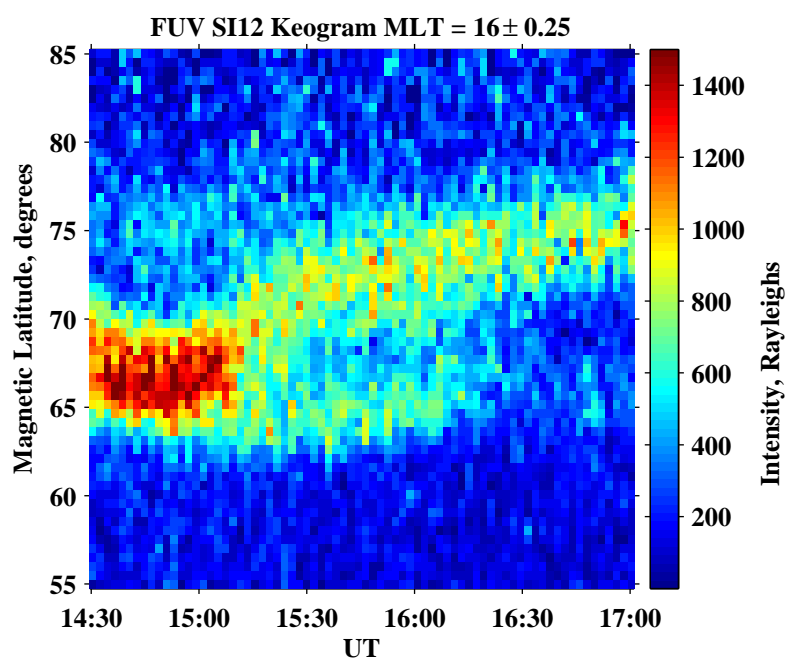


Figure 6.5. A keogram of the SI12 imager showing temporal evolution of proton aurora averaged over a half hour of local time centered on 16 MLT on June 18, 2001.

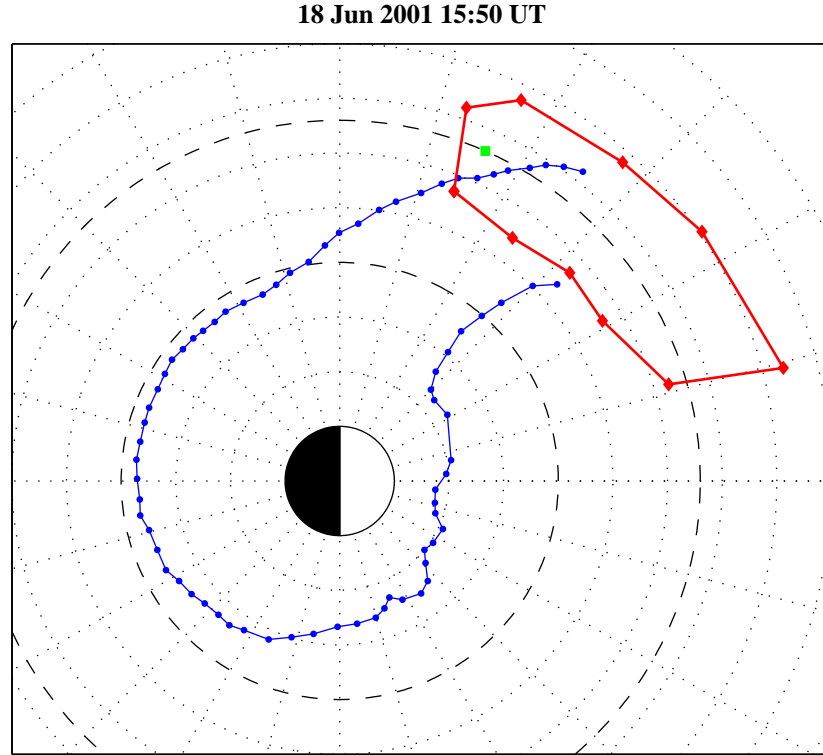


Figure 6.6. The EUV plasmopause locations (blue circles) and the edges of the detached proton arc (red diamonds) from 15:50 UT are mapped to the SM equatorial plane using the T96 magnetic field model. The green square indicates the location of LANL-01a and the dashed circles are $r=4$ and $6.6 R_E$.

relatively clear gap between the two. On the other hand, a similar keogram display for 12 MLT (not shown) showed only $\sim 4^\circ$ of separation between the peaks, and the two arcs blend together without a clear gap.

Figure 6.6 shows the EUV plasmopause locations and the equatorward and poleward edges of the detached proton arc at 15:50 UT mapped to the SM equatorial plane using the T96 magnetic field model [*Tsyganenko and Stern, 1996*] and the prevailing solar wind conditions. The plasmopause locations were mapped by finding the field line with the minimum apex along the line of sight to each point and tracing that field line to the SM equator. (Note there is little difference between the T96 mapping and the tilted dipole used in Figure 6.2.) The detached subauroral proton arc appears to map approximately to the location of the plasmaspheric plume as observed by EUV and MPA. At $\sim 16-17$ MLT, the poleward edge of the arc appears to map to higher radial distances than the eastern edge of the plume as observed by EUV, yet measurements by LANL-01a (open square) indicate plume material in this region, but at densities lower than the estimated EUV threshold. At earlier local times (13–15 MLT), the arc maps to a region that is outside of the field of view of the EUV instrument, but given the observation that the plume rotated slower at higher radial distances, it is likely that this region also contained enhanced cold plasma densities associated with the plume.

6.4 Wave-Particle Interactions

The apparent association between the plasmaspheric plume and the detached subauroral proton arc suggests that the precipitation mechanism may be a resonant interaction between ring current protons and electromagnetic ion cyclotron (EMIC) waves which are preferentially generated in the plume region.

The ring current (see [*Daglis et al., 1999*] and references therein) is formed primarily through the transport of particles from the plasma sheet into the inner magnetosphere during magnetic storms. It is unclear whether the ring current build-up mainly results from Earthward drift during periods of strong magnetospheric convection or as a result of induction electric fields associated with the dipolarization of

magnetic field lines during magnetospheric substorms [*Kamide et al.*, 1998].

Collisional processes such as charge exchange with the neutral geocorona and Coulomb collisions with thermal plasma are the dominant loss mechanism for ring current particles. However, these collisional processes are quite slow, and loss due to interaction with EMIC waves was first suggested by *Cornwall et al.* [1970] to account for rapid decay of the ring current in the early recovery phase of storms.

EMIC waves are transverse, left-hand circularly polarized waves that exist at frequencies below the local proton gyrofrequency. EMIC waves (in the range 0.1 – 5 Hz) occur most frequently in the outer dayside magnetosphere ($L > 7$) and are most likely to extend to lower L values ($L = 5$ to 7) in the afternoon local time sector [*Anderson et al.*, 1993].

As ring current ions are transported toward the Earth and thus into stronger magnetic fields, they gain energy in the transverse direction, producing anisotropic ($T_{\perp} > T_{\parallel}$) particle distributions. The anisotropy can be increased further by drift shell splitting [*Sibeck et al.*, 1987] and solar wind compression of the magnetosphere [*Anderson and Hamilton*, 1993]. The anisotropic proton distributions can become unstable to the amplification of EMIC waves, and specifically the presence of cold dense ions lowers the ion cyclotron instability threshold [*Gary et al.*, 1994]. Thus, anisotropic yet stable energetic proton distributions drifting westward from dusk may become unstable when they encounter the enhanced cold plasma densities within the plasmaspheric plume. As a result, EMIC waves would be amplified and can in turn pitch angle scatter the energetic protons into the loss cone.

During the ~ 1.5 hour period that FUV observed the detached proton arc, the MPA instrument on LANL-01a measured cold ion ($1 - 130$ eV/ q) densities in the range of $2 - 40$ cm $^{-3}$, hot ions ($0.13 - 45$ keV/ q) with an average density of ~ 2 cm $^{-3}$ and an energetic ion anisotropy ($A \equiv T_{\perp}/T_{\parallel} - 1$) of ~ 0.4 (Figure 6.3). Using a linear instability code (*Gary et al.* [1994]), the observed plasma parameters did indeed produce an EMIC instability. The cold ion density had a pronounced effect on the ion cyclotron instability with densities above ~ 8 cm $^{-3}$ yielding significantly larger wave growth rates and thus presumably increased scattering rates (S. P. Gary, private communication, 2003). After $\sim 16:30$ UT, MPA observed a decrease in both the hot

ion density and the hot ion anisotropy coincident with the decrease in the intensity of the emissions in the detached proton arc.

The geomagnetic disturbance of June 18, 2001, characterized by a prolonged period of southward IMF and high dynamic pressure, led to a buildup of the ring current as measured by the *Dst* index and as observed globally by the IMAGE High Energy Neutral Atom (HENA) imager (not presented here). Proton precipitation may have occurred throughout the disturbance in the region on the dayside filled with plasmaspheric material which over many hours formed the plasmaspheric plume. However only after the northward (and westward) turning of the IMF at 14:55 UT, which caused the main proton oval to contract and the plume to rotate toward dusk, was the subauroral proton arc visible and distinct.

6.5 Conclusions

Although relationships of the kind described here were suggested by previous studies [Immel *et al.*, 2002; Burch *et al.*, 2002], we presented here the first observation of a direct link between a detached subauroral proton arc and a globally observed plasmaspheric plume. The link between the proton arc and plume is consistent with the precipitation of protons being due to pitch angle scattering by EMIC waves, and reduction of the arc emission intensity after 16:20 UT may be correlated with a reduction in the temperature anisotropy and density of the westward drifting energetic ions as measured *in situ*.

Chapter 7

Summary

7.1 Summary of Major Results

The global vantage point provided by the IMAGE–EUV instrument has allowed us to explore several aspects of plasmaspheric dynamics from an entirely new perspective. Through detailed analysis of a set of moderately sized geomagnetic disturbances, we have obtained new results as well as confirmed and extended the results of previous experimental studies of the plasmasphere system. These disturbances represent periods of significant redistribution of mass in the magnetosphere as an estimated 50 to 100 metric tons of material are removed from a volume extending from 1.5 to 5.5 R_E in a period of 15 hours or less.

The strength and direction of the IMF B_z were shown to strongly influence the motion of the cold plasma. For each of the study periods during the disturbance onset, inward motion of the plasmapause was observed on the nightside in correlation with a southward turning of the IMF. In the June 26 – 27, 2001 event, we found highly significant correlations between the instantaneous velocity of the plasmapause at midnight MLT and the strength of B_z both during the initial disturbance onset and later during the main phase. This effect was also seen in other cases not presented here. In addition, the percentage of plasma removed from the plasmasphere for each of the cases correlated well with the total number of hours of strongly southward IMF over the duration of the disturbance.

While the disturbance onset leads to inward motion on the nightside, the plasmasphere on the dayside moves sunward. Over a period of many hours, this sunward surge evolves into a distinct plume in the afternoon sector. In the June 26 – 27, 2001 case, a rather sharp decrease was measured in the azimuthal flow speed as the western edge of the plume crossed ~ 14 MLT thus allowing the plume to stagnate for many hours.

The initial sunward surge and continued westward flows from dusk resulting from enhanced magnetospheric convection transport a considerable amount of plasmaspheric material to the outer dayside magnetosphere. For example during the June 18, 2001 event, $\sim 40\%$ of the initial He^+ distribution was removed from the plasmasphere, and we estimated that 76% (equivalent to $60 - 80$ tons of material) of that loss occurred outside the new plasmopause boundary. Thus enhanced cold plasma densities in a region of reduced magnetic field likely became conducive to the growth of electromagnetic ion cyclotron waves as anisotropic energetic proton drifted into the region from dusk. The waves in turn scattered those energetic protons into the loss cone, and the resulting precipitation was imaged by the FUV instrument.

The fate of the plume depends on geomagnetic conditions after the main disturbance, and we contrasted two somewhat extreme examples. On June 27, 2001, after the main disturbance, geomagnetic conditions became extremely quiet, and the plume was observed to rotate across the nightside at a rate less than (87% of) the expected corotation velocity. This result is in agreement with other observations of subrotating features especially under quiet conditions [e.g. *Sandel et al.*, 2003] and may be due to a violation of the the frozen-in flux condition.

On June 10, 2001, continued enhanced activity led to the wrapping of the plume, and we observed the transition from corotational type flows at low L to sunward directed flows at higher L which acted to form a low density channel between the plume and the main plasmasphere. A second plume formed on June 10, 2001 as a particularly large dayside shoulder feature rotated into the afternoon sector.

Various scale size azimuthal irregularities such as shoulders or crenulations are regularly observed during these disturbance periods, yet they appear to form only in a limited local time sector from approximately dawn to the western edge of the

plasmaspheric plume. Once formed, these mesoscale irregularities can be observed at any local time as they rotate in the aftermath of a disturbance. In contrast, the nightside plasmopause tends to vary smoothly from dusk to dawn throughout the disturbance. The mechanisms for the formation of these features are not yet completely known, nor is it known why this action is absent or suppressed in other local time sectors.

7.2 Suggestions for Future Research

The rich EUV data set and analysis techniques developed in this work provide many opportunities for future research.

First, the measurements of azimuthal and radial motions of the plasmopause boundary for the events presented in Chapters 4 and 6 can be directly compared to the results of various global convections models. A new empirical electric field model could be developed or constrained using EUV data. This would require developing an automated process for boundary selection as the current manual plasmopause selection process is prohibitively labor intensive.

Further study of morning sector azimuthal irregularities should also be undertaken. A particularly interesting example was found on May 28, 2001 when EUV observed the formation of a “notch” or inward indentation of the plasmopause. Figure 7.1a – c shows the plasmopause location at three times on May 28, 2001 during a moderate geomagnetic disturbance. At 18:45 UT (Figure 7.1a), a plasmaspheric plume can be seen in the afternoon sector, and the plasmopause boundary appears smooth at other local times. Over the course of several hours, a notch in the morning sector formed as indicated by the dashed radial line in Figure 7.1c. The notch appears to have formed as a result of inward motion of the boundary at a rate of $\sim 0.25 L$ per hour at a magnetic longitude of $\sim 226^\circ$ (Figure 7.1d). The mechanism for the formation of this feature is unknown, but this and others such events could be further explored with supporting data from mid-latitude ionospheric radar facilities such as Millstone Hill [e.g. *Foster and Rich*, 1998].

While analysis of global EUV images provides measurements of the boundary

motion, it does not yield information on the motion of plasma interior to boundary. The MPA instruments on the geosynchronous satellites provide not only cold plasma densities, used throughout this work, but also two component plasma flow measurements. The studies of plasmaspheric losses presented in Chapter 5 could be extended by careful study of the outward component of flow within the plasmaspheric plume.

Also, the type of analysis used in Chapter 5 to study the global loss of plasma during disturbances could easily be applied to study of plasmaspheric refilling in recovery periods.

The event detailed in Chapter 6 showing the association between the detached subauroral proton arc and the plasmaspheric plume was discovered quite serendipitously, and the relationship should be explored further through an exhaustive data search. Further studies could also take advantage of *in situ* measurements of precipitating energetic particles such as those from the FAST satellite [Pfaff *et al.*, 2001]. Also, the relationship between the cold plasma distribution and more transient types of subauroral proton events such as those reported by Hubert *et al.* [2003] could be investigated.

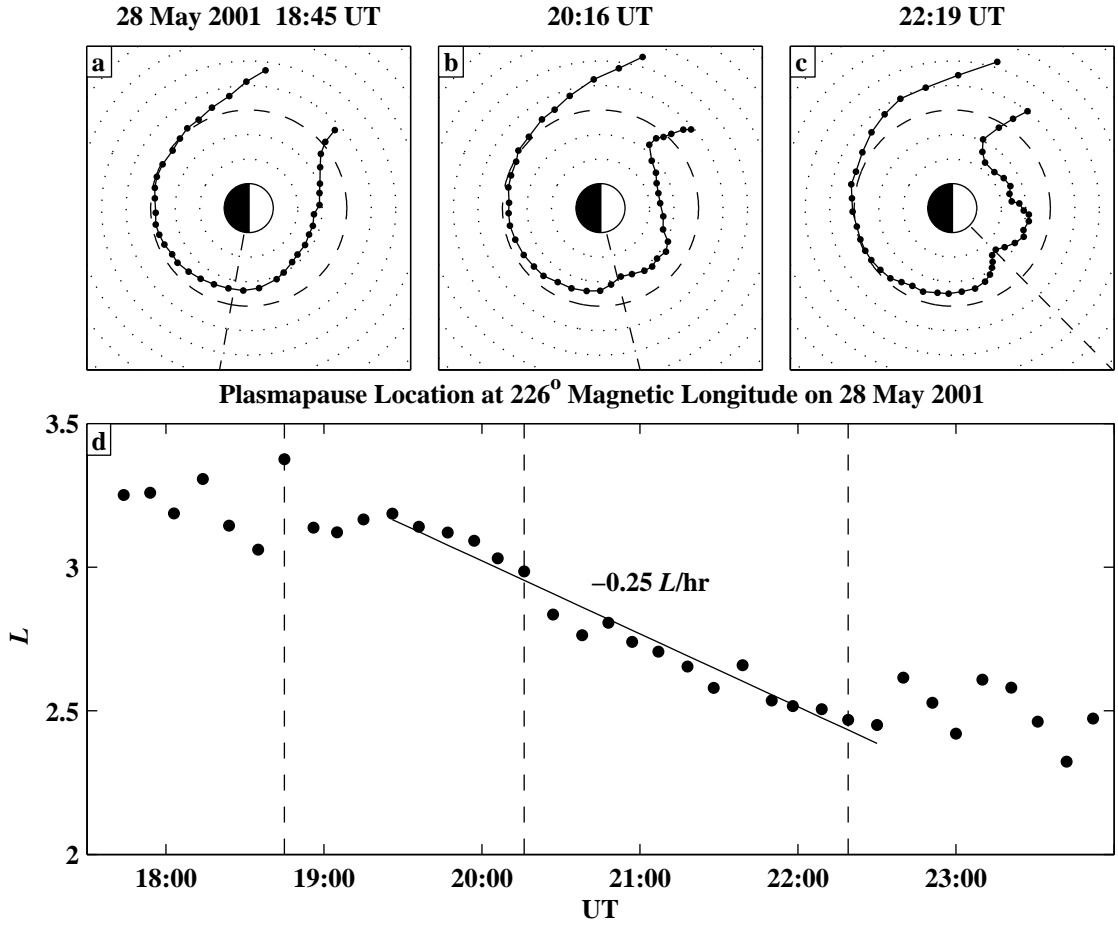


Figure 7.1. (a, b, c) EUV extracted plasmopause locations showing the formation of a notch in the morning local time sector on May 28, 2001. (d) The plasmopause location at 226° magnetic longitude is tracked showing that the notch formed as a result of inward motion of the boundary.

Bibliography

- Akasofu, S.-I., The development of the auroral substorm, *Planet. Space Sci.*, 12, 273, 1964.
- Anderson, B. J., R. E. Erlandson, and L. J. Zanetti, A statistical study of Pc 1 – 2 magnetic pulsations in the equatorial magnetosphere, 1. Equatorial occurrence distributions, *J. Geophys. Res.*, 97, 3075, 1992.
- Anderson, B. J. and D. C. Hamilton, Electromagnetic ion cyclotron waves stimulated by modest magnetospheric compressions, *J. Geophys. Res.*, 98, 11369, 1993.
- Anderson, P. C., D. L. Carpenter, K. Tsuruda, T. Mukai, and F. J. Rich, Multi-satellite observations of rapid subauroral ion drifts (SAID), *J. Geophys. Res.*, 106, 29585, 2001.
- Angerami, J. J., and J. O. Thomas, Studies of planetary atmospheres: 1. The distribution of electrons and ions in the Earth's exosphere, *J. Geophys. Res.*, 69, 4537, 1964.
- Angerami, J. J., and D. L. Carpenter, Whistler studies of the plasmopause in the magnetosphere: 2. Equatorial density and total tube electron content near the knee in magnetospheric ionization, *J. Geophys. Res.*, 71, 711, 1966.
- Axford, W. I. and C. O. Hines, A unifying theory of high-latitude geophysical phenomena and geomagnetic storms, *Can. J. Phys.*, 39, 1433, 1961.

- Bame, S. J., D. J. McComas, M. F. Thomsen, B. L. Barraclough, R. C. Elphic, J. P. Glore, J. T. Gosling, J. C. Chavez, E. P. Evans, and F. J. Wymer, Magnetospheric plasma analyzer for spacecraft with constrained resources, *Rev. Sci. Instrum.*, *64*, 1026, 1993.
- Bartels, J., N. H. Heck, and H. F. Johnston, The three-hour-range index measuring geomagnetic activity, *J. Geophys. Res.*, *44*, 411, 1939.
- Baumjohann, W. and R. A. Treumann, *Basic Space Plasma Physics*, Imperial College Press, London, 1997.
- Baumjohann, W., G. Paschmann, and C. A. Cattell, Average plasma properties in the central plasma sheet, *J. Geophys. Res.*, *94*, 6597, 1989.
- Borovsky, J. E., M. F. Thomsen, D. J. McComas, The superdense plasma sheet: plasmaspheric origin, solar wind origin, or ionospheric origin?, *J. Geophys. Res.*, *102*, 22089, 1997.
- Burch, J. L., Energy transfer in the quiet and disturbed magnetosphere, *Rev. Geophys. Space Phys.*, *21*, 463, 1983.
- Burch, J. L., IMAGE mission overview, *Space Sci. Rev.*, *91*, 1, 2000.
- Burch, J. L., S. B. Mende, D. G. Mitchell, T. E. Moore, C. J. Pollack, B. W. Reinisch, B. R. Sandel, S. A. Fuselier, D. L. Gallagher, J. L. Green, J. D. Perez, and P. H. Reiff, Views of Earth's magnetosphere with the IMAGE satellite, *Science*, *291*, 619, 2001.
- Burch, J. L., W. S. Lewis, T. J. Immel, P. C. Anderson, H. U. Frey, S. A. Fuselier, J.-C. Gérard, S. B. Mende, D. G. Mitchell, and M. F. Thomsen, Interplanetary magnetic field control of afternoon-sector detached proton auroral arcs, *J. Geophys. Res.*, *107*(A9), 1251, doi:10.1029/2001JA007554, 2002.
- Burton, R. K., R. L. McPherron, and C. T. Russell, The terrestrial magnetosphere: A half-wave rectifier of the interplanetary electric field, *Science*, *189*, 717, 1975.

- Brice, N. M., Bulk motion in the magnetosphere, *J. Geophys. Res.*, *72*, 5193, 1967.
- Carpenter, D. L., Whistler evidence of a “knee” in the magnetospheric ionization density profile, *J. Geophys. Res.*, *68*, 1675, 1963.
- Carpenter, D. L., Whistler studies of the plasmapause in the magnetosphere, 1. Temporal variations in the position of the knee and some evidence of plasma motion near the knee, *J. Geophys. Res.*, *71*, 693, 1966.
- Carpenter, D. L., Whistler evidence of the dynamic behaviour of the duskside bulge in the plasmasphere, *J. Geophys. Res.*, *75*, 3837, 1970.
- Carpenter, D. L. New whistler evidence of a dynamo origin of electric fields in the quiet plasmasphere, *J. Geophys. Res.*, *83*, 1558, 1978.
- Carpenter, D. L., and R. L. Smith, Whistler measurements of electron density in the magnetosphere, *Rev. Geophys.*, *2*, 415, 1964.
- Carpenter, D. L., K. Stone, K., J. C. Siren, T. L. Crystal, Magnetospheric electric fields deduced from drifting whistler paths, *J. Geophys. Res.*, *77*, 2819, 1972.
- Carpenter, D. L., and C. G. Park, On what ionospheric workers should know about the plasmapause-plasmasphere, *Rev. Geophys. Space Phys.*, *11*, 133, 1973.
- Carpenter, D. L., and N. T. Seely, Cross- L plasma drifts in the outer plasmasphere: Quiet time patterns and some substorm effects, *J. Geophys. Res.*, *81*, 2728, 1976.
- Carpenter, D. L., C. G. Park, and T. R. Miller, A model of substorm electric fields in the plasmasphere based on whistler data, *J. Geophys. Res.*, *84*, 6559, 1979.
- Carpenter, D. L., and R. R. Anderson, An ISEE/whistler model of equatorial electron density in the magnetosphere, *J. Geophys. Res.*, *97*, 1097, 1992.
- Carpenter, D. L., B. L. Giles, C. R. Chappell, P. M. E. Decreau, R. R. Anderson, A. M. Persoon, A. J. Smith, Y. Corcuff, and P. Canu, Plasmasphere dynamics

- in the duskside bulge region: a new look at an old topic, *J. Geophys. Res.*, *98*, 19243, 1993.
- Carpenter, D. L., and J. Lemaire, Erosion and recovery of the plasmasphere in the plasmopause region, *Space Sci. Rev.*, *80*, 153, 1997.
- Carpenter, D. L., R. R. Anderson, W. Calvert, and M. B. Moldwin, CRRES observations of density cavities inside the plasmasphere, *J. Geophys. Res.*, *105*, 23323, 2000.
- Carpenter, D. L. and A. J. Smith, The study of bulk plasma motions and associated electric fields in the plasmasphere by means of whistler-mode signals, *J. Atmos. Sol.-Ter. Phys.*, *63*, 1117, 2001.
- Carpenter D. L., M. Spasojević, T. F. Bell, U. S. Inan, B. W. Reinisch, I. A. Galkin, R. F. Benson, J. L. Green, S. F. Fung, and S. A. Boardsen, Small-scale field-aligned plasmaspheric density structures inferred from Radio Plasma Imager on IMAGE, *J. Geophys. Res.*, *107*(A9), 1258, doi10.1029/2001JA009199, 2002.
- Chamberlain, J. W., *Physics of the Aurora and Airglow*, Academic Press, New York, 1961.
- Chapman, S., and V. C. A. Ferraro, A new theory of magnetic storms, *Terr. Magn. Atmos. Electr.*, *36*, 171, 1931.
- Chapman, S., and J. Bartels, *Geomagnetism*, Oxford Univ. Press, London, 1940.
- Chappell, C. R., Detached plasma regions in the magnetosphere, *J. Geophys. Res.*, *79*, 1861, 1974.
- Chappell, C. R., K. K. Harris, and G. W. Sharp, A study of the influence of magnetic activity on the location of the plasmopause as measured by OGO 5, *J. Geophys. Res.*, *75*, 50, 1970a.
- Chappell, C. R., K. K. Harris, and G. W. Sharp, The morphology of the bulge region of the plasmasphere, *J. Geophys. Res.*, *75*, 3848, 1970b.

- Chappell, C. R., K. K. Harris, and G. W. Sharp, The dayside of the plasmasphere, *J. Geophys. Res.*, **76**, 7632, 1971.
- Chen, A. J., and R. A. Wolf, Effects on the plasmasphere of a time-varying convection electric field, *Planet. Space Sci.*, **20**, 483, 1972.
- Chen, A. J., and J. M. Grebowsky, Plasma tail interpretations of pronounced detached plasma regions measured by Ogo 5, *J. Geophys. Res.*, **79**, 3851, 1974.
- Comfort, R. H., Plasmasphere thermal structure as measured by ISEE-1 and DE-1, *Adv. Space Res.*, **6**, 31, 1986.
- Comfort, R. H., I. T. Newberry, and C. R. Chappell, Preliminary statistical survey of plasmaspheric ion properties from observations by DE-1/RIMS, in *Modeling Magnetospheric Plasma*, edited by T. E. Moore and J. H. Waite, Jr., pp. 288 – 114, American Geophysical Union, Washington D.C., 1988.
- Cornwall, J. M., F. V. Coroniti, and R. M. Thorne, Turbulent loss of ring current protons, *J. Geophys. Res.*, **75**, 4688, 1970.
- Cowley, S. W. H., A Beginner's Guide to the Earth's Magnetosphere, *Earth in Space*, **8**, 9, 1996.
- Craven, P. D., D. L. Gallagher, and R. H. Comfort, Relative concentration of He^+ in the inner magnetosphere as observed by the DE 1 retarding ion mass spectrometer, *J. Geophys. Res.*, **102**, 2279, 1997.
- Daglis, I. A., R. M. Thorne, W. Baumjohann, and S. Orsini, The terrestrial ring current: origin, formation and decay, *Rev. Geophys.*, **37**, 407, 1999.
- Davis, T. N., and M. Sugiura, Auroral electrojet activity index AE and its universal time variations, *J. Geophys. Res.*, **71**, 785, 1966.
- Dessler, A. J., and E. N. Parker, Hydromagnetic theory of geomagnetic storms, *J. Geophys. Res.*, **64**, 2239, 1959.

- Dungey, J. W., Interplanetary magnetic field and auroral zones, *Phys. Rev. Lett.*, *6*, 47, 1961.
- Freeman, J. W., H. K. Hills, T. W. Hill, P. H. Reiff, D. A. Hardy, Heavy ion circulation in the Earth's magnetosphere, *Geophys. Res. Lett.*, *4*, 195, 1977.
- Foster, J. C., and F. J. Rich, Prompt midlatitude electric field effects during severe geomagnetic storms. *J. Geophys. Res.*, *103*, 26367, 1998.
- Foster, J. C. and W. J. Burke, SAPS: A new categorization for sub-auroral electric fields, *EOS Trans. AGU*, *83*, 383, 2002.
- Foster, J. C., and H. B. Vo, Average characteristics and activity dependence of the subauroral polarization stream, *J. Geophys. Res.*, *107*(A12), 1475, doi:10.1029/2002JA009409, 2002.
- Fuselier, S. A., W. K. Peterson, D. M. Klumpar, E. G. Shelley, Entry and acceleration of He^+ in the low latitude boundary layer, *Geophys. Res. Lett.*, *16*, 751, 1989.
- Gallagher, D. L., P. D. Craven, and R. H. Comfort, Global core plasma model, *J. Geophys. Res.*, *105*, 18819, 2000.
- Gary, S. P., M. B. Moldwin, M. F. Thomsen, D. Winske, and D. J. McComas, Hot proton anisotropies and cool proton temperatures in the outer magnetosphere, *J. Geophys. Res.*, *99*, 23603, 1994.
- Goldstein, J., R. W. Spiro, P. H. Reiff, R. A. Wolf, B. R. Sandel, J. W. Freeman, and R. L. Lambour, IMF-driven overshielding electric field and the origin of the plasmaspheric shoulder of May 24, 2000, *Geophys. Res. Lett.*, *29*(16), doi:10.1029/2001GL014534, 2002.
- Goldstein J., M. Spasojević, P. H. Reiff, B. R. Sandel, W. T. Forrester, D. L. Gallagher, and B. W. Reinisch, Identifying the plasmopause in IMAGE EUV data using IMAGE RPI *in situ* steep density gradients *J. Geophys. Res.*, *108*(A4), 1147, doi:10.1029/2002JA009475, 2003a.

- Goldstein, J., B. R. Sandel, W. T. Forrester, and P. H. Reiff, IMF-driven plasmasphere erosion of 10 July 2000, *GRL*, *30*(3), 1146, doi:10.1029/2002GL016478, 2003b.
- Goldstein, J., R. W. Spiro, B. R. Sandel, R. A. Wolf, S.-Y. Su, and P. H. Reiff, Overshielding event of 28 – 29 July 2000, *Geophys. Res. Lett.*, *30*(8), 1421, doi:10.1029/2002GL016644, 2003c.
- Goldstein J., B. R. Sandel, and P. H. Reiff, Control of Plasmaspheric Dynamics by Both Convection and Sub-Auroral Polarization Stream, *Geophys. Res. Lett.*, *in press*, 2003d.
- Grebowsky, J. M., Model study of plasmopause motion, *J. Geophys. Res.*, *75*, 4329, 1970.
- Green, J. L., B. R. Sandel, S. F. Fung, D. L. Gallagher, and B. W. Reinisch, On the origin of kilometric continuum, *J. Geophys. Res.*, *107*(A7), 1105, doi:10.1029/2001JA000193, 2002.
- Gringauz, K. I., The structure of the ionized gas envelope of the Earth from direct measurements in the USSR of local charged particle concentrations, *Planet. Space Sci.*, *11*, 281, 1963.
- Helliwell, R. A., *Whistlers and Related Ionospheric Phenomena*, Stanford Univ. Press, Stanford, 1965.
- Hines, C. O., Atmosphere, stand thou still!, *Physics in Canada*, *17*, 14, 1961.
- Horne, R. B., The contribution of wave particle interactions to electron loss and acceleration in the earth's radiation belts during geomagnetic storms, in *The review of radio science*, edited by W. R. Stone, pp. 801 – 828, IEEE Press, Piscataway, 2002.
- Hubert, B., J.-C. Gérard, S. A. Fuselier, S. B. Mende, Observation of dayside sub-auroral proton flashes with the IMAGE-FUV imagers, *Geophys. Res. Lett.*, *30*, 1145, 10.1029/2002GL016464, 2003.

- Immel, T. J., S. B. Mende, H. U. Frey, L. M. Peticolas, C. W. Carlson, J.-C. Gérard, B. Hubert, S. A. Fuselier, and J. L. Burch, Precipitation of auroral protons in detached arc, *Geophys. Res. Lett.*, *29*(11), 10.1029/2001GL013847, 2002.
- Jaggi, R. K., and Wolf, R. A. Self-consistent calculation of the motion of a sheet of ions in the magnetosphere, *J. Geophys. Res.*, *78*, 2852, 1973.
- Kamide, Y., N. Yokoyama, W. Gonzalez, B. T. Tsurutani, I. A. Daglis, A. Brekke, and S. Masuda, Two-step development of geomagnetic storms, *J. Geophys. Res.*, *103*, 6917, 1998.
- Kivelson, M. G. and C. T. Russell, *Introduction to Space Physics*, Cambridge Univ. Press, Cambridge, 1995.
- Kozyra, J. U., V. K. Jordanova, R. B. Horne, R. M. Thorne, Modeling of the contribution of electromagnetic ion cyclotron (EMIC) waves to stormtime ring current erosion, in *Magnetic Storms*, edited by B. T. Tsurutani, W. D. Gonzalez, Y. Kamide, and J. K. Arballo, pp. 187 – 202, American Geophysical Union, Washington D.C., 1997.
- Kurita, K., M. Hayakawa, Evaluation of the effectiveness of theoretical model calculation in determining the plasmapause structure, *J. Geophys.*, *57*, 130, 1985.
- LeDocq, M. J., D. A. Gurnett, and R. R. Anderson, Electron number density fluctuations near the plasmapause observed by the CRRES spacecraft, *J. Geophys. Res.*, *99*, 23661, 1994.
- Lennartsson, W., and D. L. Reasoner, Low-energy plasma observations at synchronous orbit, *J. Geophys. Res.*, *83*, 2145, 1978.
- Lennartsson, W., and E. G. Shelley, Survey of 0.1- to 16-keV/e plasma sheet ion composition, *J. Geophys. Res.*, *91*, 3061, 1986.
- Lemaire, J., The mechanisms of formation of the plasmapause, *Ann. Geophys.*, *31*, 175, 1975.

- Lemaire, J., Plasma distribution models in a rotating magnetic dipole and refilling of plasmaspheric flux tubes, *Phys. Fluids B, Plasma Phys.*, 1, 1519, 1989.
- Lemaire, J. F., The formation of plasmaspheric tails, *Phys. Chem. Earth (C)*, 25, 9, 2000.
- Lemaire, J. F., The formation of the light-ion trough and peeling off the plasmasphere, *J. Atmos. Sol.-Ter. Phys.*, 63, 1285, 2001.
- Lemaire, J. F., and K. I. Gringauz, *The Earth's Plasmasphere*, Cambridge Univ. Press, Cambridge, 1998.
- Lui, A. T. Y, R. W. McEntire, and S. M. Krimigis, Evolution of the ring current during 2 geomagnetic storms, *J. Geophys. Res.*, 92, 7459, 1987.
- McComas, D. J., S. J. Bame, B. L. Barraclough, J. R. Donart, R. C. Elphic, J. T. Gosling, M. B. Moldwin, K. R. Moore, and M. F. Thomsen, Magnetospheric plasma analyzer: initial three-spacecraft observations from geosynchronous orbit, *J. Geophys. Res.*, 98, 13453, 1993.
- McComas D. J., S. J. Bame, P. Barker, W. C. Feldman, J. L. Phillips, P. Riley, J. W. Griffee, Solar Wind Electron Proton Alpha Monitor (SWEPAM) for the Advanced Composition Explorer, *Space Sci. Rev.*, 86, 563, 1998.
- McIlwain, C. E., A *Kp* dependent equatorial electric field model, *Adv. Space Res.*, 6, 187, 1986.
- Mende, S. B., H. Heetderks, H. U. Frey, J. M. Stock, M. Lampton, S. P. Geller, R. Abiad, O. H. W. Segmund, S. Habraken, E. Renotte, C. Jamar, P. Rochus, J.-C. Gérard, R. Sigler, and H. Lauche, Far Ultraviolet Imaging from the IMAGE Spacecraft, 3. Spectral Imaging of Lyman- α and OI 135.6 nm, *Space Sci. Rev.*, 91, 287, 2000.
- Moldwin, M. B., M. F. Thomsen, S. J. Bame, D. J. McComas, and K. R. Moore, An examination of the structure and dynamics of the outer plasmasphere using multiple geosynchronous satellites, *J. Geophys. Res.*, 99, 11475, 1994.

- Moldwin, M. B., M. F. Thomsen, S. J. Bame, D. J. McComas, and G. D. Reeves, The fine-scale structure of the outer plasmasphere, *J. Geophys. Res.*, *100*, 8021, 1995.
- Moldwin, M. B., L. Downward, H. K. Rassoul, R. Amin, and R. R. Anderson, A new model of the location of the plasmopause: CRRES results, *J. Geophys. Res.*, *107*(A11), 1339, doi:10.1029/2001JA009211, 2002.
- Moldwin, M. B., B. R. Sandel, M. F. Thomsen, and R. C. Elphic, Quantifying global plasmaspheric images with *in situ* observations, *Space Sci. Rev.*, *in press*, 2003.
- Mosier, S. R., M. L. Kaiser, and L. W. Brown, Observations of noise bands associated with the upper hybrid resonance by the Imp 6 radio astronomy experiment, *J. Geophys. Res.*, *78*, 1673, 1973.
- Murayama, T., Coupling function between solar wind parameters and geomagnetic indices, *Rev. Geophys. Space Phys.*, *20*, 623, 1982.
- Neugebauer, M. and C. W. Snyder, Mariner 2 observations of the solar wind, 1: Average properties, *J. Geophys. Res.*, *71*, 4469, 1966.
- Newberry, I. T., R. H. Comfort, P. G. Richards, and C. R. Chappell, Thermal He^+ in the plasmasphere: comparison of observation with numerical calculations, *J. Geophys. Res.*, *94*, 15265, 1989.
- Nishida, A., Formation of the plasmopause, or magnetospheric plasma knee, by the combined action of magnetospheric convection and plasma escape from the tail, *J. Geophys. Res.*, *71*, 5669, 1966.
- Park, C. G., A whistler study of the interchange of ionization between the ionosphere and the protonosphere, Tech. Rept. No. 3442-1, Radioscience Lab., Stanford Electronics Labs., Stanford Univ., Stanford, 1970.
- Park, C. G., Methods of determining electron concentrations in the magnetosphere from nose whistlers, Tech. Rept. No. 3454-1, Radioscience Lab., Stanford Electronics Labs., Stanford Univ., Stanford, 1972.

- Park, C.G. Some features of plasma distribution in the plasmasphere deduced from Antarctic whistlers, *J. Geophys. Res.*, *79*, 169, 1974.
- Park, C. G., and D. L Carpenter, Whistler evidence of large-scale electron-density irregularities in the plasmasphere. *J. Geophys. Res.*, *75*, 3825, 1970.
- Park, C. G., Westward electric fields as the cause of nighttime enhancements in electron concentrations in midlatitude F region. *J. Geophys. Res.*, *76*, 4560, 1971.
- Parks, G. K., *Physics of Space Plasmas*, Addison-Wesley, Redwood City, 1991.
- Pfaff, R., C. Carlson, J. Watzin, D. Everett, and T. Gruner, An overview of the Fast Auroral SnapshoT (FAST) satellite, *Space Sci. Rev.*, *98*, 1, 2001.
- Sandel, B. R., A. L. Broadfoot, C. C. Curtis, R. A. King, T. C. Stone, R. H. Hill, J. Chen, O. H. W. Siegmund, R. Raffanti, Allred, D., S. Turley, and D. L. Gallagher, The Extreme Ultraviolet Imager investigation for the IMAGE mission, *Space Sci. Rev.*, *91*, 197, 2000.
- Sandel, B. R., R. A. King, W. T. Forrester, D. L. Gallagher, A. L. Broadfoot, and C. C. Curtis, Initial Results from the IMAGE Extreme Ultraviolet Imager, *Geophys. Res. Lett.*, *28*, 1439, 2001.
- Sandel, B. R., J. Goldstein, D. L. Gallagher, and M. Spasojević, Extreme ultraviolet imager observations of the structure and dynamics of the plasmasphere, *Space Sci. Rev.*, *in press*, 2003.
- Sheeley, B. W., M. B. Moldwin, H. K. Rassoul, R. R. Anderson, An empirical plasmasphere and trough density model: CRRES observations, *J. Geophys. Res.*, *106*, 25631, 2001.
- Shepherd, S. G., and J. M. Ruohoniemi, Electrostatic potential patterns in the high latitude ionosphere constrained by SuperDARN measurements, *J. Geophys. Res.*, *105*, 23005, 2000.

- Sibeck, D.G., R. W. McEntire, A. T. Y. Lui, R. E. Lopez, and S. M. Krimigis, Magnetic field drift shell splitting: cause of unusual dayside particle pitch angle distributions during storms and substorms, *J. Geophys. Res.*, *92*, 13485, 1987.
- Smith, C. W., J. L'Heureux, N. F. Ness, M. H. Acuna, L. F. Burlaga, and J. Scheifele, The ACE Magnetic Fields Experiment, *Space Sci. Rev.*, *86*, 613, 1998.
- Smith, R. L, Propagation characteristics of whistlers trapped in field-aligned columns of enhanced ionization, *J. Geophys. Res.*, *66*, 3699, 1964.
- Smith, R. L, and D. L. Carpenter, Extension of nose whistler analysis, *J. Geophys. Res.*, *66*, 2582, 1961.
- Spasojević, M., J. Goldstein, D. L. Carpenter, U. S. Inan, B. R. Sandel, M. B. Moldwin, and B. W. Reinisch, Global response of the plasmasphere to a geomagnetic disturbance, *J. Geophys. Res.*, *108*(A9), 1340, doi:10.1029/2003JA009987, 2003.
- Stern, D.P. The motion of a proton in the equatorial magnetosphere, *J. Geophys. Res.*, *80*, 595, 1975.
- Su, Y.-J., J. E. Borovsky, M. F. Thomsen, N. Dubouoz, M. O. Chandler, T. E. Moore, and M. Bouhram, Plasmaspheric material on high-latitude open field lines, *J. Geophys. Res.*, *106*, 6085, 2001.
- Sugiura, M., Hourly values of equatorial Dst for IGY, in *Annals of the International Geophysical Year*, *35*, pp. 945 – 948, Pergamon Press, Oxford, 1964.
- Tobiska, W. K., T. Woods, F. Eparvier, R. Viereck, L. Floyd, D. Bouwer, G. Rottman, and O. R. White, The SOLAR2000 empirical solar irradiance model and forecast tool, *J. Atmos. Sol.-Ter. Phys.*, *62*, 1233, 2000.
- Tsyganenko, N. A., and D. P. Stern, Modeling the global magnetic field of the large-scale Birkeland current systems, *J. Geophys. Res.*, *101*, 27187, 1996.

- Vasyliūnas, V. M., Theoretical modes of magnetic field line merging, I. *Rev. Geophys. Space Phys.*, 13, 303, 1975.
- Vasyliūnas, V. M. Electric field and plasma flow: what drives what?, *Geophys. Res. Lett.*, 28, 2177, 2001.
- Volland, H., A semiempirical model of large-scale magnetospheric electric fields, *J. Geophys. Res.*, 78, 171, 1973.
- Walt, M., *Introduction to Geomagnetically Trapped Radiation*, Cambridge Univ. Press, Cambridge, 1994.
- Wolf, R. A., Magnetospheric Configuration, in *Introduction to Space Physics*, edited by M. G. Kivelson and C. T. Russell, pp. 288 – 329, Cambridge Univ. Press, Cambridge, 1995.